Year 2018

A Thesis for the Doctor's Degree of Sience

Direction-sensitive direct dark matter search with a three dimensional tracking gaseous detector

Kobe University
Department of Physics, Graduate School of Science

Ryota Yakabe

Advisor: Kentaro Miuchi

Abstract

Dark matter is one of the most important mysteries in particle physics and astrophysics. Cosmological observations show strong evidences that the dark matter constitutes about 27% of the universe. Although many experiments have been performed in search for the dark matter, the nature of the dark matter is still unknown. Weakly Interacting Massive Particles (WIMPs) are considered as one of the candidates of the dark matter and the direct detection experiments pursue for the WIMP-nucleus elastic scattering. NEWAGE is a direction-sensitive direct dark matter search experiment with a three-dimensional gaseous tracking detector (μ- TPC). A dark matter search experiment was performed from Jul. 2013 to Aug. 2017 (RUN14 to Run18) with the NEWAGE-0.3b' detector. The total live time is 435.85 days corresponding to an exposure of 4.505 kg·days which is about 14 times larger than that of our previous measurement. In this analysis, two new analysis methods were introduced to the NEWAGE analysis. First is the detector performance correction for a long term measurement. Second is the head-tail recognition of the nuclear tracks. Although the head-tail recognition power is limited, this method upgraded the NEWAGE-0.3b' detector from a "3D-axial" detector to a "3D-vector" detector. With this newly upgraded a 3D-vector detector, a first dark matter search was performed. The first experimental dark matter limits with a 3D-vector detector were set. The 90% spin-dependent WIMP-nucleon cross section limit of 2465 pb for 200 GeV/c^2 WIMP was obtained. The limit with 3D-axial method was also improved to 417 pb for 200 GeV/c^2 WIMPs.

Contents

Chapter 1

Introduction

1.1 Dark Matter

Dark matter is one of the most exciting mysteries of the universe in today's physics. Recent observations of Cosmic Microwave Background (CMB), Baryon Acoustic Oscillation (BAO), and Type Ia Supernovae, favor a flat universe consisting of 68.3% dark energy, 26.8% dark matter, and 4.9% baryon (ordinary matter). According to these "understandings", the dark matter is not an ordinary baryonic matter and it is very likely to be a particle in new physics beyond the Standard Model (SM) of the particle physics. In this section, studies on the dark matter in terms of astrophysics (Section1.2) and particle physics (Section1.3) are discussed.

1.2 Astrophysical Observation and dark matter

The dark matter was introduced by Zwicky in 1930s. He studied the motions of galaxies in Coma Cluster and Virgo Cluster and noticed that the velocities of galaxies were too fast to keep them in the cluster by the gravity of visible galaxies. Thus he introduced "dark matter" as an invisible source of the gravity to keep the galaxies within the cluster. The mass of the dark matter was estimated to be 10 to 100 times larger than the visible matter. Owing to the following astrophysical observations, we now have a lot of strong evidences of the dark matter as invisible mass in various scale of the universe. Also, non-baryonic nature is preferred from the measurements of chemical component of primordial nucleosynthesis.

1.2.1 Rotation curve of the galaxies

Galaxy rotation problem was first reported in 1970s. This problem is that the rotation velocity in the visible outer part is too fast to keep the stars within a galaxy. To solve this problem, additional invisible mass providing sufficient gravitational potential was introduced. The star's rotation velocity in a galaxy is calculated by Kepler's law as

$$\frac{v^2(r)}{r} = \frac{GM(r)}{r^2}, \tag{1.1}$$

where r is a radial distance from the center of a galaxy, $v(r)$ is a rotation velocity as the function of r, and $M(r)$ is a total mass within the radius r. The rotation velocity was measured from observations of the Doppler shift of bright lines in the spectra of stars, using 21 cm and 3.6 mm lines of the HI gas (neutral hydrogen gas) and the CO gas. If a galaxy consisted of only visible stars, the rotation velocity v must have fallen as $1/\sqrt{r}$ because observed stars concentrated at the center of the galaxy. However, the measured rotation velocity was almost constant even the outer region of the galaxy where the population of visible stars was very low. This observational result implies that the mass distribution $M(r)$ was proportional to r even at a large radius, and the galaxy must contain a large amount of invisible mass, or the dark matter. Figure1.1 is the rotation curve of NGC6503 galaxy measured by Doppler shift of 21 cm line[1]. This galaxy is a typical spiral galaxy with a 2 kpc radius core and a luminous disk expanding to more than 5 kpc from the center of the galaxy. Since the measured rotation curve was flat even up to the outer region, dark matter is required in the galaxy halo.
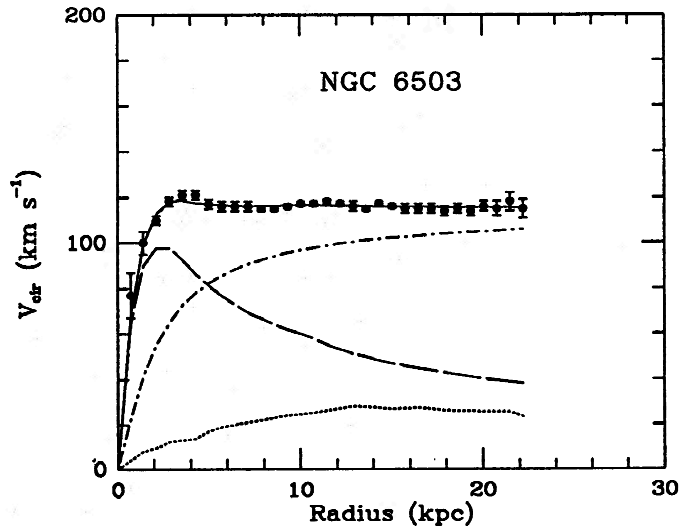
Figure 1.1: The rotation curve of NGC6503 spiral galaxy[1]. The black points are measured velocity by Doppler shift of 21 cm line. The dashed line and dotted line are the contribution to the rotation velocity from the observed disk and gas, respectively. The dashed-dotted line is the contribution from the invisible mass at the galaxy halo. The solid line is a sum of them.

1.2.2 X-ray observation of the cluster of galaxies

A cluster of galaxies is a large structure in the universe where $100 - 1000$ galaxies concentrate. The existence of the dark matter in the cluster of galaxies scale was noticed from the X-ray observation of the cluster of galaxies in 1980s. X-ray observation for the cluster of galaxies enabled us to see the distribution of high temperature gas. As a result, it was found out that cluster of galaxies was filled with high temperature plasma of about $10^7 \sim 10^8$ K and that almost all baryons exist as plasma instead of stars. Since such high temperature plasma becomes high pressure, the cluster of galaxies needs a gravitational

2

potential to keep the galaxies inside. Calculated mass was $10 - 100$ times as much as the sum of the galaxies and plasma in a cluster. Thus, the dark matter was suggested to sustain the distribution of cluster of galaxies scale. In the X-ray observation of clusters of galaxies Abell1060 and AWM7 by ASCA, the baryon fractions at clusters of galaxies was derived as shown in Figure 1.2[2]. Obtained baryon fractions were less than ~ 0.2, and then it revealed the existence of dark matter around a cluster of galaxies.
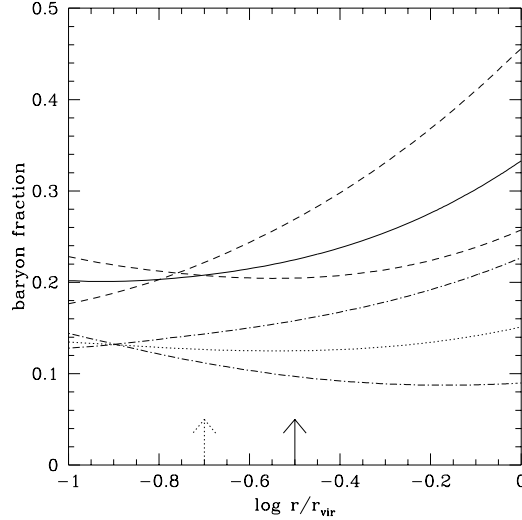
Figure 1.2: The baryon fraction of galaxy clusters Abell1060 and AWM7 observed by ASCA[2]. Horizontal axis is the distance from the center of galaxy clusters normalized by virial radius r_{vir}. 2 ± 0.5 Mpc and 2 ± 0.4 Mpc for Abel1060 and AWM7 were taken as r_{vir}, respectively. Solid line and dotted line show the best fit model corresponding to Abel1060 and AWM7, respectively. Dashed line and dot-dashed line show the model in case most compact and most expanded, respectively.

1.2.3 Weak gravitational lensing of Bullet Cluster

1E 0657-558, so-called "Bullet Cluster", is the region where two clusters of galaxies collided. Another dark matter evidence was observed in this region by weak gravitational lensing. Gravitational lensing is the phenomenon that the light from a distant source (a background galaxy) is bent by a distribution of the gravitational potential between the source and the observer. Here, the background object is observed to be multiplied or amplified or warped. When a gravitational potential is not so strong, a background galaxy is just warped, which is called "weak gravitational lensing". Using weak gravitational lensing, one can evaluate the shape and the amount of the gravitational potential with a statistical analysis of the warps of galaxies. The region around 1E 0657-558 was observed by Hubble Space Telescope to evaluate the mass distribution through weak gravitational lensing. The estimated mass distribution was the green contour in Figure1.3. In addition, the optical and X-ray radiation distribution observed by Magellan telescope and Chandra satellite are shown in the left and the right, respectively. The high temperature plasma observed by the X-ray and the right side cluster is moving away from the left side one at

3

~ 4700 km/s. As a line-of-sight velocity is only ~ 600 km/s, the collision occurred nearly in the plane of the sky. From these observations, gravitational potential does not trace the plasma distribution and obtained the picture that weakly interacting dark matter goes ahead in contrast to the viscous plasma. This result is another clear evidence of the existence of the dark matter at a cluster of galaxies scale.
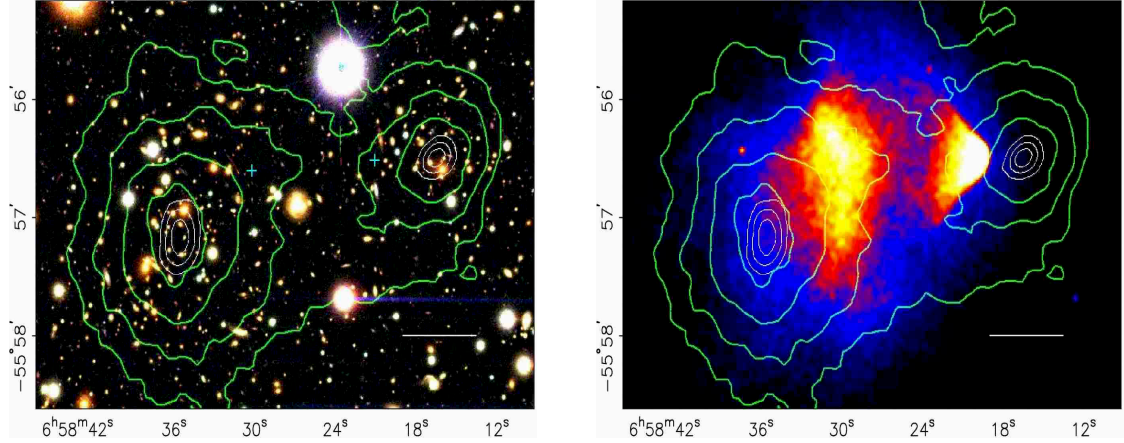
Figure 1.3: Space distribution of 1E 0657-558 where two clusters of galaxies collided. Left color image, right one and green contour represent the space distribution measured by optical, X-ray and gravitational lensing, respectively[3].
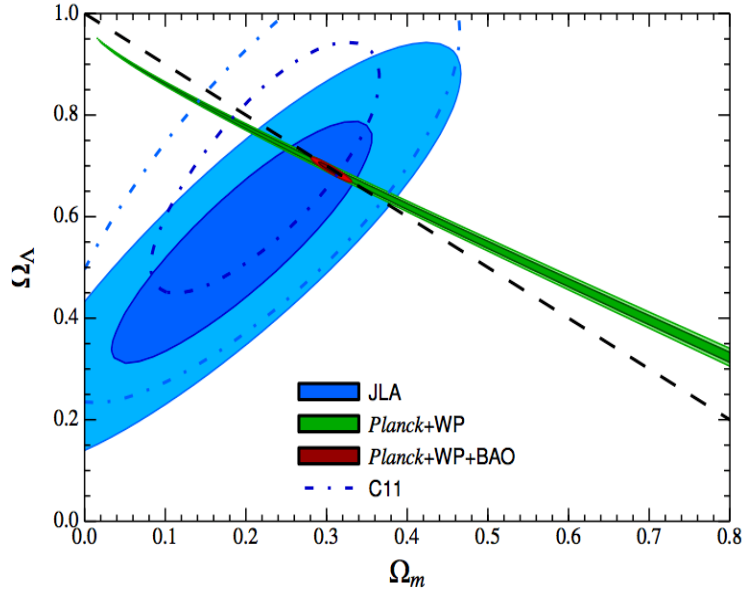
1.2.4 Cosmological parameters

Cosmology is the theory which covers the whole universe. The ΛCDM model, one of the Big Bang cosmological model including a cosmological constant denoted by Λ and cold dark matter (CDM), is now considered as a standard model of cosmology. In the ΛCDM model, the energy densities of the universe components are normalized by a critical density $\rho_c (= \frac{3c^2 H_0^2}{8\pi G})$ and called cosmological parameters. The normalized parameters corresponding to the densities of the dark energy, the matter and the radiation are referred to as Ω_Λ, Ω_m and Ω_r, respectively. Only Ω_r is accurately measured directly as following. The radiation density is dominated by the energy of the CMB, and several satellite observations determined its temperature to be T = 2.72548 $\pm$ 0.00057K, corresponding to $\Omega_r h^2 = 2.47 \times 10^{-5}$[8], where h is Hubble parameter normalized by 100 km/s/Mpc. Ω_r is negligible compared to Ω_m after the transition from the radiation dominant era to the matter dominant era at the early universe (z $\sim$104). When we consider baryon and dark matter separately, matter (Ω_m) is divided into baryon (Ω_b) and dark matter (Ω_{DM}). Here, we briefly explain the cosmological parameters. The evolution of the scale factor a, representing the size of universe, is written as

$$\left(\frac{\dot{a}}{a}\right)^2 = H_0^2 \left(\frac{\Omega_m}{a^3} + \frac{\Omega_r}{a^4} + \Omega_\Lambda + \frac{\Omega_k}{a^2}\right), \quad (1.2)$$

where H_0 is Hubble constant and Ω_k is the normalized curvature of the universe. Equation (1.2) is the normalized Friedmann equation and derived from general relativ-

4

ity assuming a homogeneous isotropic universe. By solving this differential equation, we can evaluate the time evolution of the universe and investigate the universe contraction/expansion, the flatness of the universe, and the existence of the Big Bang. The evolution depends on the cosmological parameters and thus these parameters can be determined by astrophysical observations. Obtained results on cosmological parameters are shown in Figure1.4. Combined analysis of several observations such as the observations of Type Ia SuperNova (IaSN)[4], Cosmic Microwave Background (CMB)[5], and Baryon Acoustic Oscillation (BAO)[6] representatively. Each observation sets the limit or allowed region of the cosmological parameters as shown in Figure 1.4.

Figure 1.4: Allowed regions of cosmological parameters $(\Omega_\Lambda, \Omega_m)$ by observations of IaSN, CMB("Plank" in the figure), and BAO. A flat universe with $(\Omega_\Lambda, \Omega_m) \approx (0.7, 0.3)$ is favored by the three observations.

A Type IaSN explosion occurs when a white dwarf in a binary system getting mass accretion from a companion star reaches to the Chandrasekhar mass. Thus, the maximum luminosity of IaSN is considered to be constant in spite of individual situations. In addition, a supernova is so luminous phenomenon that we can investigates a distant universe over z ∼ 1. The redshift of IaSN spectrum gives the expansion velocity of the universe at the distance of IaSN, and the measured intensity of a IaSN gives a luminosity distance d_{L} using $F = \frac{L}{4\pi d_{\mathrm{L}}^2}$, where F is observed flux at the Earth and L is an intrinsic luminosity of a IaSN. On the other hand, the luminosity distance can be written with cosmological parameters as

$$d_{\mathrm{L}}(z) = \frac{1+z}{H_0} \int_0^z [\Omega_{\Lambda,0} + (1+z')^3 \Omega_{m,0} + (1+z')^2 \Omega_{\mathrm{k},0}]^{-1/2} dz'. \tag{1.3}$$

From the equation (1.3), cosmological parameters can be evaluated. Figure shows observed IaSN luminosity (converted to magnitude m) as a function of the distance

5
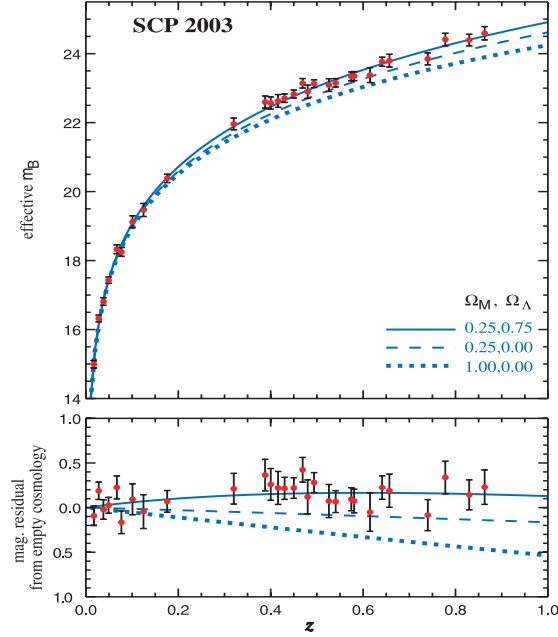
Figure 1.5: Observed IaSN luminosity (converted to magnitude m) as a function of the distance (shown in units of redshift z)[4]. Red points are measured and blue lines are models. Bottom figure shows the residual from the model assuming $\Omega_m = 0$, $\Omega_\Lambda = 0$. The model with $\Omega_m = 0.25$, $\Omega_\Lambda = 0.75$ was found to be consistent to the measurements.

(shown in units of redshift z)[4]. From this figure, the model with $\Omega_m = 0.25$, $\Omega_\Lambda = 0.75$ was found to be consistent to measurements.

Cosmic Microwave Background (CMB) is the thermal radiation left from the Big Bang. In the early and high temperature universe, where electrons, protons and photons exist with thermal equilibrium, photons cannot move straight due to Compton scatterings with electrons. As the temperature decreased adiabatically with the universe expansion, electrons and protons formed atoms, and photons can go straight. This phenomenon is called recombination and the temperature of this time corresponds to the ionizing energy of a hydrogen atom which is ~ 3000 K. After the recombination, photon's wavelength increased according to the universe expansion. And now, we observe this remained photon as a microwave and its spectrum is consistent to a black body of 2.725 K. Observed CMB is almost perfectly isotropic, with a very tiny 10^{-6} fluctuation in temperature. In order to study the fluctuations of various scales, the spatial distribution of the temperature $T(\theta, \phi)$ is obtained by fitting with spherical harmonics Y_{lm} using coefficients a_{lm} as

$$T(\theta, \phi) = \sum_{l=0}^{\infty} \sum_{m=-l}^{l} a_{lm} Y_{lm}((\theta, \phi), \tag{1.4}$$

$$C_l = \frac{1}{2l+1} \sum_{m=-l}^{l} |a_{lm}|^2.$$

Here C_l is called angular power spectrum and represents the amplitude of the fluctua-

tion at the scale of l ($\sim$180 in degree). C_0 is the monopole and corresponds to the average temperature, and C_1 is the dipole moment and corresponds to the motion of the earth. At the finer scale, fluctuations were induced by integrated Sachs-Wolfe effect (ISW) and have information of the recombination era (z $\sim$1100). ISW is the wavelength shifting effect that causes red shift at higher density region and blue shift at lower one due to a density fluctuation which was drawn out a quantum fluctuation by inflation. Assuming the cosmological parameters, we can evaluate the angular power spectrum by developing the temperature fluctuation induced by ISW according to the Boltzmann equation. Planck satellite observed the cosmic microwave fluctuations all over the sky[5]. Figure 1.6 shows the angular power spectrum measured by Planck.
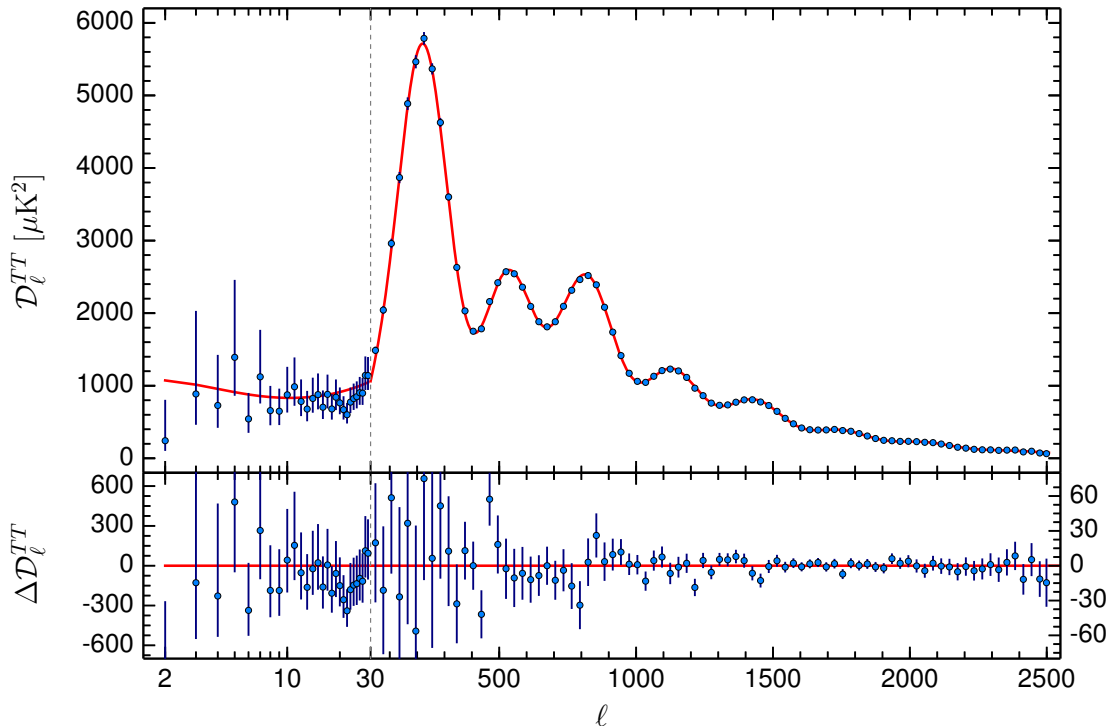
Figure 1.6: Angular power spectrum of CMB observed by Planck[5]. Blue points are measured data, red line is the best fit model. Bottom figure shows the residual from the best fit model.

Baryon acoustic oscillations (BAO) is the fluctuation in the density of the visible baryonic matter of the universe, caused by acoustic waves which existed in the early universe. Theoretical models of the structure formation of the cluster of galaxies enable us predict how to develop the density fluctuation from the acoustic waves to visible galaxies. Cosmological parameters are estimated by comparing observed galaxies distribution to the calculated one. The density fluctuation is considered to be developed by the gravitational instability because gravity is the unique long-range force in the four fundamental forces in the universe. In order to explain the density fluctuation, two types of dark matter were considered. One is the low mass dark matter with a relativistic. This type of dark matter is called hot dark matter (HDM). The other is the massive dark mat-

ter with non-relativistic velocities. This type of dark matter is called cold dark matter (CDM). In case of HDM, a fine structure is disturbed by the motion of the dark matter. In this case, a scenario that large scale structure is formed in the first place then clusters and galaxies are formed, is favored (top-down scenario). But this top-down scenario is not supported because galaxies exist even at the early universe around z ∼ 6. On the other hand, a bottom up scenario is favored in case of CDM and now this scenario is widely supported. Sloan Digital Sky Survey (SDSS) is the project surveying galaxies to investigate the distribution of galaxies[6]. In order to compare observations with the structure formation model, "two point correlation function" was used. Two point correlation function indicates the difference from the random distribution and defined as follows. Consider the probability $P(\boldsymbol{x}_1, \boldsymbol{x}_2)(dx_1)^3(dx_2)^3$ for galaxies contained to both of two volumes $(dx_1)^3(dx_2)^3$ around two points $\boldsymbol{x}_1$, $\boldsymbol{x}_2$ at a distance r. If the distribution of galaxies is perfectly at random, this probability is given as $\overline{n}^2(dx_1)^3(dx_2)^3$ using the number density of galaxies $\overline{n}$. But, the actual probability differs from random as

$$P(\boldsymbol{x}_1, \boldsymbol{x}_2)d^3x_1 d^3x_2 = \overline{n}^2[1 + \xi(r)](dx_1)^3(dx_2)^3, \qquad (1.5)$$

where $\xi(r)$ is the two point correlation function. Figure 1.7 is measured two point correlation function of galaxies by SDSS.
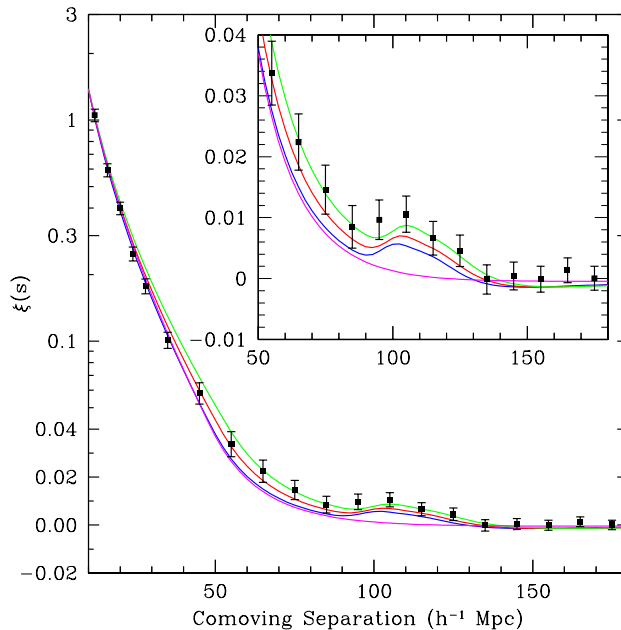
Figure 1.7: Measured two point correlation function of galaxies by SDSS[6]. Top, second and third lines show models assuming $\Omega_m h^2 = 0.12$, 0.13 and 0.14, respectively, all with $\Omega_b h^2 = 0.024$ and $n = 0.98$. The bottom line shows a pure CDM model assuming $\Omega_b h^2 = 0$ and $\Omega_m h^2 = 0.105$. Here, n is number density of galaxy. Inset is the enlarged view.

The peak around $\sim 100h^{-1}$Mpc is the indication of BAO and called an acoustic peak. The amplitude of an acoustic peak is sensitive to the gravitational components of the universe, and Ω_m is estimated by BAO as shown in Figure 1.4.

1.2.5 Big Bang nucleosynthesis

Big Bang Nucleosynthesis (BBN) describes the production of light nuclei besides hydrogen during the early universe. In 1940s, BBN was advocated by George Gamow to explain the ratio of elements in the universe, and after some discussions, the existence of CMB was predicted. Hence the discovery of CMB strongly supported BBN. Baryon density Ω_{b} is evaluated by BBN, and the dark matter density can be estimated as $\Omega_{\mathrm{DM}} = \Omega_{\mathrm{m}} - \Omega_{\mathrm{b}}$.

Production of heavier nuclei needs a high temperature and high density environment, such an ultimate environment is realized only at Big Bang, inner star, and Supernova. The fraction of elements in the universe is 75% hydrogen, 25% helium and the rest with other elements. Similar fractions are measured anywhere in the universe. The nuclei produced in inner stars or Supernovae are not only helium but also heavier elements. In order to explain the general abundance of light elements, BBN is inevitable.

At Big Bang, when the temperature and the density was high enough, protons and neutrons were at the equilibrium of weak interaction and they can convert to each other, where the ratio of protons to neutrons became 1 : 1. As the temperature and density became lower due to the universe expansion, the reaction velocity became slower than the expansion. When the temperature is below ~ 1 MeV, protons and neutrons are no longer in equilibrium. After that, neutrons one-sidedly decayed to protons, and the ratio of protons to neutrons became 4 : 1 at ~ 100 keV. At this temperature, the number of photons of which energy resolves deuterons ^{2}D (binding energy of ^{2}D = 2.22 MeV) by photodegradation reaction was less than the number of ^{2}D. As a result, suppressed nuclear fusion came to be superior, and then nucleons fused to more stable nuclei. Since the binding energy of ^{4}He (28.3 MeV) is much higher than that of ^{2}D, almost all the generated ^{2}D fused to ^{4}He, and almost all the neutrons were fixed in ^{4}He. Also, ^{7}Li and ^{7}Be were slightly generated. As the universe expanding, the universe became too cold and too low in density to keep nuclear fusions and then the fraction of elements was fixed at this time. The fixed fraction is calculated by solving the Boltzmann equation and depends on the baryon-to-photon ratio.

The number of photons and baryons decrease equally during the universe expansion, and the baryon-to-photon ratio has been kept constant. Since the number density of photons is measured by CMB observations, the number density of baryons can be calculated using the baryon-to-photon ratio. Figure 1.8 shows the relation of elements fraction to the baryon-to-photon ratio. The baryon-to-photon ratios measured from observed number density of some light elements are almost consistent among these elements, and baryon density $\Omega_{\mathrm{b}} h^2 = 0.0214$ is obtained[7]. Considering normalized Hubble parameter $h = 0.71^{+0.04}_{-0.03}$, the baryon density is calculated as $\Omega_{\mathrm{b}} = 0.044 \pm 0.004$. Because this value is too small to explain the matter density $\Omega_{\mathrm{m}} \sim 0.25$, the existence of non-baryon dark matter of the amount of $\Omega_{\mathrm{DM}} \sim 0.20$ is supported.
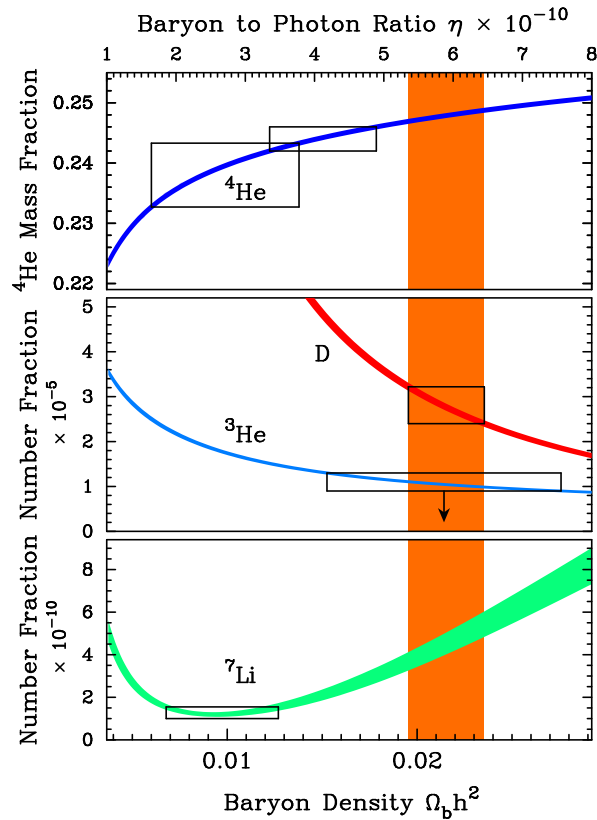
Figure 1.8: The relation of elements fraction to the baryon-to-photon ratio. Horizontal axis shows baryon-to-photon ratio and also written as baryon density. Vertical axis is elements fractions compared to hydrogen in the early universe. Four lines are the calculation of the standard BBN model (SBBN). The regions surrounded by squares are the allowed regions of number density from observation and corresponding baryon-to-photon ratio. Comparing the measurement to the calculation, $\Omega_b h^2 = 0.0214$ was obtained[7].

1.3 Dark matter candidates

From astrophysical observations, the amount of non-baryonic dark matter was estimated to be $\Omega_{\mathrm{DM}} \sim 0.20$. Also, the structure formation model (Section1.2.4) strongly favors the CDM than HDM. In this section, the candidates of the particle dark matter are reviewed.

1.3.1 WIMP

In particle physics, the Standard Model (SM) theory is well accomplished and can explain physical phenomena at low energy scale up to 1 TeV scale. However, SM theory has several problems, and this theory is considered to be the low energy approximation of an ultimate unified theory. In this ultimate unified theory, the fundamental four interactions are considered to be unified at Planck energy scale ($\sim 10^{19}$ GeV). The existence of theories beyond the SM (BSM) describing the phenomena between SM energy scale and Planck energy scale is widely believed. Weakly Interacting Massive Particles (WIMPs) are predicted in some BSMs, where the interaction is weak and the mass is heavier than SM particles. WIMPs are good candidates of the dark matter from their nature, and strongly motivated by particle physics. There are several theories which produce WIMPs such as supersymmetry theory (SUSY), universal extra dimensions (UED), little Higgs theory (LHT), and so on. Particularly, SUSY is strongly preferred as a BSM.

Supersymmetry theory (SUSY) is one of the these theories, which solves the hierarchy problem. In addition, a unification of the coupling constants is realized as shown in Figure1.9. This theory introduces new partner particles whose spins differ from those of SM particles by 1/2 as listed in Table1.1.

Table 1.1: SUSY particles

SM particles			SUSY particles		
Symbol	Name	Spin	Symbol	Name	Spin
$q = u, c, t$	up quark	1/2	$\tilde{q}_u^1, ..., \tilde{q}_u^6$	up squarks	0
$q = d, s, b$	down quarks	1/2	$\tilde{q}_d^1, ..., \tilde{q}_d^6$	down squarks	0
$l = e, \mu, \tau$	leptons	1/2	$\tilde{l}_1, ..., \tilde{l}_6$	sleptons	0
ν_e, ν_μ, ν_τ	neutrinos	1/2	$\tilde{\nu}_1, \tilde{\nu}_2, \tilde{\nu}_3$	sneutrinos	0
g	gluons	1	$\tilde{g}$	gluinos	1/2
$W^\pm$	W bosons	1	$\tilde{\chi}_1^\pm, \tilde{\chi}_2^\pm$	charginos	1/2
$H^\pm$	charged Higgs	0			
γ	photon	1	$\tilde{\chi}_1^0, ..., \tilde{\chi}_4^0$	neutralinos	1/2
Z^0	Z boson	1			
h^0	light scaler Higgs	0			
H^0	heavy scaler Higgs	0			
A^0	pseudo scaler Higgs	0			

The interaction of SUSY particles with SM particles are governed by the R-parity given as

$$R = (-1)^{3B+L+2S}, \tag{1.6}$$
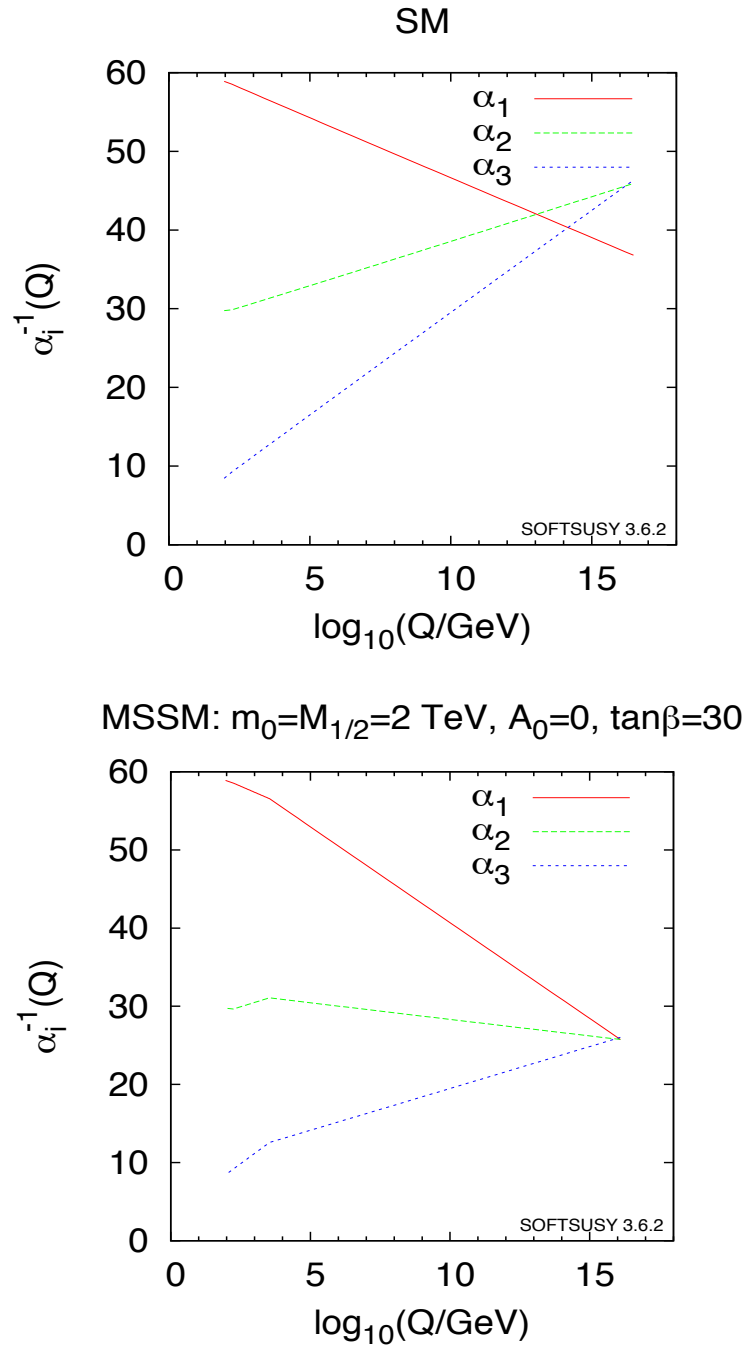
Figure 1.9: The relation of the coupling constants and energy in the standard model (SM) (top) and in the minimum supersymmetric standard model (MSSM) (bottom)[14]. α_1, α_2 and α_3 are the U(1), U(2) and U(3) couplings, respectively.

12

where B, L and S are the baryon number, the lepton number and the spin, respectively. SM particles have odd R-parities, while SUSY particles have even R-parities. From the conservation of the R-parity, the lightest SUSY particle (LSP) must be stable because it cannot decay to SM particles without SUSY particles. LSP is the lightest gluino or chargino or neutralino, whose spins are 1/2. If LSP is the lightest neutralino, the neutralino can be a candidate of the dark matter. Lightest neutralino ($\tilde{\chi}_1^0 \equiv \chi$) is the lightest linear combination of the photino ($\tilde{\gamma}$), the zino ($\tilde{Z}$) and the higgsinos ($\tilde{H}_1, \tilde{H}_2$). The photino and zino are expressed with the superpartners of gauge bosons, the bino ($\tilde{B}$) and the wino ($\tilde{W}_3$) as

$$\begin{aligned} \tilde{\gamma} &= \cos\theta_{\mathrm{W}}\tilde{B} + \sin\theta_{\mathrm{W}}\tilde{W}_3 \tilde{Z} \\ &= -\sin\theta_{\mathrm{W}}\tilde{B} + \cos\theta_{\mathrm{W}}\tilde{W}_3. \end{aligned} \tag{1.7}$$

Thus, lightest neutralino χ is written as

$$\chi = a_1\tilde{B} + a_2\tilde{W}_3 + a_3\tilde{H}_1 + a_4\tilde{H}_2. \tag{1.8}$$

The lightest SUSY particle (LSP) is stable and satisfies the nature of dark matter if LSP is uncharged[8]. The method of neutralino search and its review are described in Chapter?? and Chapter??.

Universal Extra Dimension (UED) is one of the theories to provide WIMP other than SUSY. UED is the BSM theory to unify the gravity interaction and the electromagnetic interaction. UED argues that the universe consists of five or more dimensions. In the low energy limit (energy scale of SM), the universe is observed as four dimensions. UED requires the Kaluza-Klein particles which conserve the K-K-parity. The lightest Kaluza-Klein particle (LKP) is thus stable and can be a candidate of the dark matter[9].

Little Higgs theory (LHT) is one of the BSM theories which naturally explains the electroweak symmetry breaking. LHT requires a global symmetry at $\sim 10\mathrm{TeV}$ scale and is broken at $\sim \mathrm{TeV}$ scale to cancel the second divergence of Higgs mass correction in the first loop. In this theory, new particles named T-partner and T-parity are introduced. SM particles have positive T-parity, and T-partners have negative T-parity in contrast. The lightest T- partner (LTP) is stable due to the conservation of the T-parity, and one of the candidates of the dark matter[10].

1.3.2 Axion

Axion was introduced as a new neutral light pseudo-scalar boson in order to solve the CP violation problem for the strong interaction[11]. The mass of the axion is limited to $1\,\mu\mathrm{eV} - 1\,\mathrm{meV}$ or $2\,\mathrm{eV} - 5\,\mathrm{eV}$ by the evolution of a star, observations of the neutrinos from supernova explosions, cosmology and so on. A lighter mass region remains as the window for the cold dark matter[12]. In spite of the light mass, axion is considered as a candidate of the dark matter because axions were produced at the phase transition of a vacuum around inflation era and axions were not in the thermal equilibrium with other particles at the early universe. Axions are widely searched for by the detection of photons generated by the Primakoff effect, which is the conversion from an axion to photons in a strong magnetic field[13]. Figure1.10 shows the results of axion searches in the lighter

mass region. No positive signal has been obtained and the limit of the axion-photon coupling for each mass of axion is set[14].
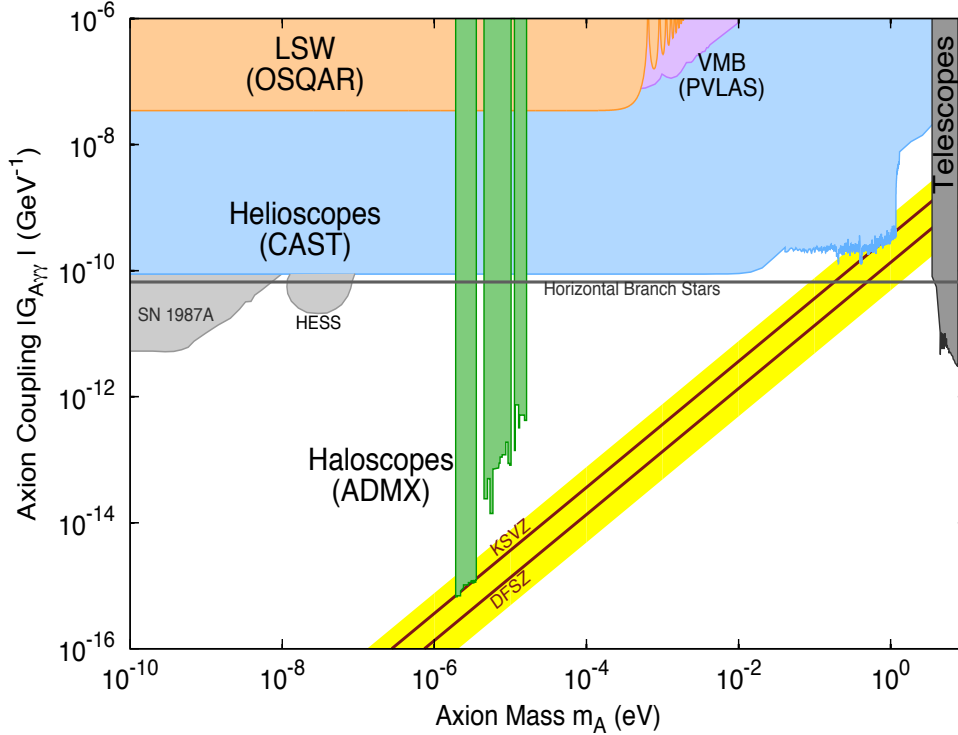
Figure 1.10: Current status of axion searches using the axion-photon coupling for each mass of axion[14].

1.3.3 Sterile neutrino

By the experimental studies on neutrino oscillation in these a few decades, it is established that there are three kind of neutrinos ν_e, ν_μ and ν_τ, and they are mixed with themselves. Now, the fourth neutrino named sterile neutrino is proposed as the final state of neutrino mixing to explain the result of LSND experiment[15]. In addition, by assuming sterile neutrino, the pulsar kick phenomenon of neutron stars also be explained[16]. Unlike other ordinal neutrinos, the sterile neutrino does not interact via the weak interaction. Mass of the sterile neutrino is estimated as $1 \sim 30$ keV. Then, sterile neutrino can be a candidate of the dark matter. Although the life time of the sterile neutrino is longer than the age of the universe, sterile neutrino is considered to decay to X-rays. The sterile neutrino search using X-ray space observatories are performed and the result are shown in Figure 1.2.4[15]. No X-ray signal originated from sterile neutrinos has been observed and the limit of the mixing angle for each mass is obtained.
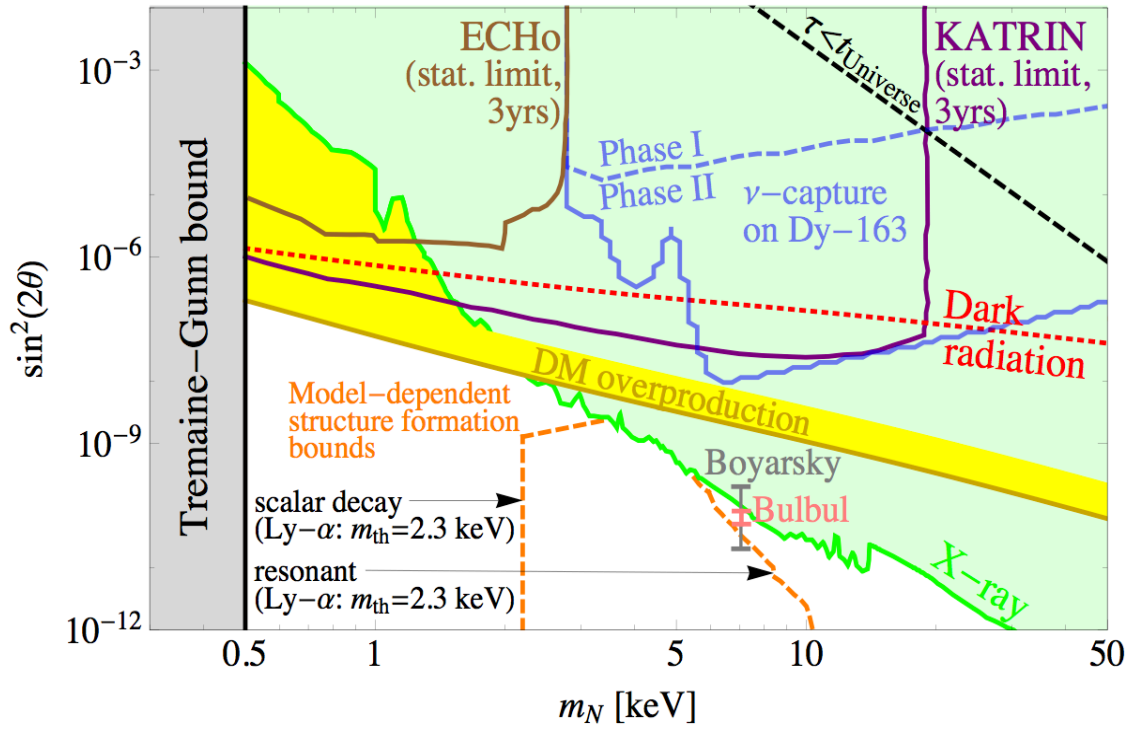
Figure 1.11: Obtained limits of the mixing angle θ as a function of sterile neutrino mass m_N[17]. The region above green line is the constraint region by X-ray observations. The region above yellow-gold line is the constraint region since DM overproduced.

1.3.4 Other candidate

In addition to the candidates described above, there are a variety of dark matter candidates such as mirror matter[22], asymmetric dark matter[23], crypton[24], and so on. Please see the references for details.

Chapter 2

Method of Direct Dark Matter Search

Direct search of the WIMP dark matter detection pursues for the detection via WIMP-nucleus elastic scatterings. Direct detection can provide the direct evidence of the existence of the dark matter in the halo of our galaxy. In this section, the theoretical framework of the direct detection focusing on the expected signal is reviewed[25].

2.1 Energy Spectrum

Direct detection method is to detect the energy deposition on the nucleus via WIMP-nucleus elastic scatterings, and thus the calculation of the expected energy spectrum is the first step to estimate the signals. An elastic scattering process is usually assumed and the shape of the expected energy spectrum depends on the relative mass of the target nucleus to the WIMP mass and the relative velocity of the Earth to the halo of our galaxy. The rate of the cross section are determined by the cross section of the WIMP-nucleus scattering and the flux of the WIMPs.

The solar system rotates in our galaxy at a distance of 8 kpc from the center of the galaxy, and the Earth rotates around the Sun. Then, the velocity of the Earth relative to the galactic halo is written as

$$
\begin{aligned}
v_{\mathrm{E}}(= |\boldsymbol{v}_{\mathrm{E}}|) =\ & v_{\mathrm{sum}} + v_{\mathrm{orb}}\ \cos\theta_{\mathrm{orb}}\ \sin(2\pi y) \\
\simeq\ & 244 + 15\sin(2\pi y)\ [\mathrm{km/sec}],
\end{aligned}
\tag{2.1}
$$

where v_{sun} is the velocity of the Sun relative to the galactic halo, v_{orb} is the orbital rotation velocity of the Earth around the Sun, θ_{orb} is the inclination of the Earth orbital plane with respect to the galactic plane and y is the time in year from March 2nd. Figure 2.1 shows the schematic view of the motion of the Sun and the Earth in our galaxy. Due to the rotation of the Earth around the Sun, the relative velocity of the Earth to our galaxy has its maximum in June and its minimum in December.
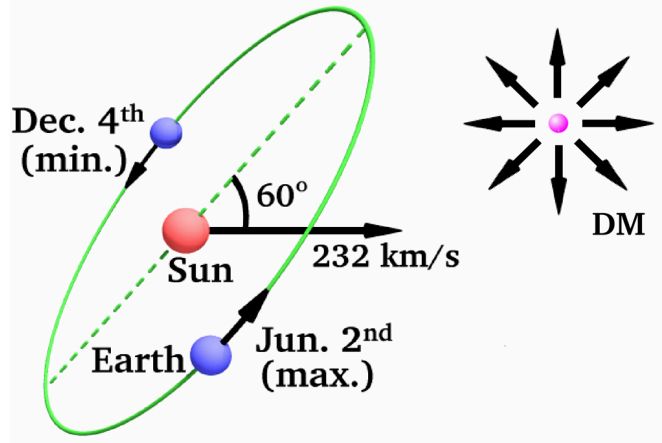
Figure 2.1: The schematic view of the motion of the Sun and the Earth in our galaxy.

The number density of WIMPs, dn, with the velocity of $v \sim v + dv$ is written as

$$dn = \frac{n_0}{k} f(\boldsymbol{v}, \boldsymbol{v}_\mathrm{E}) d^3 v, \tag{2.2}$$

$$n_0 \equiv \int_0^{v_{\mathrm{esc}}} dn, \quad k = \int_0^{2\pi} d\phi \int_{-1}^{+1} d(\cos\theta) \int_0^{v_{\mathrm{esc}}} f(\boldsymbol{v}, \boldsymbol{v}_\mathrm{E}) v^2 dv,$$

where n_0 is the total number of WIMPs in our galaxy, k is the normalize constant, $v_e sc$ is the escape velocity of the galaxy, θ is the angle between $\boldsymbol{v}_\mathrm{E}$ and WIMP velocity, and ϕ is azimuth angle taking WIMP velocity vector as a zenith. Assuming a Boltzmann distribution, the velocity distribution of the dark matter $f(\boldsymbol{v}, \boldsymbol{v}_\mathrm{E})$ is written as

$$f(\boldsymbol{v}, \boldsymbol{v}_\mathrm{E}) = e^{-(\boldsymbol{v}+\boldsymbol{v}_\mathrm{E})^2/v_0^2} \tag{2.3}$$

where v_0 is the velocity dispersion of our galaxy and if the galaxy the one of the rotation velocity is flat, it becomes rotation velocity. The normalize constant k is derived as

$$k = k_0 = (\pi v_0^2)^{3/2} \qquad (v_{\mathrm{esc}} = \infty) \tag{2.4}$$

$$k = k_1 = k_0 \left\{ \mathrm{erf}\left(\frac{v_{\mathrm{esc}}}{v_0}\right) - \frac{2}{\sqrt{\pi}} \frac{v_{\mathrm{esc}}}{v_0} e^{-v_{\mathrm{esc}}^2/v_0^2} \right\} \qquad (v_{\mathrm{esc}} \neq \infty), \tag{2.5}$$

where $\mathrm{erf}(x) \equiv \frac{2}{\sqrt{\pi}} \int_0^x e^{-t^2} dt$ is the error function. The differential event rate R per target mass per days is

$$R = \frac{N_A}{A} \sigma v dn, \tag{2.6}$$

where N_A is the Avogadro number (6.02×10^{26}), A is the mass number of the target nucleus, $v = |\boldsymbol{v} - \boldsymbol{v}_\mathrm{E}|$ is the dark matter velocity relative to the target, σ is the WIMP-nucleus cross section.

Strictly, σ depends on the momentum transfer. In this section, we discuss the cross section with zero momentum transfer σ_0. The cross section taking account of the momentum transfer will be discussed in the latter section2.3. The total event rate R is derived by integrating Equation (2.6) as

$$dR = \frac{N_A}{A}\sigma_0 \int v\, dn, \tag{2.7}$$

The total event rate R_0 for $v_E = 0$ and $v_{esc} = \infty$ is described as

$$R_0 = \frac{2}{\sqrt{\pi}}\frac{N_A}{A}\frac{\rho_D}{M_D}\sigma_0 v_0 \tag{2.8}$$

$$= \frac{361}{M_D M_N}\left(\frac{\sigma_0}{1\mathrm{pb}}\right)\left(\frac{\rho_D}{0.3\mathrm{GeV}/c^2/\mathrm{cm}^3}\right)\left(\frac{v_0}{220\mathrm{km/s}}\right), \tag{2.9}$$

where ρ_D is the mass density of the dark matter, M_D is the mass of the dark matter, $M_N(= 0.932A)$ is the mass of the target nucleus. The Equation (2.9) is normalized by σ_0 = 1pb, v_0 = 220 km/s, ρ_D = 0.3 GeV/c^2/cm³.

The recoil energy E_R of the nucleus with a mass M_N caused by an elastic scattering of the dark matter with the kinematic energy $E(= \frac{1}{2}M_D v^2)$ in the laboratory system is

$$E_R = Er(1 - \cos\theta)/2 \tag{2.10}$$

$$r = \frac{4M_D M_N}{(M_D M_N)^2}, \tag{2.11}$$

where θ is the scattering angle in the center of mass system, r is the reduced mass. Assuming the scattering is isotropic in the center of mass system, $\cos\theta$ distribution become flat and E_R also becomes flat in the $0 \leq E_R \leq Er$ region. Then the energy spectrum $\frac{dR}{dE_R}$ is written as

$$\frac{dR}{dE_R} = \int_{E_{\min}}^{E_{\max}}\frac{1}{Er}dR(E) \tag{2.12}$$

$$= \frac{1}{E_0 r}\int_{v_{\min}}^{v_{\max}}\frac{v_0^2}{v^2}dR(v), \tag{2.13}$$

where $E_{\min} = E_R/r$ is the minimum kinetic energy of WIMP capable to give the energy E_R to a target nuclei, $E_{\max}$ is the maximum kinetic energy of WIMP in a laboratory system, E_0 is defined as $E_0 = \frac{1}{2}M_D v_0^2 = \frac{v_0^2}{v^2}E$. The energy spectrum is obtained using Equation (2.2), (2.3), and (2.6) as

$$\frac{dR}{dE_R} = \frac{R_0}{E_0 r}\frac{k_0}{k}\int_{v_{\min}}^{v_{\max}}\frac{1}{v}f(\boldsymbol{v}, \boldsymbol{v}_E)d^3 v. \tag{2.14}$$

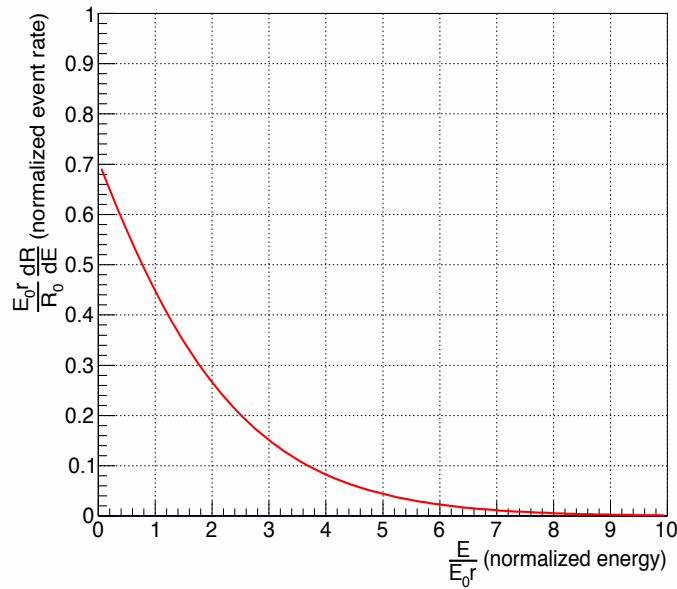By performing the integration of Equation (2.14), the specific formula of energy spectra are obtained as

$$\frac{dR(0,\infty)}{dE_R} = \frac{R_0}{E_0 r} e^{-E_R/E_0 r}, \tag{2.15}$$

$$\frac{dR(0,v_{\rm esc})}{dE_R} = \frac{k_0}{k_1} \left\{ \frac{dR(0,\infty)}{dE_R} e^{-E_R/E_0 r} - \frac{R_0}{E_0 r} e^{-v_{\rm esc}^2/v_0^2} \right\} \tag{2.16}$$

$$\frac{dR(v_{\rm E},\infty)}{dE_R} = \frac{R_0}{E_0 r} \frac{\sqrt{\pi}}{4} \frac{v_0}{v_{\rm E}} \left\{ {\rm erf}\left(\frac{v_{\rm min}+v_{\rm E}}{v_0} \right) - {\rm erf}\left(\frac{v_{\rm min}-v_{\rm E}}{v_0} \right) \right\} \tag{2.17}$$

$$\frac{dR(v_{\rm E},v_{\rm esc})}{dE_R} = \frac{k_0}{k_1} \left\{ \frac{dR(v_{\rm E},\infty)}{dE_R} - \frac{R_0}{E_0 r} e^{-v_{\rm esc}^2/v_0^2} \right\}. \tag{2.18}$$

Figure 2.2 shows the normalized energy spectrum.

Figure 2.2: The normalized energy spectrum of nucleus caused by an elastic scattering of the WIMP.
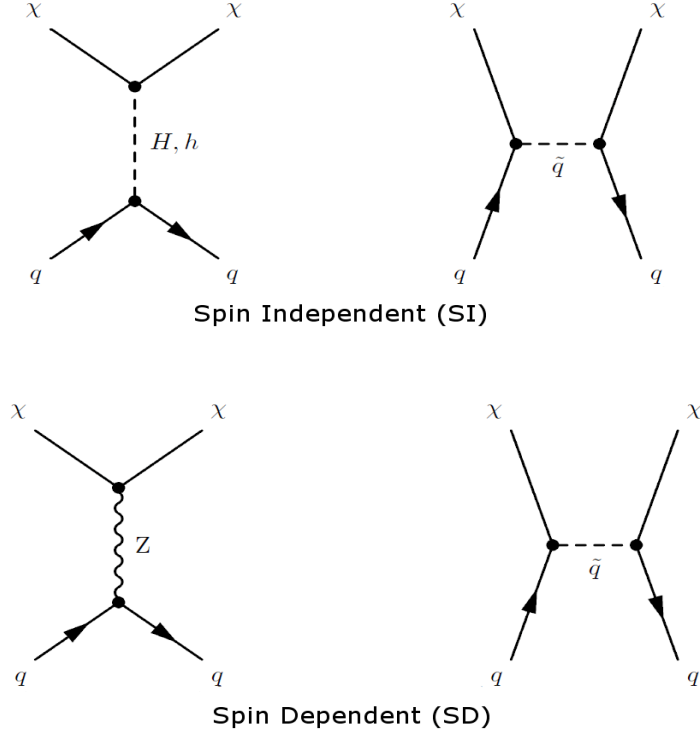
2.2 Cross section

In the previous section, the total rate R_0 was shown to be proportional to the WIMP-nucleus cross section. The cross section can be calculated by assuming certain sets of parameters in the MSSM model [10, 26, 27]. In this subsection, the elastic scattering cross section of SUSY neutralino and nucleus is discussed.

2.2.1 Lagrangian

The MSSM Lagrangian framework leads to the following low-energy effective Lagrangian, $\mathscr{L}_{\rm eff}$, which is suitable for describing elastic neutralino-quark interactions[26].

$$\mathcal{L}_{\text{eff}} = \overline{\chi}\gamma^\mu\gamma^5\chi\overline{q}_i\gamma_\mu(\alpha_{1i} + \alpha_{2i}\gamma^5)q_i$$
$$+ \alpha_{3i}\overline{\chi}\chi\overline{q}_iq_i$$
$$+ \alpha_{4i}\overline{\chi}\gamma^5\chi\overline{q}_i\gamma^5q_i \qquad (2.19)$$
$$+ \alpha_{5i}\overline{\chi}\chi\overline{q}_i\gamma^5q_i$$
$$+ \alpha_{6i}\overline{\chi}\gamma^5\chi\overline{q}_iq_i$$

where χ and q denote neutralino and quarks. The Lagrangian should be summed over quark generations, and the subscript i refers to up-type $i = 1$ and down-type $i = 2$ quarks. The terms with coefficients α_{1i}, α_{4i}, α_{5i} and α_{6i} depend on the velocity and are suppressed because the velocity is non-relativistic in an elastic neutralino-quark scattering. Coefficients α_{2i} and α_{3i} contribute to the Spin-Independent(SI) and Spin-Dependent(SD) interactions, respectively, and Feynman diagrams of these interactions are shown in Figure 2.3.

Figure 2.3: Feynman diagrams of neutralino-quark elastic scattering. Upper set is SI and lower set is SD, respectively.

2.2.2 Spin Independent(SI) cross section

The cross section of SI interaction is written as

$$\sigma^{\text{SI}}_{\chi-\text{N}} = \frac{4\mu^2_{\chi-\text{N}}}{\pi}[Zf_{\text{p}} + (A - Z)f_{\text{n}}]^2, \qquad (2.20)$$

where Z and A are the atomic number and mass number of a target, respectively. $\mu_{\chi-N}$ is the reduced mass of the neutralino mass M_D and a target mass M_N,

$$\mu_{\chi-N} = \frac{M_D M_N}{M_D + M_N} \qquad (2.21)$$

f_p and f_n are proton-neutralino and neutron-neutralino SI couplings, respectively. They are written as the sum of the neutralino-quarks SI couplings, $f_{T_q}^{(p)}$ and $f_{T_q}^{(n)}$ as

$$\frac{f^{(p)}}{M_p} = \sum_{q=u,d,s} f_{T_q}^{(p)} \frac{\alpha_{3q}}{M_q} + \frac{2}{27} f_{T_{TG}}^{(p)} \sum_{q=c,t,b} \frac{\alpha_{3q}}{M_q} \qquad (2.22)$$

$$\frac{f^{(n)}}{M_n} = \sum_{q=u,d,s} f_{T_q}^{(n)} \frac{\alpha_{3q}}{M_q} + \frac{2}{27} f_{T_{TG}}^{(n)} \sum_{q=c,t,b} \frac{\alpha_{3q}}{M_q}, \qquad (2.23)$$

where M_p, M_n and M_q are the mass of the proton, the neutron and quarks, respectively. The numerical value of the $f_{T_q}^{(p)}, f_{T_q}^{(n)}, f_{T_{TG}}^{(p)}$ and $f_{T_{TG}}^{(n)}$ are calculated from the mass of quarks and chiral symmetry applied to baryons, as

$$f_{T_u}^{(p)} = 0.020 \pm 0.004, f_{T_d}^{(p)} = 0.026 \pm 0.005, f_{T_s}^{(p)} = 0.118 \pm 0.062, \qquad (2.24)$$

$$f_{T_u}^{(n)} = 0.014 \pm 0.003, f_{T_d}^{(n)} = 0.036 \pm 0.008, f_{T_s}^{(n)} = 0.118 \pm 0.062, \qquad (2.25)$$

$$f_{T_{TG}}^{(p)} = 1 - \sum_{q=u,d,s} f_{T_q}^{(p)}, \qquad (2.26)$$

$$f_{T_{TG}}^{(n)} = 1 - \sum_{q=u,d,s} f_{T_q}^{(n)}. \qquad (2.27)$$

In most of the cases, $f_{T_q}^{(p)} \simeq f_{T_q}^{(n)}$, therefore $\sigma_{\chi-N}^{SI} \propto \mu_{\chi-N}^2 A^2$ is practically derived. Thus, the cross section of SI interaction is written by using neutralino-proton SI cross section $\sigma_{\chi-p}^{SI}$,

$$\sigma_{\chi-N}^{SI} = \sigma_{\chi-p} \frac{\mu_{\chi-N}^2}{\mu_{\chi-p}^2} A^2. \qquad (2.28)$$

Equation (2.28) indicates that a target element with large A is effective for SI-interacting neutralinos. Figure 2.4 shows the SI cross sections normalized by neutralino-proton SI cross section for some target nucleus.

2.2.3 Spin Dependent(SD) cross section

The cross section of SD interaction is written as

$$\sigma_{\chi-N}^{SD} = \frac{32}{\pi} G_F^2 \mu_{\chi-N}^2 (a_p \langle S_p \rangle + a_n \langle S_n \rangle)^2 \frac{J+1}{J}, \qquad (2.29)$$

where $G_F(= 1.166 \times 10^{-5} \text{GeV}^{-2}(\hbar c)^3)$ is the Fermi coupling constant, $\langle S_p \rangle$ and $\langle S_n \rangle$ are expectation values of spin of proton and neutron in the nucleus, J is the total spin of the nucleus. a_p and a_n consist of the sum of quark components as
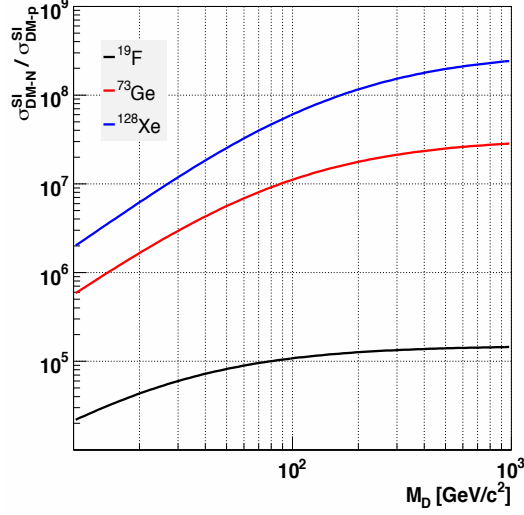
Figure 2.4: SI cross sections normalized by neutralino-proton SI cross section, $\sigma^{SI}_{\chi-N}/\sigma^{SI}_{\chi-p}$ as a functio of neutralino mass. Black, red and blue line shows target difference as ^{19}F, ^{73}Ge and ^{128}Xe

$$a_{\mathrm{p}} = \sum_{q-u,d,s} \frac{\alpha_{2q}}{\sqrt{2}G_{\mathrm{F}}} \Delta^{(\mathrm{p})}_q, \tag{2.30}$$

$$a_{\mathrm{n}} = \sum_{q-u,d,s} \frac{\alpha_{2q}}{\sqrt{2}G_{\mathrm{F}}} \Delta^{(\mathrm{n})}_q, \tag{2.31}$$

where $\Delta^{(\mathrm{p})}_q$ and $\Delta^{(\mathrm{n})}_q$ are the quark spin contents of the nucleon, and are calculated

$$\Delta^{(\mathrm{p})}_u = \Delta^{(\mathrm{n})}_d = 0.78 \pm 0.02, \tag{2.32}$$

$$\Delta^{(\mathrm{p})}_d = \Delta^{(\mathrm{n})}_u = -0.48 \pm 0.02, \tag{2.33}$$

$$\Delta^{(\mathrm{p})}_s = \Delta^{(\mathrm{n})}_s = -0.15 \pm 0.02. \tag{2.34}$$

Using Lande factor $\Lambda = \frac{a_{\mathrm{p}}\langle S_{\mathrm{p}}\rangle + a_{\mathrm{n}}\langle S_{\mathrm{n}}\rangle}{J}$, the cross section of SD interaction is written as

$$\sigma^{SD}_{\chi-\mathrm{N}} = \frac{32}{\pi} G^2_{\mathrm{F}} \mu^2_{\chi-\mathrm{N}} \Lambda^2 J(J+1). \tag{2.35}$$

The spin-dependent interaction can only occur for nuclei with nonzero spin. Only nuclei with an odd number of either protons or neutrons can have nonzero spin. As for such nuclei, Λ is approximated using S_{odd} determined from measured magnetic momentum μ_{mag}, as

$$\Lambda \approx \frac{a_{\mathrm{odd}}S_{\mathrm{odd}}}{J}, \tag{2.36}$$

$$S_{\mathrm{odd}} \approx \frac{\mu_{\mathrm{mag}} - g^l_{\mathrm{odd}}J}{g^s_{\mathrm{odd}} - g^l_{\mathrm{odd}}}. \tag{2.37}$$

23

where subscript "odd" refers an unpaired nucleon; p(proton) or n(neutron). g^l_{odd} and g^s_{odd} are the orbital and spin nucleon g-factor; $g^l_{\text{p}} = 1, g^l_{\text{n}} = 0, g^s_{\text{p}} = 5.586$ and $g^s_{\text{n}} = -3.826$. The list of the spin J, measured μ_{mag} and the calculated $\Lambda^2 J(J+1)/a_{\text{odd}} (\equiv \lambda^2 J(J+1))$ are in Table 2.1 for some target nucleus. For experimental use, the SD cross section is written using $\sigma^{\text{SD}}_{\chi-\text{p}}$ as

$$\sigma^{\text{SD}}_{\chi-\text{N}} = \sigma^{\text{SD}}_{\chi-\text{p}} \frac{\mu^2_{\chi-\text{N}}}{\mu^2_{\chi-\text{p}}} \frac{\lambda^2 J(J+1)}{0.75}. \tag{2.38}$$

Values of $\sigma^{\text{SD}}_{\chi-\text{N}}/\sigma^{\text{SD}}_{\chi-\text{p}}$ and $\sigma^{\text{SD}}_{\chi-\text{N}}/\sigma^{\text{SD}}_{\chi-\text{n}}$ for some target nucleus are shown in Figure 2.5 and Figure 2.6, respectively.
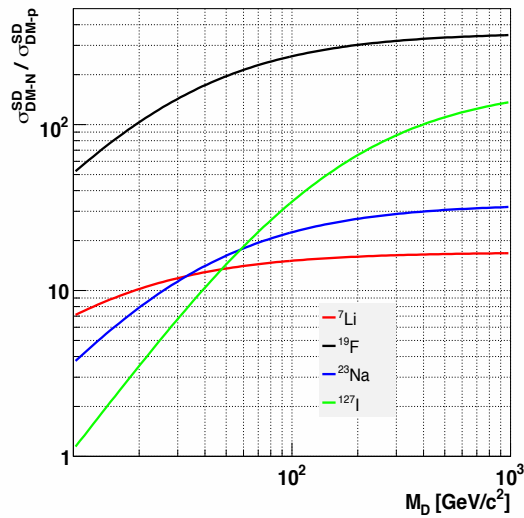
Figure 2.5: SD cross sections normalized by neutralino-neutron SD cross section, $\sigma^{\text{SD}}_{\chi-\text{N}}/\sigma^{\text{SD}}_{\chi-\text{p}}$ as a function of neutralino mass. Red, black, blue and green line shows target difference as ^{7}Li, ^{19}F, ^{23}Na and ^{127}I, respectively.
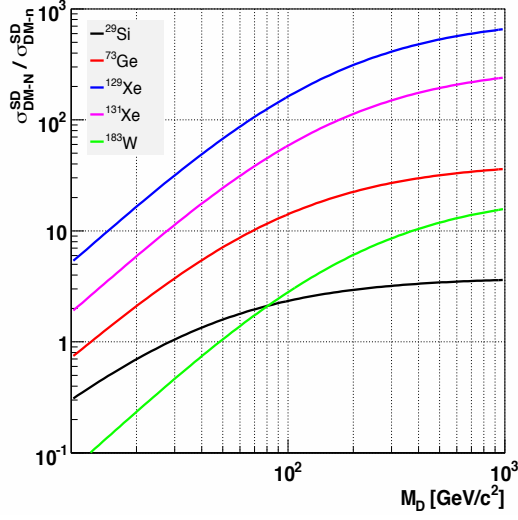
Figure 2.6: SD cross sections normalized by neutralino-proton SD cross section, $\sigma^{\mathrm{SD}}_{\chi-\mathrm{N}}/\sigma^{\mathrm{SD}}_{\chi-\mathrm{n}}$ as a function of neutralino mass. Black, red, blue, pink, green line shows target difference as ^{29}Si, ^{73}Ge, ^{129}Xe, ^{131}Xe and ^{183}W, respectively,

Table 2.1: The spin J, measured μ_{mag} and the calculated $\lambda^2 J(J+1)$ for some nucleus.

Isotope	J	Abundance(%)	μ_{mag}	$\lambda^2 J(J+1)$	unpared necleon
^{1}H	1/2	100	2.793	0.750	proton
^{7}Li	3/2	92.5	3.256	0.244	proton
^{11}B	3/2	80.1	2.689	0.112	proton
^{15}N	1/2	0.4	-0.283	0.087	proton
^{19}F	1/2	100	2.629	0.647	proton
^{23}Na	3/2	100	2.218	0.041	proton
^{127}I	5/2	100	2.813	0.007	proton
^{133}Cs	7/2	100	2.582	0.052	proton
^{3}He	1/2	1.0×10^{-4}	-2.128	0.928	proton
^{17}O	5/2	0.0	-1.890	0.342	proton
^{29}Si	1/2	4.7	-0.555	0.063	proton
^{73}Ge	9/2	7.8	-0.879	0.065	proton
^{129}Xe	1/2	26.4	-0.778	0.124	proton
^{131}Xe	3/2	21.2	0.692	0.055	proton
^{183}W	1/2	14.3	0.118	0.003	proton

2.3 Form factor

When the de Broglie wavelength h/q with the momentum transfer q is no longer large compared to the nuclear radius, where h is the Planck constant and $q = \sqrt{2M_{\mathrm{N}}E_{\mathrm{R}}}$ is the momentum of the recoil nuclei for a recoil energy of E_{N}, the effective cross section begins to fall for large q cases. This effect is referred to as a "form factor". The effective neutralino-nucleus cross section is corrected with this form factor as

$$\sigma(qr_{\mathrm{n}}) = \sigma_0 F^2(qr_{\mathrm{n}}), \qquad (2.39)$$

where σ_0 is the cross section at a zero momentum transfer and F is a function of the dimensionless quantity, qr_{n}, where r_{n} is an effective nuclear radius. In the first Born (plane wave) approximation, the form factor is given by Fourier transformation of the density distribution of the 'scattering centres', $\rho(r)$, as

$$
\begin{aligned}
F(qr_{\mathrm{n}} &= \int \rho(r) e^{i\boldsymbol{q}\cdot\boldsymbol{r}} \boldsymbol{dr} \\
&= \frac{4\pi}{q} \int_0^\infty r\sin(qr)\rho(r)dr.
\end{aligned}
\qquad (2.40)
$$

For the SI interaction, since neutralino would interact with any of the nucleon, the nuclei can be approximated as a solid sphere. In this case, the form factor is written using Bessel function $j_i(x) = (\sin(x) - x\cos(x))/x^2$ as

$$F(qr_{\mathrm{n}}) = 3\frac{j_1(qr_{\mathrm{n}})}{qr_{\mathrm{n}}}\exp(-\frac{(qs)^2}{2}), \qquad (2.41)$$

where $r_{\mathrm{n}} \simeq 1.14A^{1/3}$ fm, and $s \simeq 0.9$ fm representing the nuclear skin thickness. Figure 2.7 shows the SI form factors of some isotopes as a function of the recoil energy E_{R}. Expected energy spectra of SI interaction with ^{19}F target is shown in Figure 2.8, where the form factor is taken into account.

For the SD interaction, since neutralino would interact with the surplus nucleon, the nuclei can be approximated as a thin shell, and this assumption is called the odd-group model. In this case, the form factor is written using Bessel function $j_0 = \sin(x)/x$ as
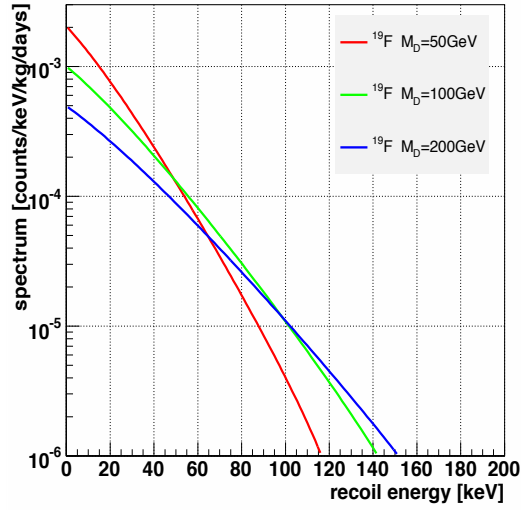
$$F(qr_{\mathrm{n}} = j_0(qr_{\mathrm{n}}), \qquad (2.42)$$

where $r_{\mathrm{n}} \simeq 1.0A^{1/3}$ fm. Figure 2.9 shows the SD form factors of some isotopes as a function of the recoil energy E_{R}. Expected energy spectra of SD interaction with ^{19}F target is shown in Figure 2.10, where the form factor is taken into account.
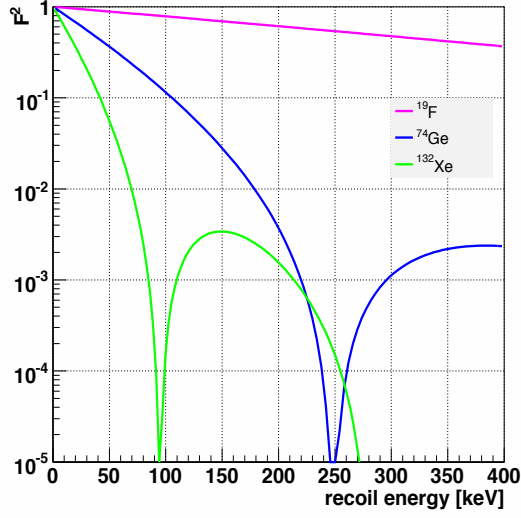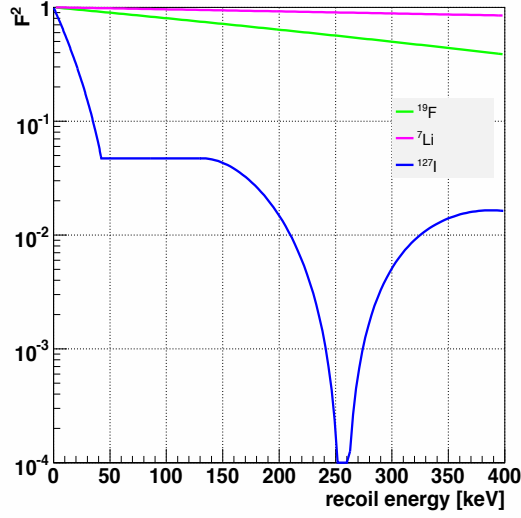
Figure 2.7: The SI form factors of some isotopes as a function of the recoil energy E_R. Pink, blue and green lines show target isotopes of ^{19}F, ^{74}Ge, ^{123}Xe, respectively.

Figure 2.8: The expected energy spectra of SI interaction with ^{19}F target, where $\sigma^{\mathrm{SI}}_{\chi-\mathrm{p}} = 10^{-6}$ pb is assumed. Red, green and blue lines show the cases for the neutralino mass of $M_{\mathrm{D}} = 50, 100$ and 200 GeV/c^2, respectively.

Figure 2.9: The SD form factors of some isotopes as a function of the recoil energy E_R. Green, pink, blue and green lines show target isotopes of ^{7}Li, ^{19}F, ^{127}I, respectively.
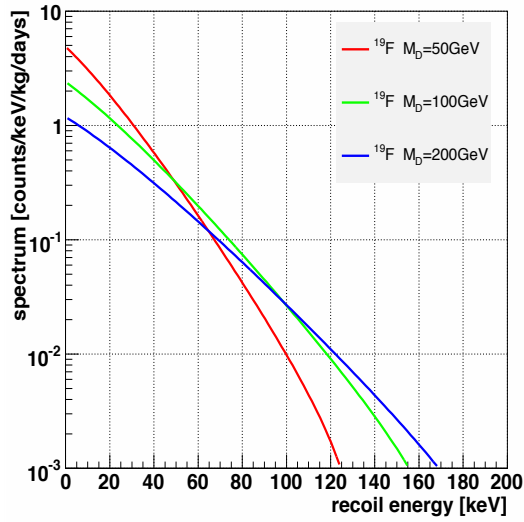
Figure 2.10: The expected energy spectra of SD interaction with ^{19}F target, where $\sigma^{\mathrm{SD}}_{\chi-\mathrm{p}} = 1$ pb assumed. Red, green and blue lines show the cases for the neutralino mass of $M_{\mathrm{D}} = 50, 100$ and 200 GeV/c^2, respectively.

2.4 Dark matter signal

We need to observe a distinct signature in order to claim a clear detection of the dark matter because the expected spectrum itself has featureless exponential shape as shown in Figure 2.8 and Figure 2.10. Distinct signatures can be caused by the nuclear-dependence of the neutralino-necleus reactions, the relative motion of Solar system to the galactic halo, and that of the Earth to the galactic halo. They can be observed as the signatures listed below.

- Nuclear target dependence of the event rate
- Annual modulation of the event rate and the shape of the spectrum
- Directional dependence of the event rate

These signals are discussed in the following subsections.

2.4.1 Nuclear target dependence

The shape of the expected energy spectrum dR/dE_R depends on the isotopes for the following reasons. First, the mass number A affects the reduced mass as Equation (2.21), thus the expected event rate becomes high for the target mass close to the assumed neutralino mass. Second, the mass number and the reduced mass affect the SI cross section as Equation (2.28), thus the expected event rate becomes higher for larger mass number isotopes. Third, the $\lambda^2 J(J+1)$ term and the reduced mass affect the SD cross section as Equation (2.38), thus some isotopes with the large $\lambda^2 J(J+1)$ term, such as ^{19}F, ^{3}He and so on, have large SD cross sections. Fourth, the mass number A affects the form factor as Equation (2.41) and Equation (2.42), thus the effective cross section become small for large mass number isotopes. Figure 2.11 and Figure 2.12 are the expected energy spectra dR/dE_R of various targets for the SI-interacting and the SD-interacting neutralino, respectively. Here $M_{\mathrm{D}} = 100 \ \mathrm{GeV}/c^2$, $\sigma^{\mathrm{SI}}_{\chi-\mathrm{p}} = 1 \times 10^6$ pb and $\sigma^{\mathrm{SD}}_{\chi-\mathrm{p}} = 1$ pb are assumed. From Figure 2.11 and Figure 2.12, it can be judged that the difference of the event rate between isotopes can be a distinct signal of dark matter. It should be noted, however, the background also depends on the isotopes, thus it is difficult to claim a dark matter detection strongly by using only this signal.

2.4.2 Annual modulation

The annual modulation of the event rate is caused by the Earth's motion around the Sun as described in Equation (2.1). The velocity of the Earth relative to our galaxy, v_{E}, become maximum in June 2nd and minimum in December 4th, and the order of modulation size is less than $O(v_{\mathrm{orb}}/v_{\mathrm{sun}}) \sim 5\%$. Figure 2.13 illustrates the expected modulation of the energy spectrum between June and December, where the target is ^{19}F for the SD interaction, $M_{\mathrm{D}} = 100 \ \mathrm{GeV}/c^2$ and $\sigma^{SI}_{\chi-p} = 1$ pb. In order to detect such a tiny annual modulation, we need to take large statistics using a large mass detector such as solid or liquid detector. The experimental results of annual modulation will be discussed in section 3.1
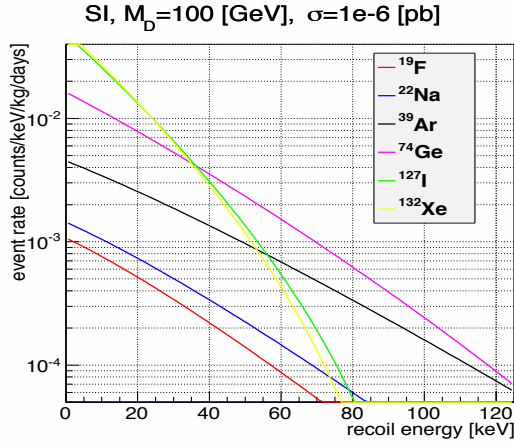
Figure 2.11: The expected energy spectrum dR/dE_{R} of various targets for the SI-interacting neutralino with a mass of $M_{\mathrm{D}} = 100$ GeV$/c^2$ and $\sigma^{SI}_{\chi-p} = 10^{-6}$ pb.
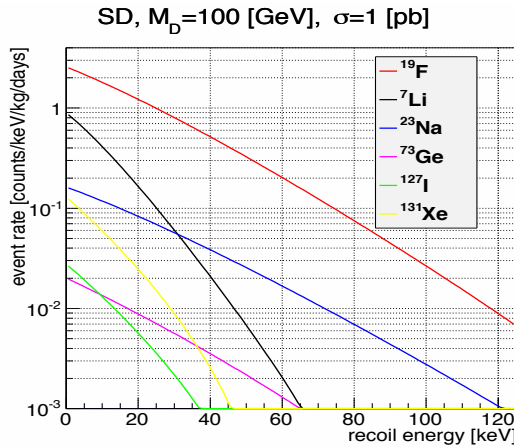
Figure 2.12: The expected energy spectrum dR/dE_{R} of various targets for the SD-interacting neutralino with a mass of $M_{\mathrm{D}} = 100$ GeV$/c^2$ and $\sigma^{SI}_{\chi-p} = 1$ pb.
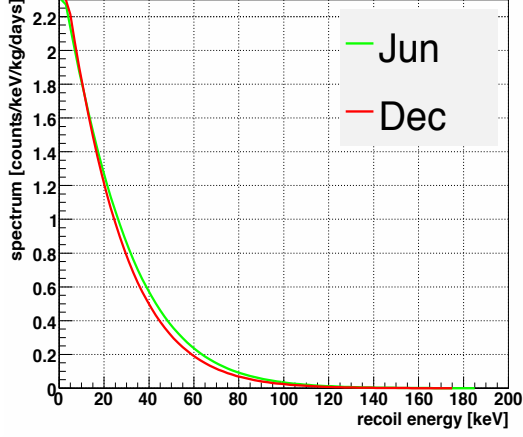
Figure 2.13: The expected modulation of energy spectrum between Jun. and Dec., where the target is ^{19}F for the SD interaction, M $= 100$ GeV$/c^2$, $\sigma_{\chi-p}^{SD} = 1$ pb.

2.4.3 Directionality

The most convincing signal of the dark matter would be seen in the directional distribution of the recoil nucleus. Since the Cygnus constellation is seen in the forward direction of the Solar system's motion, dark matters would seem to be coming from the Cygnus direction like "WIMP-wind". Since the Cygnus direction is varying per hour and per day, the systematic error due to the daily and seasonal environmental changes will be canceled.

In the laboratory system, expected angular spectrum of recoil nucleus is written as

$$\frac{d^2R}{dE_R d\cos\theta} \simeq \frac{1}{2}\frac{R_0}{E_0 r}\exp\left[\frac{-(v_{\mathrm{E}}\cos\theta - v_{\min})^2}{v_0^2}\right], \tag{2.43}$$

where angle θ is formed by the WIMP-wind direction and the recoil nuclei direction[28]. Figure 2.14 shows the expected angle-energy distribution, where the target is ^{19}F for the SD interaction, M $= 100$ GeV$/c^2$, and $\sigma_{\mathrm{SD}} = 1$ pb. Figure 2.15 shows the expected cos θ distribution obtained by selecting the events with recoil energy of $100 - 120$ keV in Figure 2.14.

Since an isotropic background makes flat cosθ distribution, asymmetric cosθ distribution in Figure 2.15 can be a strong evidence of the dark matter detection.
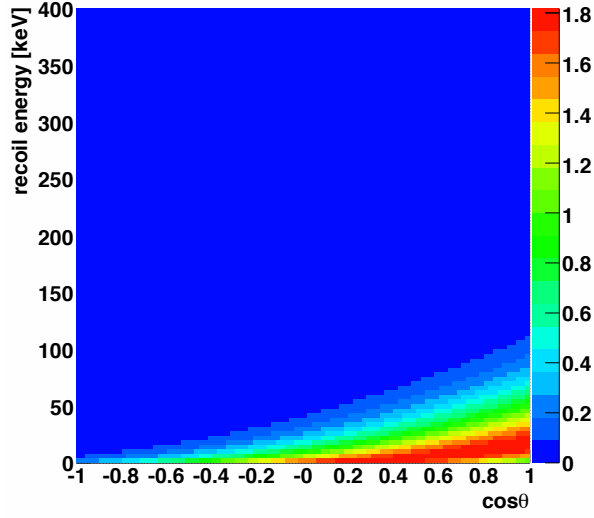
Figure 2.14: The expected angle-energy distribution, where the target is ^{19}F for the SD interaction, M = $100\mathrm{GeV}/c^2$, $\sigma^{SD}_{\chi-p} = 1$ pb, θ is the angle formed by the WIMP-wind direction and recoil nuclei direction. The color bar represent the event rate with an unit of [count/keV/kg/days/ $\cos\theta$]
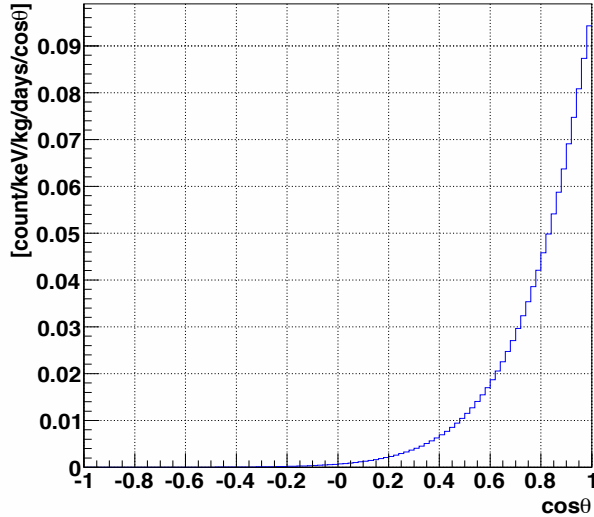
Figure 2.15: The expected $\cos\theta$ distribution ($100 - 120$ keV), where the target is ^{19}F for the SD interaction, M = 100 GeV/c^2, $\sigma^{SD}_{\chi-\mathrm{p}} = 1$ pb , θ is the angle formed by the WIMP-wind direction and the recoil nuclei direction.

Chapter 3

Review of Dark Matter Search

A number of experiments have been carried out to detect WIMP-nucleus elastic scatterings. In the direct search experiments, detectors are designed to detect recoil energy of typically less than 100 keV via photons, phonons or charges. In general, direct dark matter detectors should have following three characteristics.

- Low energy threshold
  The shape of the expected energy spectrum is exponential-like. Then, the lower the threshold energy is, the more number of signals is expected. A relevant energy region is considered to be below 100 keV.
- Large mass
  Since the direct detection of the dark matter is a rare event search, a large target mass is required to accumulate sufficient statistics in a reasonable observation time. Typical required mass is from kilogram to ton.
- Low background
  Typical techniques of low radioisotope background such as a material selection and shielding are important to WIMP detectors. Basically, the detector is settled in the underground laboratories to reduce the background induced by cosmic-rays. In addition, particle identifications using additional signals are useful to discriminate backgrounds.

Direct dark matter search experiments are roughly categorized into two types in terms of the signals obtained; the conventional type and the direction-sensitive type. Whereas a conventional detector measures only the energy of the nuclear recoil, a direction-sensitive type also obtains the directional information of nuclear recoil tracks which can provide a strong evidence of the dark matter detection. A detector with a high position resolution is required for the direction-sensitive search because the typical track length is less than 1 mm in atmospheric pressure gas. A majority of the experimental groups in the direct dark matter search field adopt "conventional method" to make use of the well-established large mass detectors. Direct detection experiments are reviewed in this chapter.

3.1   Conventional experiment

Almost all direct dark matter search experiments use solid or liquid detectors to have a large target mass. The recoil energy is converted to photon, heat and ionization. The

detectors are categorized as follows; solid scintillators and liquid noble gas scintillators for detecting only the photon, liquid noble gas scintillators for detecting the photon and ionization, semiconductor bolometers for detecting the ionization and heat, crystal bolometers for detecting photon and heat, bubble chambers for detecting the ionization. Results of the direct dark matter search are summarized in Figure 3.1 and Figure 3.2 [14]. In these plots, the WIMP-proton cross sections are shown as a function of the WIMP mass. The lines are exclusion lines which is the upper limits for the cross section. The areas are, in contrast, the allowed region where the results indicates the existence of a dark matter particle in that phase space. The latest results of SI WIMP-nucleon elastic cross sections are shown in Figure 3.3 [20, 19] and spin-dependent WIMP-proton elastic scattering cross sections as a function of WIMP mass in Figure 3.4 [21]. Details on the conventional detector experiments are described in the following subsections.
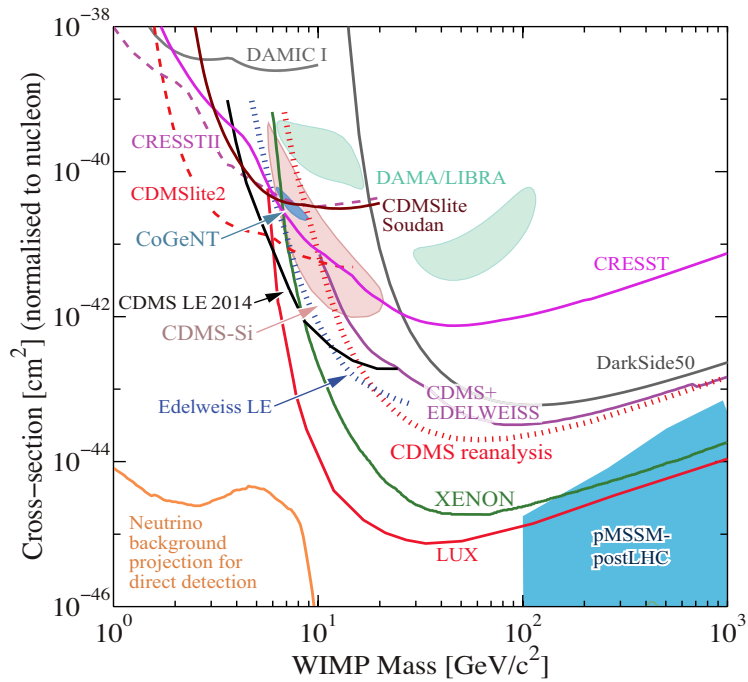

Figure 3.1: WIMP cross sections (normalized to a single nucleon) for spin-independent coupling versus WIMP mass [14]. The DAMA/LIBRA, CDMS-Si, and CoGeNT enclosed areas are regions of interest from possible signal events. For context, the blue shaded region shows a scan of the parameter space of the pMSSM, a version of the MSSM with 19 parameters, by the ATLAS collaboration, which integrates constraints set by LUX and ATLAS Run 1; the favored region is around 10^{-46}cm^2 and 500 GeV.

3.1.1 Solid scintillator

Scintillators have advantages in constructing large mass detectors and well-studied properties. Many types of scintillators, such as NaI(Tl), CsI(Tl), have been used for dark matter searches. DAMA group conducted a dark matter search with a highly radio-pure
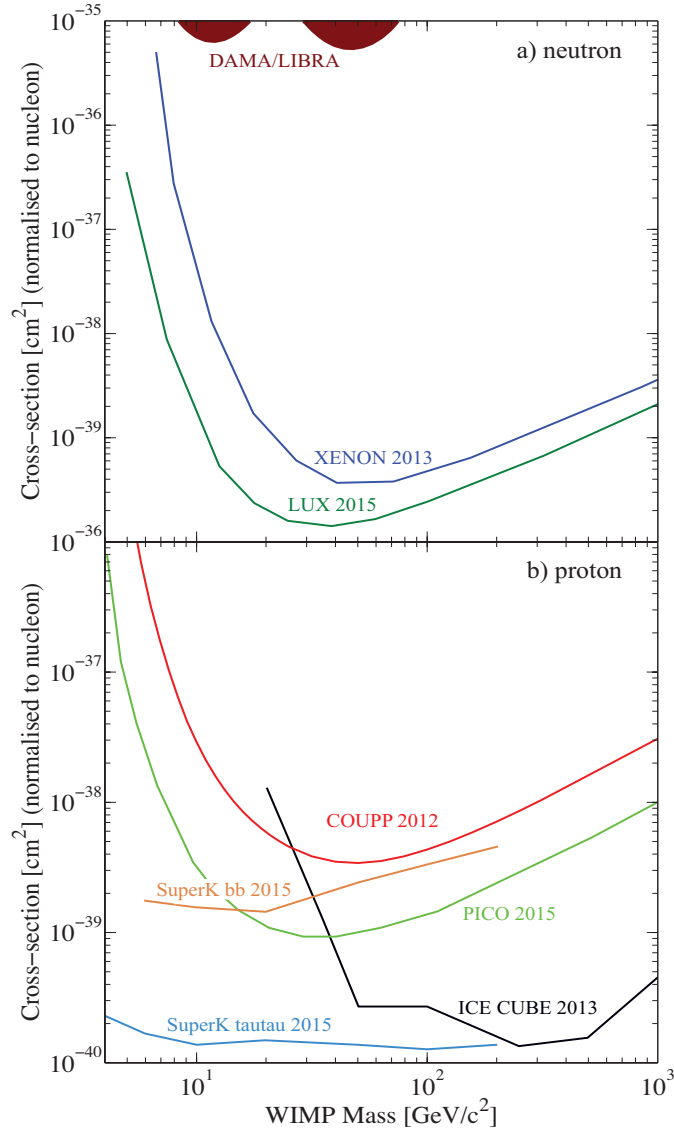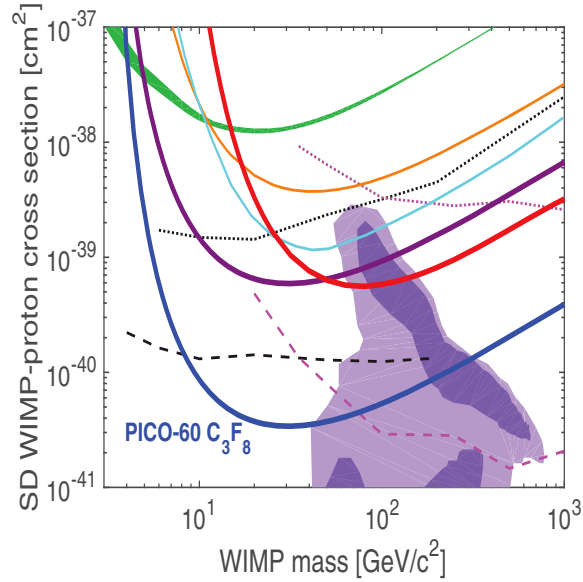
Figure 3.2: WIMP cross sections for spin dependent coupling versus mass [14]. (a) interactions with the neutron; (b) interactions with the proton. Indirect detection results are from SuperKamiokande (annihilation into $b\bar{b}$ and $\tau^{+}\tau^{-}$ channels) together with IceCube (annihilation into $W^{+}W^{-}$).
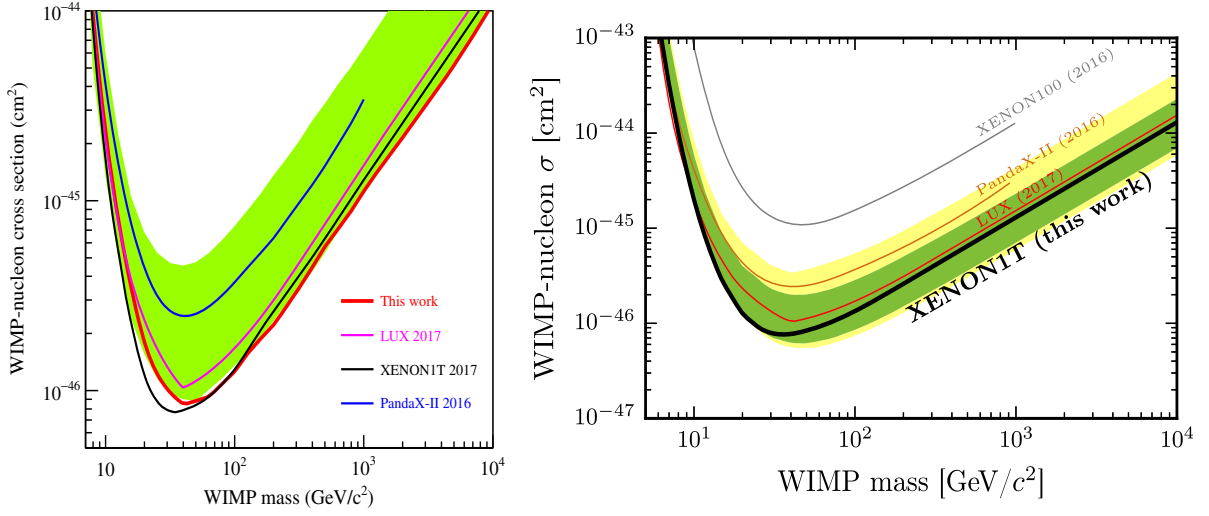
Figure 3.3: The 90% C.L. upper limits versus WIMP mass for the spin-independent WIMP-nucleon elastic cross sections from the combined PandaX-II Run 9 and Run 10 data (red), overlaid with that from PandaX-II 2016 [3] (blue)(Left)[20]. XENON1T(black line)(Right)[19].

Figure 3.4: spin-dependent WIMP-proton elastic scattering cross sections as a function of WIMP mass.[21]

100 kg NaI(Tl) setup for seven years and claimed to have detected an annual modulation signature due to the dark matter [29]. Allowed parameter regions of WIMPs are shown as enclosed regions in Figure 3.1 and Figure 3.2. The DAMA/LIBRA experiment accumulated larger exposure (1.17 ton · year) with a detector of total 250kg and claimed a positive signature of the dark matter. However, it is also pointed out that this annual modulation signal could have arised from seasonal fluctuating background because several experiments have obtained lower cross section limits. Experiments using NaI in other sites [30, 31] are being performed and prepared to confirm the DAMA 's signal. In addition, a direction-sensitive experiment can provide a distinct signal of dark matter without seasonal systematic error. KIMS using 34.8 kg of CsI(Tl) set a better SD limits with a 3490 kg · days of exposure [34] .

3.1.2   Liquid nobel-gas scintillator

Liquid noble gases are excellent scintillators, and furthermore, ionization signals can be collected with an existence of a certain electric field. Particularly, liquid xenon (LXe) have a good intrinsic properties of large mass number, high density, high radio purity, and high light output. Though the mass number of liquid argon (LAr) is less than that of LXe, LAr has the advantage of being low cost and better particle identification power. There are two types of liquid noble-gas dark matter detectors. One is a single phase detector which detects only a scintillation signal by photon detectors. Single phase detectors are constructed as simple as possible to reduce the background from detector itself. Environmental gamma-ray background can be rejected by the self shielding, and a pulse shaping analysis could used for the nuclear recoil discrimination. The other is a two phase detector which has a gas phase above the liquid phase and detects not only the scintillation signal but also the ionization signal. The ionization signal is detected as a gas amplification scintillation signal in the gas phase caused by the primary electron drifted out of the liquid phase. The ionization signals for electron recoils are larger than that of nuclear recoils. Therefore, the ratio of the ionization signal and the primary scintillation signal provides a powerful electron discrimination power. XMASS[36] and DEAP[37] are the single phase detectors using LXe. XMASS using 832 kg of liquid xenon performed the direct dark matter search with 359.2 live days times 832 kg of exposure. DEAP-3600 was performed 2 km underground at SNOLAB utilizing a large target mass, with the LAr target contained in a spherical acrylic vessel of 3600 kg capacity with 4.44 live days (fiducial exposure of 9.87 tonne days). As two phase detectors using LXe, there are LUX [38],PandaX-II[20] and XENON1T [19]. LUX using 250 kg of LXe performed a dark matter search with a 3.35×10^4 kg days exposure and obtained the best limit for the SI interacting WIMP in the mass range of 50 GeV/c^2. PandaX-II using 580 kg of LXe performed the dark matter search with a total exposure of 5.4×10^4 kg day, the most stringent upper limit on the spin-independent WIMP-nucleon cross section is set for a WIMP with mass larger than 100 GeV/c^2, with the lowest 90% C.L. exclusion at 8.6×10^{-47}cm^2 at 40 GeV/c^2. XENON1T using $\sim$ 1042 kg of fiducial mass performed the dark matter search with 34.2 live days and derive the most stringent exclusion limits on the spin-independent WIMP-nucleon interaction cross section for WIMP masses above 10 GeV/c^2, with a minimum of 7.7×10^{-47}cm^2 for 35 GeV/c^2 WIMPs at 90% C.L.

3.1.3 Semiconductor detector

In the direct search using bolometers, the nuclear recoil energy is detected via phonons (temperature rising). The heat capacity of a dielectric crystal is proportional to T^3 at the low temperature, thus at the mK temperature, the small energy deposition from a nuclear recoil can yield a measurable increase of the temparture. Since the electron-hole pairs is also generated at the same time in the semiconductor bolometers, electron background can be discriminated by using the difference of ionization/phonon ratio. In addition, some groups have developed "scintillating bolometers" which detect scintillation photons together with heat as an alternative method for the electron event rejection. superCDMS experiment operated towers of Ge crystals (each of mass is 600 g) with a thickness of 25 mm cooled down to 10 mK [40]. CoGeNT project uses 443g of p-type point contact Ge detector with a low-threshold of 0.4 keV, and performed a dark matter search with an exposure of $\sim$ 200 kg $\cdot$ days [41]. In the low energy region, the annual modulation of event rate was observed by CoGent for over one year at $\sim 2.8\,\sigma$, and obtained the allowed region at low mass region as shown in the upper panel of Figure 3.1. EDELWEISS-III experiment using (820 to 890 g) mass performed the dark matter search with fiducial exposure of 496 kg $\cdot$ days [42]. CRESST-II experiment uses 5 kg of $CaWO_4$ crystals and read two types of signals, a phonon signal and coincidently produced scintillation light for electron discrimination [43]. After an exposure of 52 kg $\cdot$ live-days CRESST-II set the allowed region as shown in the upper panel of Figure 3.1. DAMIC experiment uses low noise CCD with a very low energy threshold of 40 eV, and is dedicated to the search for low-mass WIMP [44]. They performed a dark matter search using a CCD of 1 g with an exposure of 1.5 kg $\cdot$ day, and obtained the best limit in the low-mass region.

3.1.4 Bubble chamber

Bubble chambers are the detector made of superheated liquids. Bubble chambers are kept in a delicate metastable superheated state, and ionizing radiation particle makes a local vapor phase with the energy deposition along its path. Rapidly growing bubbles are photographed and the chamber is then reset by a fast recompression to the metastable liquid phase. These devices have advantages of the electron discrimination, a large mass, and a target selection for the SD WIMP searches. But they have disadvantage of being a threshold-type detector, or no way to to detect the nuclear recoil energy. The superheated liquid can be tuned to respond exclusively to particles with a large stopping power, so that muon and electron events all fall well below the bubble nucleation threshold. PICO [21], SIMPLE [46], PICASSO [47] experiments applied a superheated droplet detector for the direct dark matter search using piezoelectric sensors as the trigger. PICO60 performed a dark matter search using 52 kg of C_3F_8 bubble chamber with an exposure of 1167 kg $\cdot$ days. SIMPLE performed a dark matter search using 0.215 kg of C_2ClF5_5 bubble chamber with an exposure of 13.67 kg $\cdot$ days. PICASSO performed a dark matter search using 0.72 kg of ^{19}F in C_4F_{10} bubble chamber with an exposure of 114 kg $\cdot$ days. Since ^{19}F large $\lambda^2 J(J+1)$ term is used for a target of these detectors, they have strong limit for SD interaction.

3.2 Direction-sensitive experiment

Direction-sensitive experiments are to measure the incoming direction of WIMPs with detectors to measure the direction of nuclear recoil tracks. Typical length of the nuclear track with an energy of 100 keV is less than 1mm in the gas at 1atm pressure. Thus, low pressure gaseous detectors are used in many cases. As an alternative approach, it is pointed out that a high pressure noble-gas detector would provide some directional information due to the "columnar recombination effect" [48]. Direction-sensitive detectors can also be categorized by the information that got. Nuclear tracks has the information of the direction and sense, in other words a three-dimensional vector like track is the perfect detection of the nuclear track Most of the detectors are not ideal 3D-vector detectors. Some detectors only detect projected track and thus they are referred to as 2D or 1D detectors Some detectors are not sensitive to head-tail of the tracks and thus are called as axial detector.

3.2.1 Gaseous detector

Low pressure gaseous time-projection-chambers, commonly coupled with micro-patterned gaseous detectors (MPGDs), namely μ-TPCs, are widely studied for direction-sensitive dark matter searches. The requirement for the use of low pressure gas implies large volume detectors of more than 1m^3 will eventually be needed. Although the target mass density is $\sim 1/1000$ times less than that of conventional detectors, the directional signal can be a strong evidence of the detection of the dark matter.

(1) Typical feature of gaseous detectors

μ-TPC obtains a track of a charged particle in the following sequences. The detector gas is ionized along the path of a charged particle. The ionized electrons drift along the electric field that is applied along the z-axis in the gas, undergo gas amplification if necessary, then reach the 2-dimensional detector. Using x and y determined by the two dimensional detector and z determined by the time when the electron reaches the two dimensional detector. Thus a three dimensional track is obtained.

A target gas should have a large cross-section of WIMP-nucleus scatterings. The noble gases such as Xe and Ar are often used in a gas detector, in particular, the sensitivity of SI interaction is high for Xe due to the large mass number. However, the diffusion of electron during drift in the noble gas is very large and it requires fine optimizations to construct a large detector measuring fine tracks.

MAGBOLTZ [49] calculations of the diffusion constant for several gas are shown in Figure 3.5. A negative ion time projection chamber (NITPC), in which the primary electrons are rapidly captured by electro-negative gases such as CS_2 and drift as the negative ions along an electric field, has potential to realize a very small diffusion. It is because drift ions remain in or near thermal equilibrium with the gas, and diffusions are suppressed to the thermal levels. CF_4 gas, although it is not an electron negative gas, has small electron diffusions because the electron drift velocity in CF_4 gas is high as shown in Figure 3.6. CF_4 gas is easy to handle because it is inert and harmless, while CS_2 gas is ignitable and harmful.
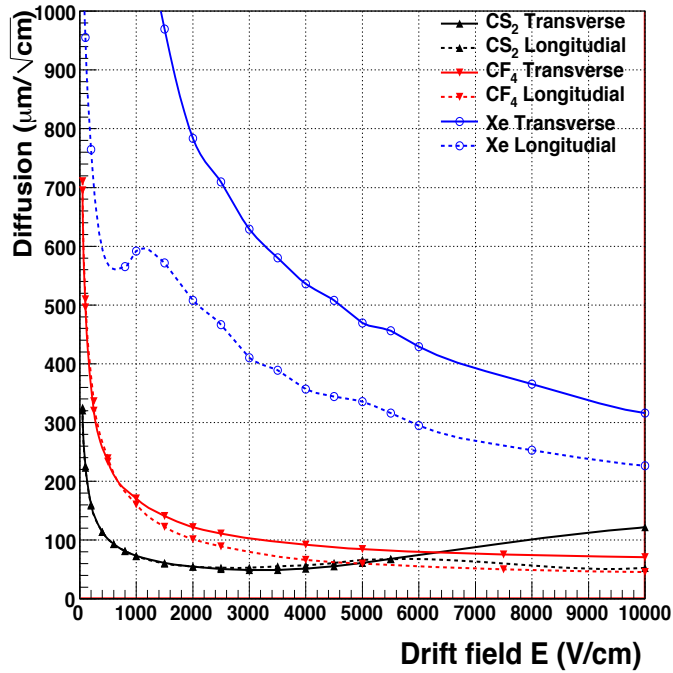
Figure 3.5: Gas diffusions of electrons or negative ions as a function of the electric field at a temperature of 300K calculated by MAGBOLTZ. Dotted and Solid line are longitudinal and transverse diffusion, respectively. Color shows the molecular; red, blue and black correspond to CF_4, Xe and CS_2, respectively.
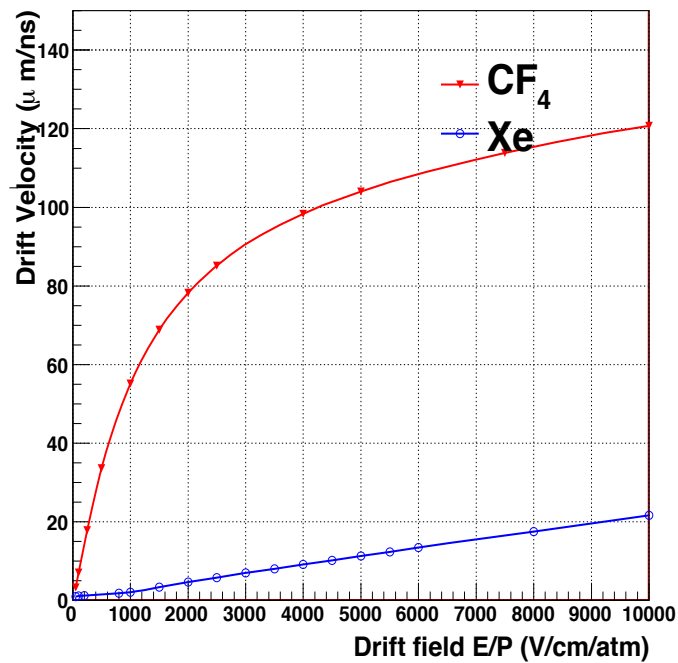

Figure 3.6: Drift velocities of electrons as a function of electric field calculated by MAGBOLTZ for CF_4(red) and Xe(blue).

We note that CS_2 gas has an advantage to the SI interaction search with large mass number of ^{32}S and CF_4 gas has an advantage to the SD interaction search with a large $\lambda^2 J(J+1)$ term. The properties of CF_4 gas are summarized in Table 3.1.

Table 3.1: Properties of CF_4 gas.

| a chemical formula	CF_4
name	carbon tetrafluoride
appearance	colorless, odorless, inert and nonpoisonous
molecular weight	88.01 g/mol
density	3.76 g/l (15C, 1 atm)
melting point	89.55 K
boiling point	145.35 K
W-value	34 eV[1] [50]

Direction-sensitive detector should have a position resolution better than a typical nuclear track length of interest. The lengths of nuclear tracks in several types of gas calculated by SRIM [52] as a function of the initial energy are shown in Figure 3.7. In the lower pressure gas, longer tracks are expected and thus a lower energy threshold is realized. But low pressure gas detector needs a large volume and also often causes the unstability of the operation. We need to overcome these difficulties in order to detect the very distinct signals of the dark matter.
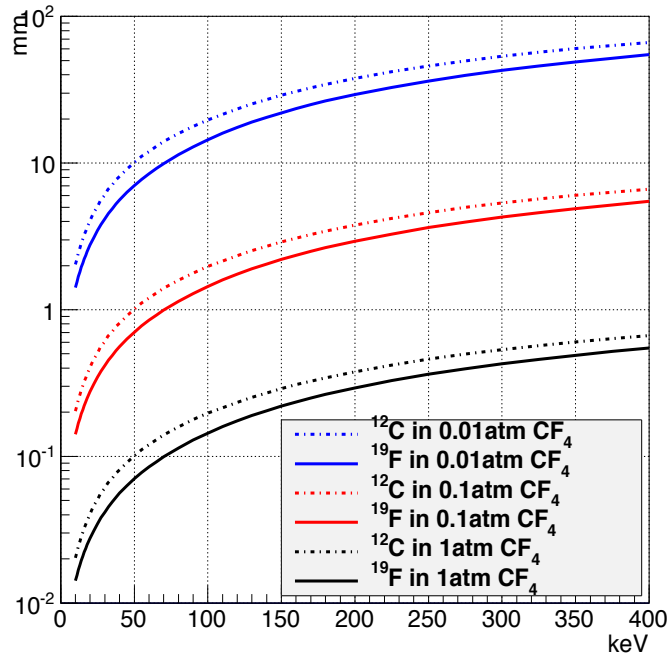
Figure 3.7: Track length of recoil ^{12}C(dotted line) and ^{19}F(solid line) in CF_4 gas calculated by SRIM with each pressure (blue:0.01atm, red:0.1atm, black:1.0atm).

---

[1]The W-value is reported elsewhere [51] which is said to be a typo .
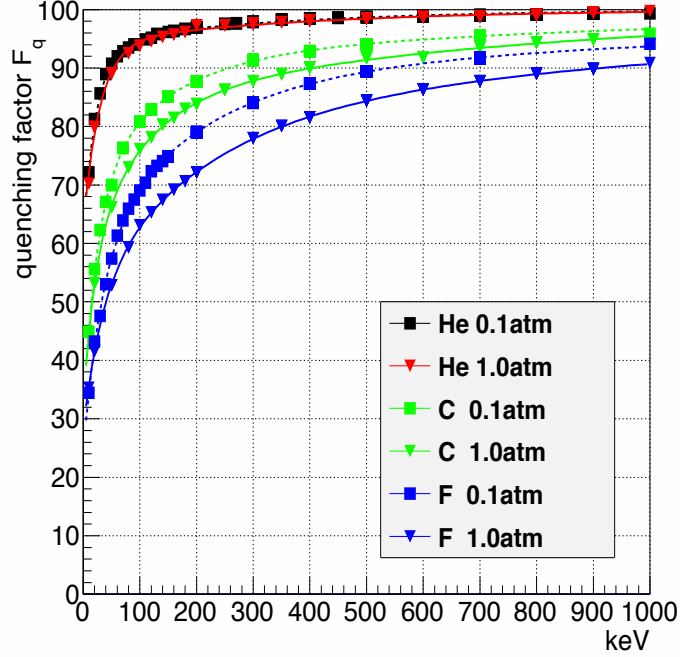
Figure 3.8: Quenching factor of various nucleus in CF_4 gas calculated by SRIM. Each line shows different nuclei-pressure combination as shown in the legend.

It is important to consider a nuclear quenching factor for low energy nuclear recoils. Nuclear quenching factor, $F_q = E_{\text{ionized}}/E_{\text{total}}$, is the ratio between total energy loss and energy used for ionization. Nuclear quenching factors for several gas detectors were summarized in [53]. The nuclear quenching factors of ^{4}He, ^{12}C and ^{19}F ions in CF_4 gas were calculated by SRIM as shown in Figure 3.8. These values have nucleus-, energy- and also gas pressure-, dependence as shown in the figure. They are used when we convert the measured (ionized) energy to the recoil (total) energy in dark matter search experiments.

## (2)   Experiments with gaseous detectors

We review the experiments with gaseous detectors and development status in the following paragraph. DRIFT experiment pioneered the study of the directional detection of the dark matter with 1m^3 of gas detectors. Particularly, they have been leading the field with the background reduction techniques [54]. They performed a dark matter search with DRIFT-IId detector for 54.7-days live time with140 g of a mixture of 30 torr CS_2, 10 torr CF_4 and 1 torr O_2 gas. They have also started R&Ds to use MPGD readouts in order to overcome their potential weakness of the readout pitch of 2 mm.

DMTPC collaboration proposed a new method to detect the recoil tracks using a CCD-readout TPC[55]. They demonstrated that the projected images of nuclear recoil tracks could be precisely taken via scintillation photons produced during the avalanche process in CF_4 gas. Although only two dimensional projected track is obtained instead of three dimensional track due to the mechanism of the readout, their technique is very notable for the detection of the track sense. In 2011, they reported the surface dark matter search result, and improved the SD direction-sensitive limit to 2.0 $\times 10^3$ pb for

115 GeV/c^2 dark matter.

MIMAC project [56] and D3 project [57] are also developing the gaseous tracker. MicroMEGAS [58] is used for MIMAC, and GEMs [59] with an ATLAS FE-I3 pixel chip [60] are used for D3. NEWAGE with CF_4 gas and a fine pitch gaseous detectors has obtained first direction-sensitive limits in 2007, and improved to 557pb for WIMP mass of 200GeV/c^2 in 2015 (Figure 3.9)[61].
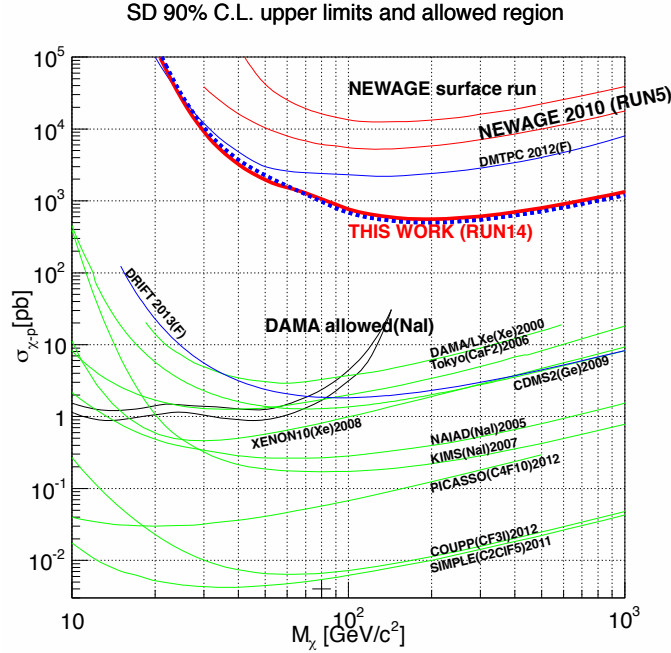
Figure 3.9: Results of direction-sensitive direct dark matter search experiments. red solid line shows the result of NEWAGE2015 [61].

3.2.2   Emulsion detector

Nuclear emulsions, though they are solid detector, can potentially be used for direction sensitive dark matter experiments because of their good position resolutions $\sim$ O(100 nm)[62]. Emulsion has AgBr in gelatin, and tiny cluster of Ag is generated along the pass of a charged particle. Then, by developing the cluster of Ag, a track of charged particle is observed by microscope. Although emulsions have no time resolution, they have advantage in scalability.

3.2.3   High pressure gaseous detector

D. Nygren proposed a new concept based on the columnar recombination in dense xenon gas which enables to sense the nuclear recoil direction relative to the TPC drift field [48]. The directionality information is obtained through a comparison, event-by-event, of the ionization signal and recombination signal that are produced prior to drifting the track

ionization. The optimum xenon density may be about ten bars, much higher than that of low pressure gas detectors, and large mass experiment can be performed.

Chapter 4

NEWAGE

NEWAGE (NEw general WIMP search with an Advanced Gaseous tracker Experiment) is one of the direction-sensitive direct dark matter search experiments. As mentioned in Section 2.4.3, directional information is certainly a strong evidence of the discovery of the dark matter. NEWAGE adopts a three dimensional gaseous tracking detector micro-Time Projection Chamber (μ-TPC) whose readout is a micro-Pixel Chamber (μ-PIC), one of the micro patterned gaseous detectors (MPGDs). The μ-PIC has two advantages; fine tracking and scalability. The finer pitch of μ-PIC (400 μm) than that of MWPC ($\sim$2 mm), realizes a higher direction sensitivity. The large size μ-PIC can be made at a low cost because it is made by print circuit board technology. CF_4 is selected for the target gas because the gas diffusion is small and fluorine has a relatively large SD cross section. Final goal of NEWAGE is to detect a strong evidence and to study the properties of the dark matter.

Previous measurements were performed in Kamioka with NEWAGE-0.3b' detector which improved the direction-sensitive limit of spin-dependent WIMP-proton cross section down to 557pb for 200GeV [61]. In that experiment, the gas pressure was set to 0.1 atm, the energy threshold was 50 keV with an angular resolution of 40° and an data acquisition protocol (DAQ-mode5) was used. In this chapter, details of NEWAGE-0.3b' detector are described. The structure of the detector is described in Section 4.1, and the data aquisition system is explained in Section 4.2. The simulator is written in Section 4.3, and the typical performances are described in Section 4.4.

4.1 NEWAGE-0.3b' detector

NEWAGE-0.3b' consists of a micro time projection chamber (μ-TPC), its electronics system, and the gas circulation system (Figure 4.1) and is set in an underground laboratory at Kamioka Observatory, Gihu, Japan.

A schematic view of the μ-TPC and the internal structure are shown in Figure 4.2 and Figure 4.3, respectively. μ-TPC consists of a two-dimensional imaging device "micro pixel chamber (μ-PIC)" [65], a gas electron multiplier (GEM) [66], and a detection volume (30 × 30 × 41 cm^3) filled with CF_4 gas at 0.1 atm. x, y and z axis are defined in Figure 4.2, and the unit is cm in this thesis unless otherwise mentioned.

A μ-PIC is a variation of the micro-patterned gaseous detectors (MPGDs) and is manufactured using printed circuit board (PCB) technology. PCB technology realizes an
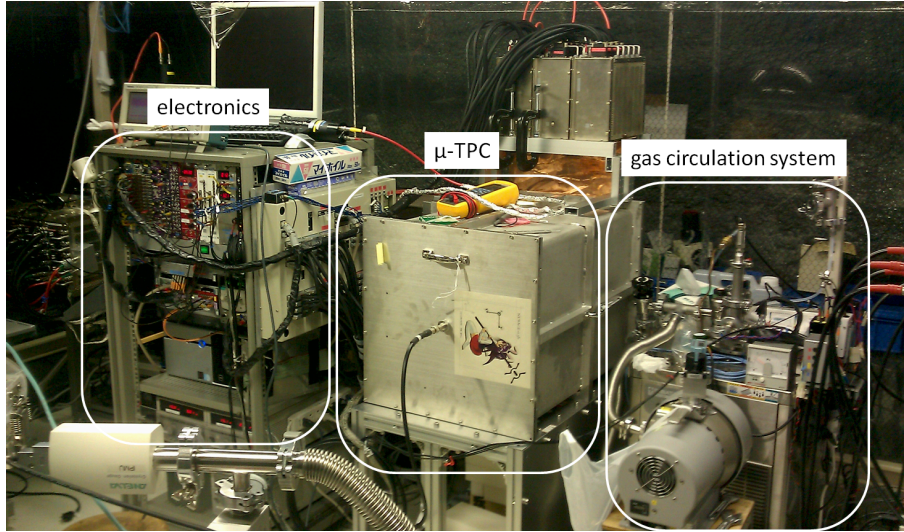
Figure 4.1: Outer view of the NEWAGE-0.3b' system in Kamioka Underground Laboratory. This system consists of the μ-TPC, the gas circulation system and the electronics(DAQ).
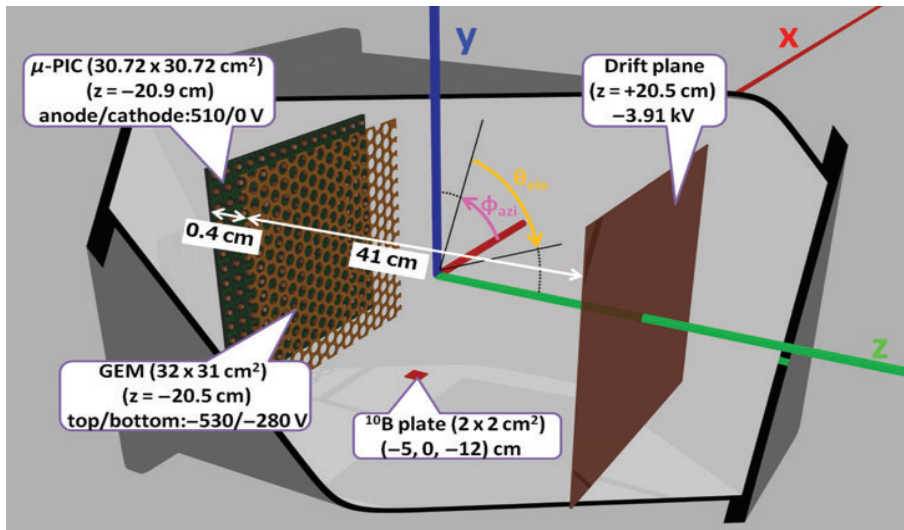
Figure 4.2: Schematic view of the μ-TPC. μ-TPC consists of a drift cage, a μ-PIC and a GEM. The detection volume is $30.72 \times 30.72 \times 41 \mathrm{cm}^3$.
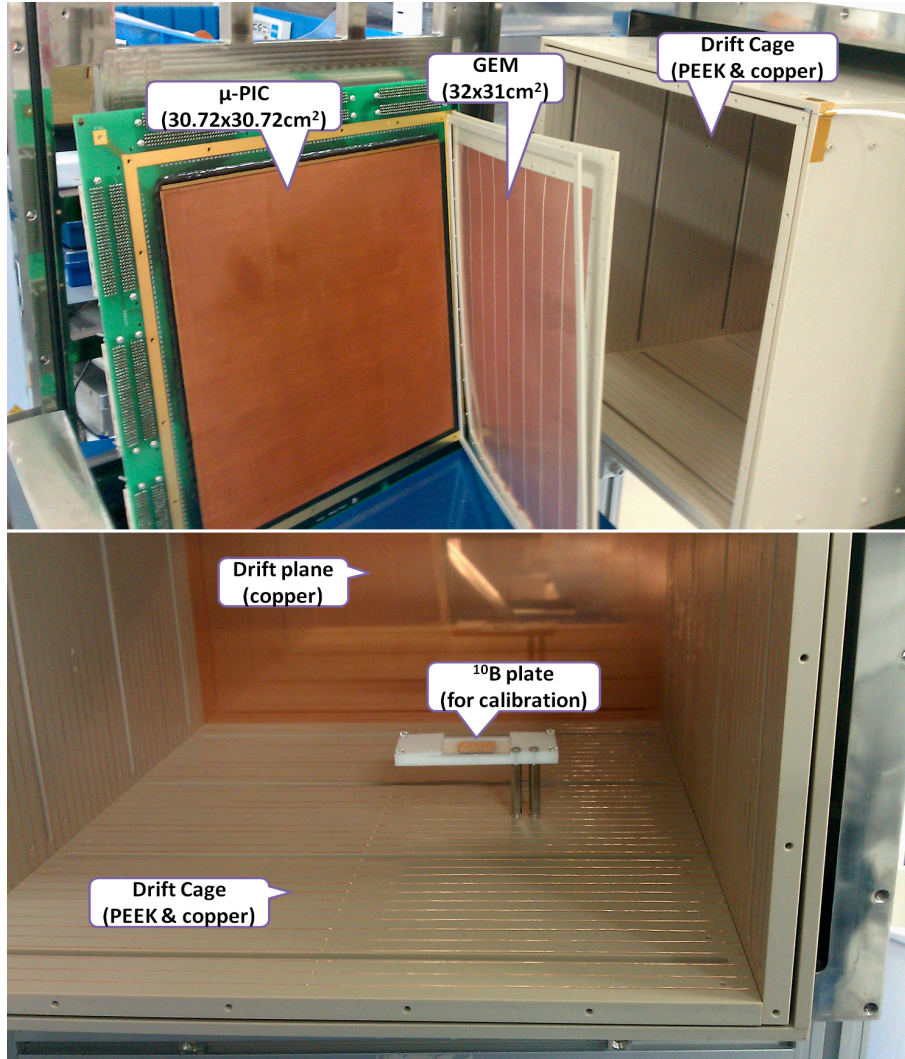
Figure 4.3: The μ-PIC and the GEM during their installation (upper) and inner structure of μ-TPC including the ^{10}B-evapolated glass plate (lower).

economical large-size detector production, which is one of the most important requirements for the fabrication of a dark matter detector. The effective area of the μ-PIC for the NEWAGE-0.3b' is 30.72×30.72 cm^2, and it has $768 + 768$ orthogonally-formed strips with a pitch of 400 μm. Anode electrodes with a diameter of 70 μm are formed on the strips in a circular ring cathode electrodes of 260 μm in diameter. The photographs and schematic the structure of the μ-PIC are shown in Figure 4.4. Positive bias applied to the anode electrode and gas amplification occurs around the anode electrodes and the same amount of negative and positive charge is read from the anode and cathode electrodes, respectively. The Charge from the anode and cathode electrodes are read through the strips.

The GEM is placed 4 mm above the μ-PIC as a sub-amplifier to ensure the gas gain. The effective area of the GEM (31×32 cm^2) covers the entire surface of the μ-PIC. The GEM area is segmented into 8 sub-areas to reduce discharge damages. The GEM is made

of a 100 μm thick liquid crystal polymer, the hole size and pitch are 70 μm and 140 μm, respectively.

The drift length is 41 cm, which was determined by the optimization between the target-increase advantage and the angular-resolution deterioration with a longer drift length. Electric field is formed by a drift plane and 1 cm-spaced wires on the side walls made of polyetheretherketone (PEEK). Typical voltages applied for the μ-PIC, the GEM and the drift plane are listed in Table 4.1, where a stable operation with a combined (μ-PIC $\times$ GEM) gas gain of 1500 was obtained. A glass plate with a thin layer of ^{10}B is installed at the position of $(-5, -12, 0)$ for the energy calibration. The size of the ^{10}B layer is 2×2 cm and the designed thickness is 0.6 μm. The μ-TPC is placed on a 2.5 cm thick stainless-steel vacuum vessel filled with CF_4 gas at 0.1 atm. As mentioned in Section (1), CF_4 gas is suitable for a direction-sensitive spin dependent dark matter search.
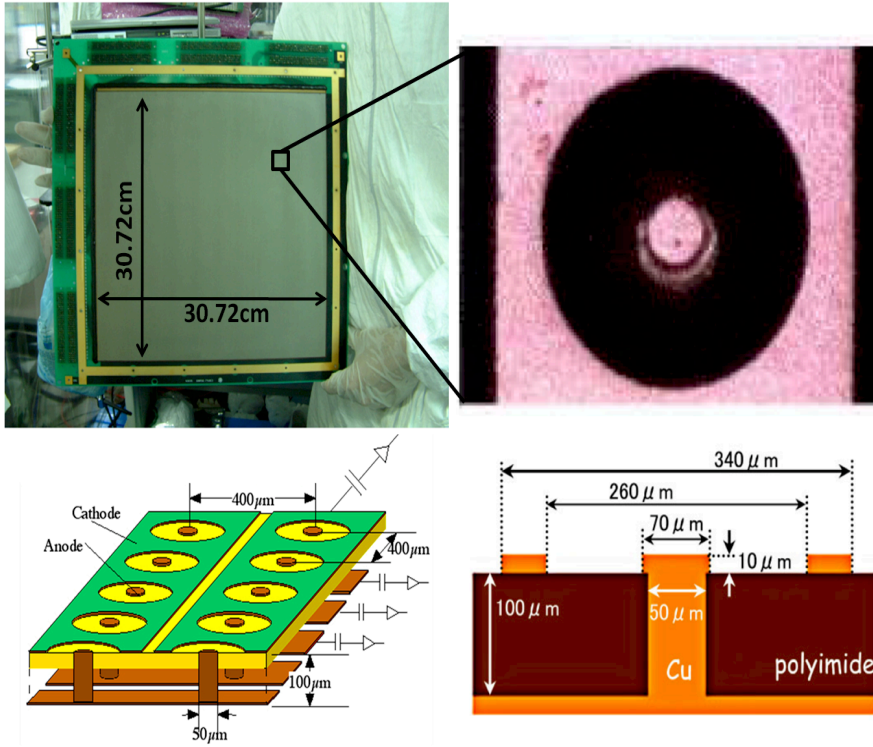

Figure 4.4: The photograph of the μ-PIC (left top) and the enlarged photograph by microscope (right top). The schematic view (left bottom) and the cross-section view of the μ-PIC structure (right bottom).

A gas circulation system with cooled charcoal was developed for NEWAGE-0.3b'. The schematic drawing is shown in Figure 4.5. The aims of this system are to reduce radon, which is a serious background source for dark matter searches, and to keep the gas quality (gas gain and drift velocity) during long time use for more than one month. The gas in the vessel passes through the charcoal, where 100 g of charcoal (the product name is TSURUMICOAL 2GS) absorb radon and impurities as well. The pump (XDS5 Scroll Pump (EDWARDS)) is an oil-free pump, and works with a low pressure gas at

Table 4.1: Supplied voltages for μ-PIC, GEM-top, GEM-bottom, and drift plane.

Device	Voltage	Current
μ-PIC	510 V	~ 4 nA
GEM-top	-530 V	< 1 μA
GEM-bottom	-280 V	< 1 μA
Drift plane	-3.76 kV	19.5 μA

0.1 atm. A needle-type valve was used to control the flow rate at $500 \sim 1000$ ml/min. A stable cooling at 230 K was realized by controlling a heater, while the cooler(CT-910 Cool Man Trap (SIBATA)) was always operated at its maximum cooling power.
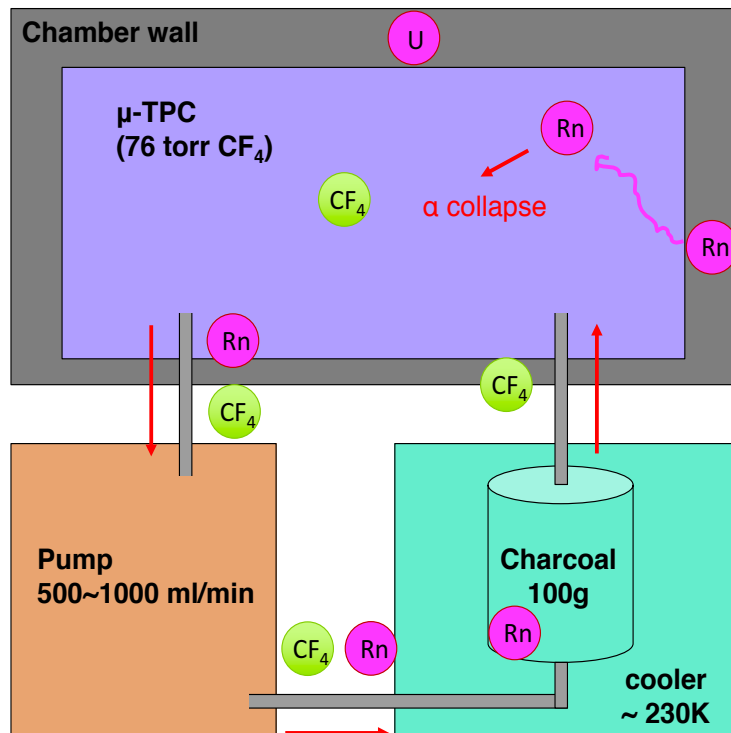
Figure 4.5: The schematic image of the gas circulation system for lowering radon backgrounds and keeping the gas quality.

4.2   Data acquisition system

A data acquisition (DAQ) system dedicated to the μ-PIC readout is used for the NEWAGE-0.3b' [67]. The schematic structure of the DAQ is shown in Figure 4.6.

The system records two types of data : "charge" by the flash-ADC(FADC) and "track" by the memory board. The DAQ has two types of trigger modes. One is the "self-trigger mode", where the TPC analog signals from 768 anode strips are grouped down to 16
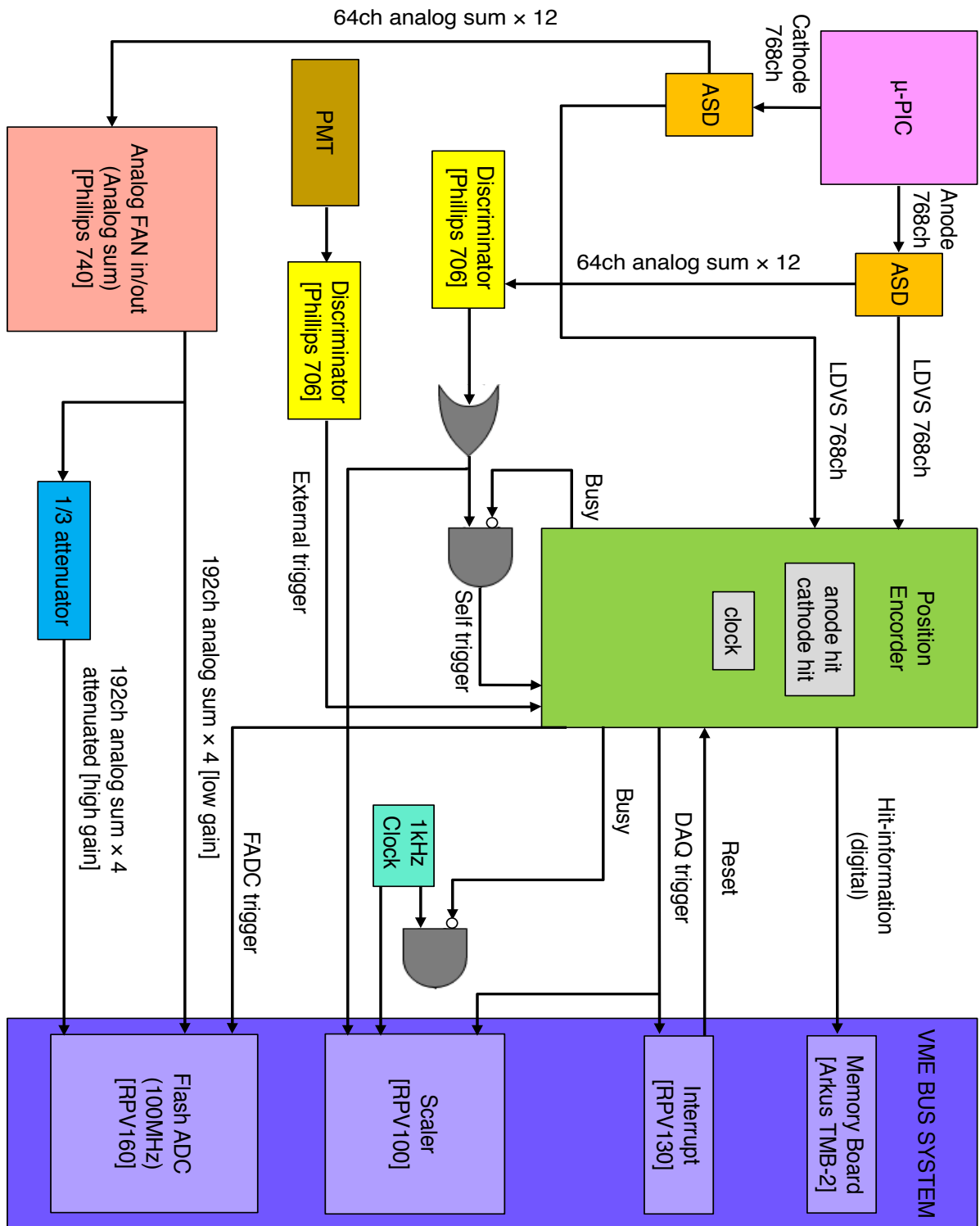
Figure 4.6: Data acquisition system (DAQ) of NEWAGE-0.3b' detector.

channels and any one of their hits is used as the trigger. In this trigger mode, the absolute z position is not measured, but only the relative position is measured. The self-trigger mode is used otherwise mentioned in this thesis. The other is "external-trigger mode", for a measurement using a ^{252}Cf source. The signal of a prompt gamma ray or a neutron from ^{252}Cf detected by a plastic scintillator set nearby the source is used as a trigger. In this mode, the absolute z position of the tracks are measured. The drift velocity and the angular resolutions are measured with the external-trigger mode. Two types of DAQ-mode for "track" data with a different measured parameters as listed in Table 4.2 were used for this work. DAQ-mode5 records the addresses and time-over-threshold (TOT) of all strips with a hit in each event. The TOT is the time between rising and falling edges crossing the threshold, which roughly corresponds to the deposited energy on the individual strips. as shown in Figure 4.7.

Table 4.2: The list of the DAQ mode.

DAQ-mode	mode1	mode5
x-y online-coincidence	required	not required
strip address to record at each clock	$X_{\min}, X_{\max}, Y_{\min}, Y_{\max}$	all
time over threshold (TOT)	not take	take
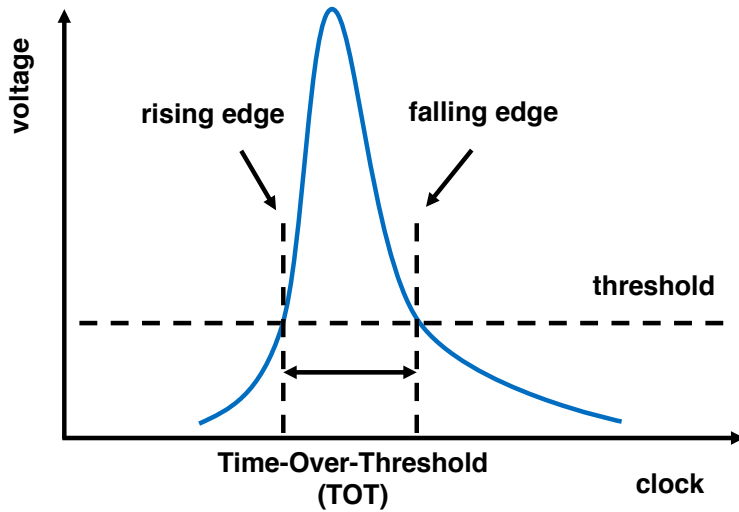
Figure 4.7: The schematic image of time-over-threshold (TOT). Blue line shows the waveform of a strip.

DAQ-mode5 with self-trigger mode is used for the dark matter measurements and calibrations unless otherwise mentioned. DAQ-mode1 records the data reduced in size by taking x-y coincidence and limiting the number of output addressed for the "track" information. The dead time of DAQ-mode1 was thus shorter than that of DAQ-mode5 and DAQ-mode1 is used for the external-trigger mode. For "charge" information, analog signal of 768 cathodes are amplified and grouped down to 8 channels, then these waveforms are recorded by a 100 MHz FADC. Half of the channels (4 channels) is used for low

energy event, on the other hand the other half of the channels, which are attenuated to 1/3 before recorded by FADC, are used for high energy event. The charge is calculated by summing up FADC-waveform area (FADC-value/FADC-bit [mV] × 10 [ns]) over the average revel each of clock is shown as purple part in Figure 4.8 when the signal exceeds the thereshold and dividing it by resistance value.
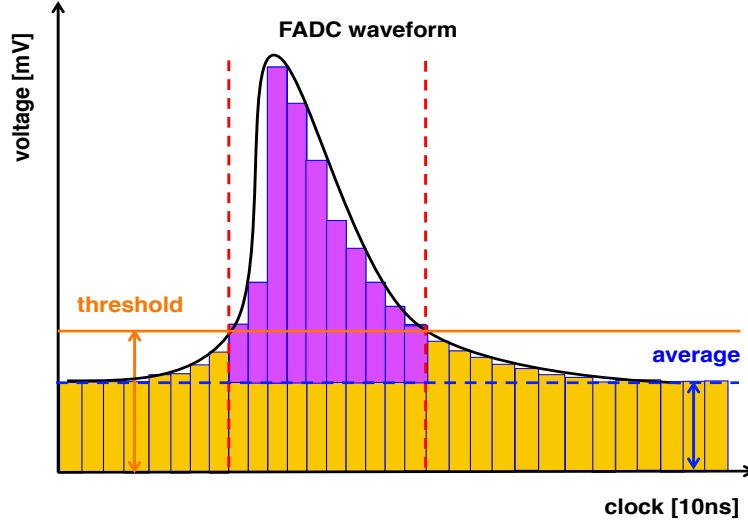
Figure 4.8: The typical FADC waveform (Black line).

4.3   Simulator

A Monte Carlo simulation was used to evaluate the detector performance. The full process, starting from the generation of incoming particles, followed by the interaction of the particles in the detector, the electron drift in the gas volume, the gas amplification nearby the detection plane, the amplification and the discrimination by the preamplifier, the data reduction in the FPGAs, and the data acquisition, was simulated. A simulation package named Geant4 [68], originally developed for high-energy physics experiments and now being used widely in related fields, was used for the generation, transportation and interaction of the incoming particles. Gamma-rays, electrons, neutrons, and α particles were generated inside and outside of the detector for the performance evaluation (Section 4.4). The version and physics lists used in the simulator are listed in Table 4.3.

The electron drift and the gas amplification parts were simulated mainly based on MAGBOLTZ package [49]. MAGBOLTZ is a package to simulate the transportation of electrons in gas. Electron clouds generated by a reaction in the detector volume are diffused during the drifting towards the detection plane. The electron diffusion in the CF_4 at 0.1 atm gas was simulated in our code. The diffusion size orthogonal($\sigma_{\text{transverse}}$) and parallel($\sigma_{\text{longitudial}}$) to the drift direction were 0.27 mm/$\sqrt{\text{cm}}$ and 0.19 mm/$\sqrt{\text{cm}}$, respectively. The electrons were diffused, amplified in the GEM holes and in the vicinities of the μ-PIC pixels, then detected by the μ-PIC detector. Positions and timings of the detected electrons were recorded. After the charge detection, the data acquisition system was simulated by our original code. The signal was amplified and discriminated by the

Table 4.3: The version and physics lists used for the simulation.

version	G4.9.2.p03
electromagnetic process	G4LowEnergyRayleigh G4LowEnergyPhotonElectric G4LowEnergyCompton G4LowEnergyGammaConversion G4LowEnergyIonisation G4LowEnergyBremsstrahlung G4eIonisation G4eBremsstrahlung G4eplusAnnihilation G4hLowEnergyIonisation G4EnergyLossTables G4hIonisation
hadronic process	G4LElastic G4LEProtonInelastic G4NeutronHPElastic G4NeutronHPElasticData G4NeutronHPInelastic G4NeutronHPCapture

preamplifires with the specifications listed in Table 4.4. Then the DAQ system was simulated and the "track" and "charge" information were recorded by the same format as the real data.

**Table 4.4:** The parameters of ASD used in the detector response included in the simulator.

parameter	value
rise time	6 ns
decay time	70 ns
preamp gain	0.898 V/pC
mainamp	× 7

4.4   Detector performance

The performance of NEWAGE-0.3b' detector was studied. The methods to measure these parameter and typical results are described in this section. Some of these performances were monitored during the dark matter runs.
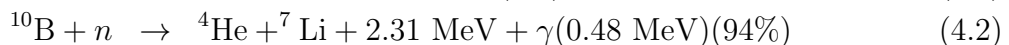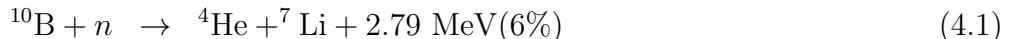
4.4.1 Drift Velocity

The electron drift velocity in the μ-TPC is needed to convert the arrival timing (clock) to the z position. We measured the nuclear recoil events in the μ-TPC using fast neutrons from ^{252}Cf source placed at $(0, 0, 47.5)$. In order to determine the starting time of drift, we used external-trigger mode with a plastic scintillator as the external trigger detecting gamma rays generated by fission of ^{252}Cf which simultaneously emits several fast neutrons. Because the trigger rate of external-trigger is very high, we used DAQ-mode1 which works with less dead time. Figure 4.9 shows one of the measured drift time distributions of nuclear recoils. The edge structure at 440 clock corresponds to the event occurred just below the drift plane. The drift velocity was calculated to be 9.3 cm/μs since electrons took 4.4 μs to drift 41 cm in this measurement.
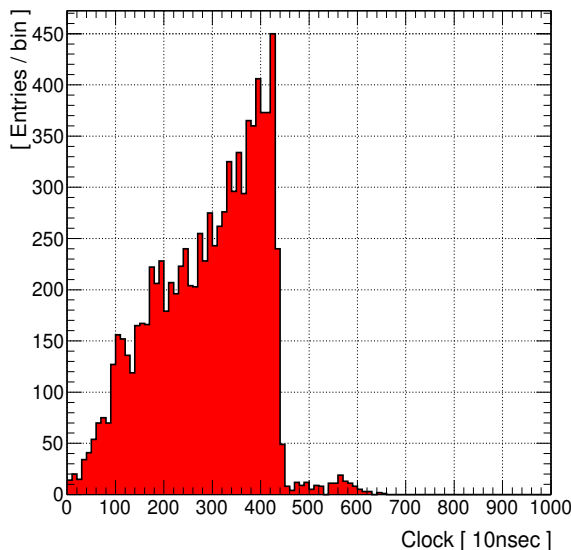

Figure 4.9: Drift time distribution of nuclear recoils in a drift velocity measurement

4.4.2 Energy calibration

Since our purpose is to detect the recoil nuclei by dark matter, we calibrated the energy scale of the μ-TPC using α particles instead of γ-rays and β-rays for the energy calibration. A glass plate on which ^{10}B is deposited with a thickness of 0.6 μm (designed value) in 2×2 cm area is placed at the position of $(-5, -12, 0)$ for the calibration (see Figure 4.2). By irradiating the ^{10}B plate with thermalized neutrons from ^{252}Cf surrounded by polyethylene, α particles are generated in the μ-TPC by the following reactions.

$$^{10}\text{B} + n \rightarrow {}^{4}\text{He} + {}^{7}\text{Li} + 2.79 \text{ MeV}(6\%) \tag{4.1}$$

$$^{10}\text{B} + n \rightarrow {}^{4}\text{He} + {}^{7}\text{Li} + 2.31 \text{ MeV} + \gamma(0.48 \text{ MeV})(94\%) \tag{4.2}$$

Since the cross section of reaction (4.2) is about 15 times larger than that of (4.1), neutron capture reaction of ^{10}B emits prompt γ-rays with 478 keV in most cases, and the

54
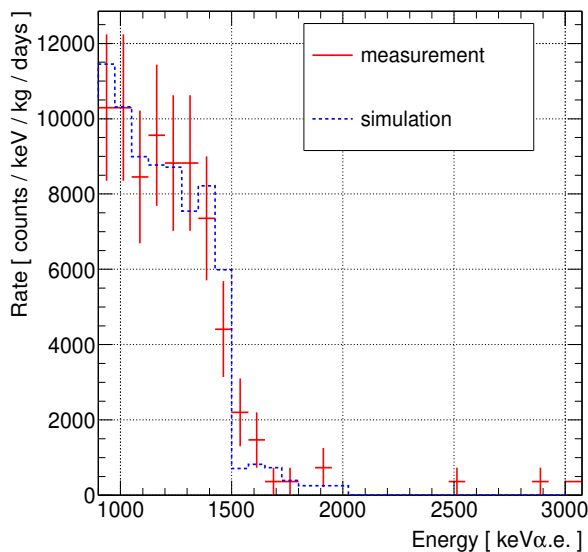
Figure 4.10: A result of an energy calibration using α particles from ${}^{10}B(n, \alpha){}^{7}$Li. Blue line is simulated energy spectrum and red points are measured one.

^{7}Li nuclei and α particle share $2.22(= 2.7 - 0.478)$ MeV, thus the generated α particle has 1.5 MeV of kinetic energy. Because the thickness of the deposited ^{10}B is not negligible compared to the range of α-rays in boron, the 1.5 MeV α particles make the shape of an edge rather than a peak. Figure 4.10 shows the result of the energy calibration. By comparing the simulation (blue line) and measurement (red histograms with error bars), we determined the energy scale.

In order to check the linearity, we checked the energy scale of ~ 6 MeV in addition to the ^{10}B calibration. The radon decay events in the TPC gas make peaks around 6MeV. Figure 4.11 shows the measured energy spectrum of α particles due to the radon progeny. There are two types of radon as ^{220}Rn and ^{222}Rn. The energy of α particles from ^{220}Rn and its progeny are 6.288 MeV, 6.779 MeV, 6.051 MeV (35.94%) and 8.785 MeV (64.06%), and that of ^{222}Rn are 5.490 MeV, 6.003 MeV (99.98%) and 7.687 MeV (99.98%). Therefore, both radon makes peaks at ~ 6 MeV. Since the fraction of the ^{220}Rn and ^{220}Rn is not known, both cases were examined and the differences were treated as the systematic error. The linearity up to 6 MeV was thus confirmed within the systematic error as shown in Figure 4.12.

Though the energy calibration in the lower energy region is important, direct measurement with a gas gain of 1500 is difficult. A linearity check with a small-sized detector operated at higher gas gain with an ^{55}Fe source was performed and we rely on this measurement for the low energy linearity [63].
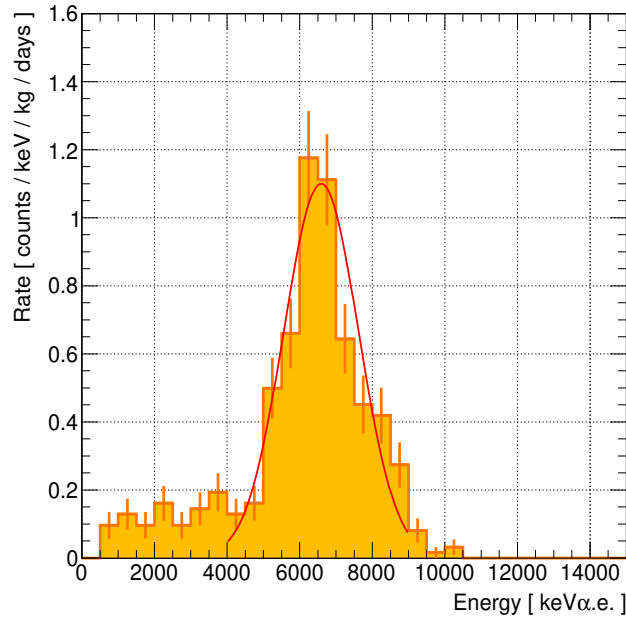
Figure 4.11: The measured energy spectrum of α particles due to the radon progeny (orange histogram). Red line is the fitted line in case of ^{220}Rn.
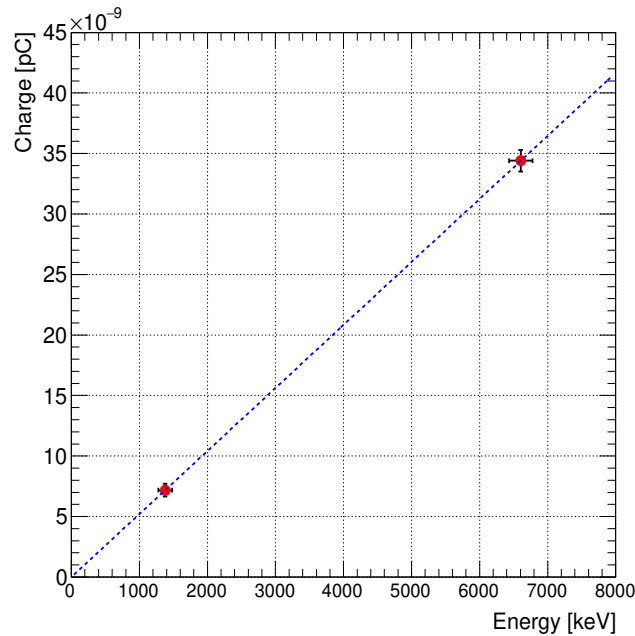

Figure 4.12: The relation of energy and charge. Red point around 1.5MeV is determined from ^{10}B calibration, and point around 6MeV is obtained from radon fitting. The error bar is the systematic error due to the difference of ^{220}Rn and ^{222}Rn.

4.4.3 Energy resolution

The energy resolution estimated by fitting energy spectrum of the radon peak and FADC waveform. The energy resolution obtained from the width of the radon peak was $12 \pm 1\%$. This resolution, σ_{uni}, is due to the position dependence of the gas gain and the attachment of electrons during the drift. The electric noise component in the energy resolution, σ_{noise}, was evaluated with the FADC data. The off-timing waveforms were processed by the same manner as the on-timing data. σ_{noise} has energy dependence because the time-window for the charge calculation has energy dependence, thus the σ_{noise} values were evaluated for the energies relevant for the dark matter signals. Obtained energy resolution due to electronic noise was $\sigma_{\mathrm{noise}} = 1.4$ keV for 50 keV. The energy dependence of σ_{noise} and total energy resolution σ_{total} are shown in Figure 4.13. σ_{total} is defined by Equation (4.3).

$$\sigma_{\mathrm{total}} = \sqrt{\sigma_{\mathrm{uni}}^2 + \sigma_{\mathrm{noise}}^2} \qquad (4.3)$$
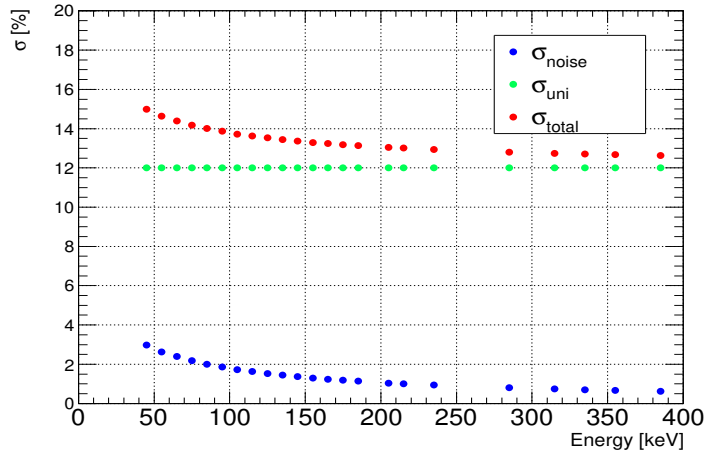
Figure 4.13: Blue, green and red point are estimated noise, uniform and total energy resolution, respectively.

4.4.4 Event Selection

The event selection criteria was almost the same as the one used in the previous measurement [61]. A fiducial volume of $28 \times 24 \times 41$ cm^3 was selected from the detection volume of $30.72 \times 30.72 \times 41$ cm^3 and we required that the whole track of the particle was in this fiducial volume. This cut mainly rejects protons and electrons from the wall of the detection volume and the ^{10}B plate. The gamma-ray and the alpha-ray background are cut by the following criteria. Because the energy deposition per unit distance of an electron is much smaller than that of a nucleus, tracks of electron events should be long and non-continuous compared to tracks of nuclear events. The track length and the energy deposition are quantified by two parameters: "length" and "TOT-sum". "length" is calculated as follows. In the x-z and y-z planes, rising points are fitted with straight lines. Here, the rising points have information about the track shape, while the time durations (TOTs) correspond to the energy deposition. Then, the range of rising points along the fitted line is calculated on each plane and the "length" in the 3D space is calculated by quadrature. Besides, because the drift length of the alpha-ray background from radioactive impurities contaminated the μ-PIC is short, gas diffusion is small, and the track shape is close to a straight line. In order to discriminate this alpha-ray background by using track shape, "roundness" is defined by Eq. (4.4) as the extent to which the shape of the rise points.

$$
\begin{aligned}
\text{roundness}_\text{x} &= \frac{\sum^{N_x}(z_\text{risex} - a_x x - b_x)^2}{N_x}, \quad \text{roundness}_\text{y} = \frac{\sum^{N_y}(z_\text{risey} - a_y y - b_y)^2}{N_y} \\
\text{roundness} &= \min(\text{roundness}_\text{x}, \text{roundness}_\text{y})
\end{aligned}
\tag{4.4}
$$

where N_x and N_y are the number of hits on the x and y strips, respectively. z_risex and z_risey are the minimum z values, and (a_x, b_x) and (a_y, b_y) are the best-fit straight lines obtained by fitting (x, z_risex) and (y, z_risey), respectively.

In this work , a energy-dependence was added to the TOT-sum cut in order to improve the rejection of the gamma-ray background. We checked the energy dependence of the track length, TOT-sum, and roundness for nuclear events by ^{252}Cf and gamma-ray events by ^{137}Cs. The cut criteria are listed below and Figure 4.14 shows Length cut, TOT-sum cut and Roundness cut respectively.

- **Fiducial cut** : -14 cm $\leq$ X $\leq$ +14 cm, -10 cm $\leq$ Y $\leq$ +14 cm

- **Energy cut** : 50 keV $\leq$ Energy $\leq$ 400 keV

- **Length cut** : Length cm > 0.6 + 0.004 $\times$ E keV
  for the rejection of long events.

- **TOT-sum cut** : TOT-sum < 50 + 0.5 $\times$ E keV
  for the rejection of scratched events.

- **Roundness cut** : roundness < 0.04
 for the rejection of the events remained in ^{137}Cs-run.

The detection efficiency after these cuts applied for the nuclear events and the rejection power for gamma-ray events were measured. We evaluated the efficiency by dividing the
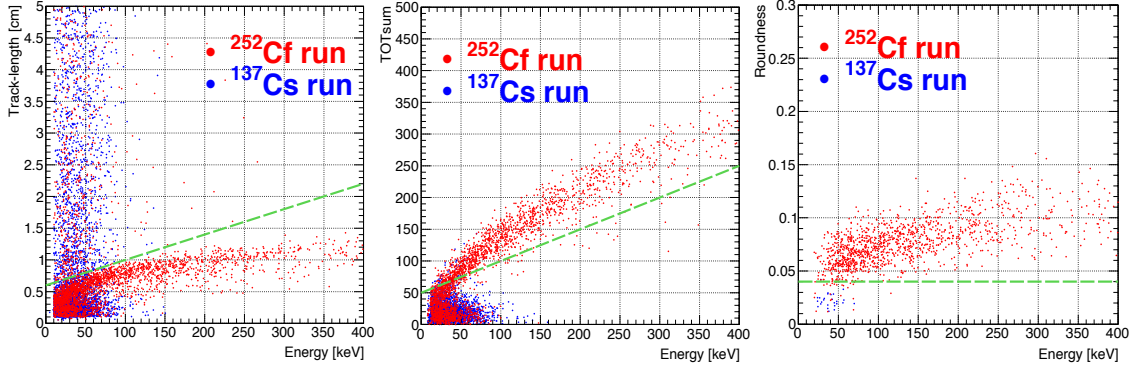
Figure 4.14: Energy dependence of the track length(Left), TOT-sum after the length cut(Center) and roundness after the length cut and TOT-sum cut(Right). Red and blue points are measured with ^{252}Cf and ^{137}Cs, respectively.

measured energy spectrum after all cuts by the simulated one. An ideal simulation results, not including the detector responses was used as the denominator. In order to cancel the position dependence and measure an overall response of the detector, an averaged spectrum of 6 measurements by placing a ^{252}Cf to 6 places; $(25.5, 0, 0)$, $(-25.5, 0, 0)$, $(0, 25.5, 0)$, $(0, -25.5, 0)$, $(0, 0, 47.5)$ and $(0, 0, -47.5)$ was used. The detection efficiency fluctuates depending on the Elapsed time from gas change date and typical detection efficiency of the nuclear recoil events is shown in Figure 4.15 here. We obtained the detection efficiency of nuclear events as 30% at 50 keV. The detection efficiency of electron events, or the gamma-ray rejection power, was evaluated by irradiating the detector with gamma-rays from a ^{137}Cs source and comparing the data with the simulation results. The detection efficiency for a given energy bin was calculated by dividing the measured event rate with the simulated event rate of the electron with that energy. Evaluated detection efficiency in the energy bin 50 - 100 keV was 2.5×10^{-5}. The energy dependence of the electron detection efficiency is shown in Figure 4.16.
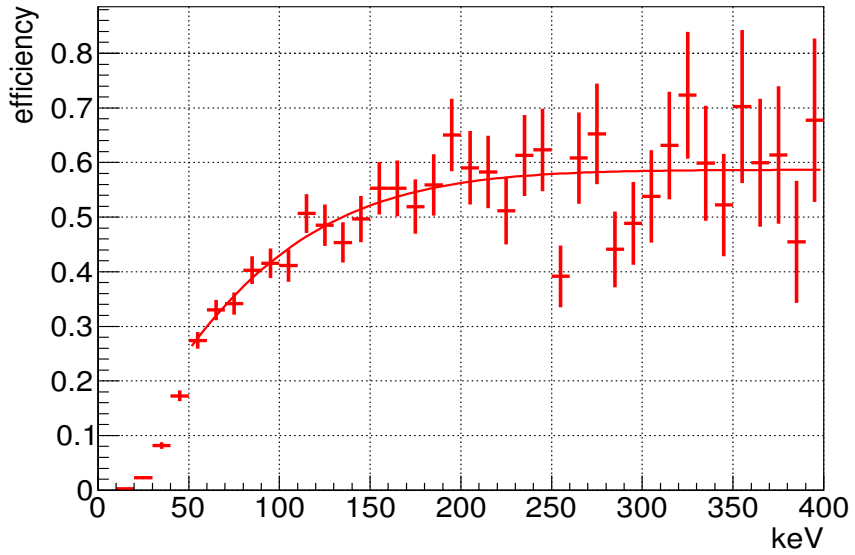
Figure 4.15: The detection efficiency of nuclear events.
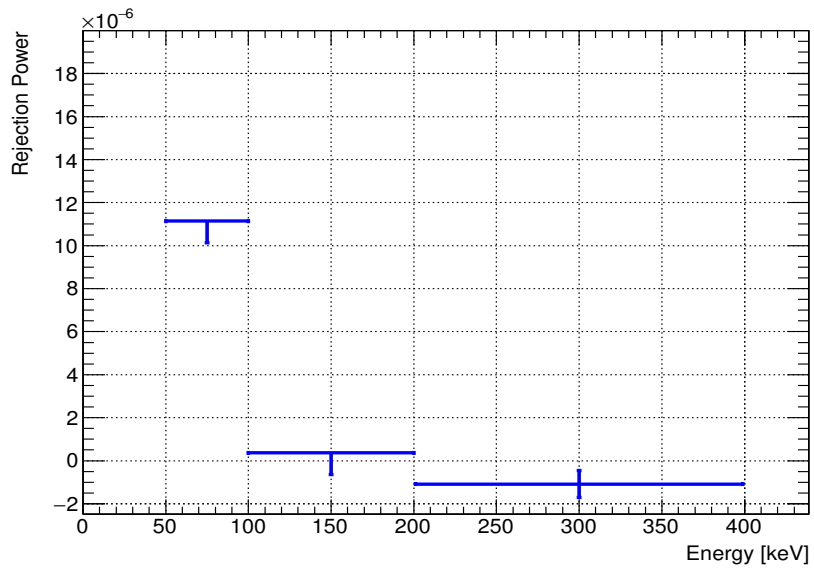
Figure 4.16: The detection efficiency of the electron event, or gamma-ray rejection power.

60

4.4.5   Angular resolution

The angular resolution of the nuclear tracks was measured using the fast neutrons from a ^{252}Cf source [69]. It is evaluated by the comparison of measured and simulated distributions of the recoil angle. The recoil angle is defined in Figure 4.17. In order to measure the actual scattering position, DAQ-mode1 with an external-trigger mode was used.
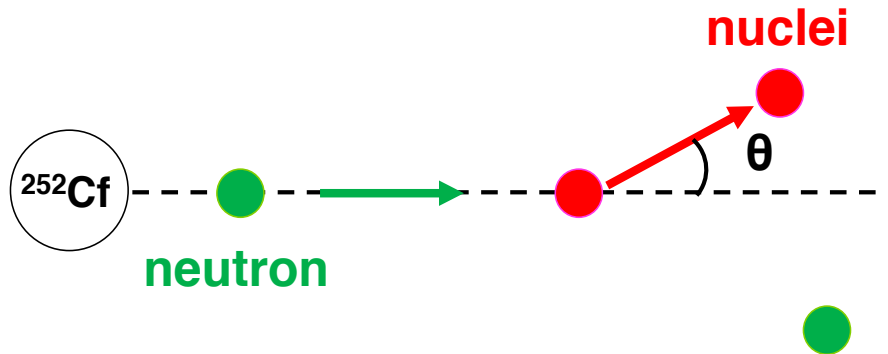

Figure 4.17: The schematic view of nuclear recoil. θ is the recoil angle.

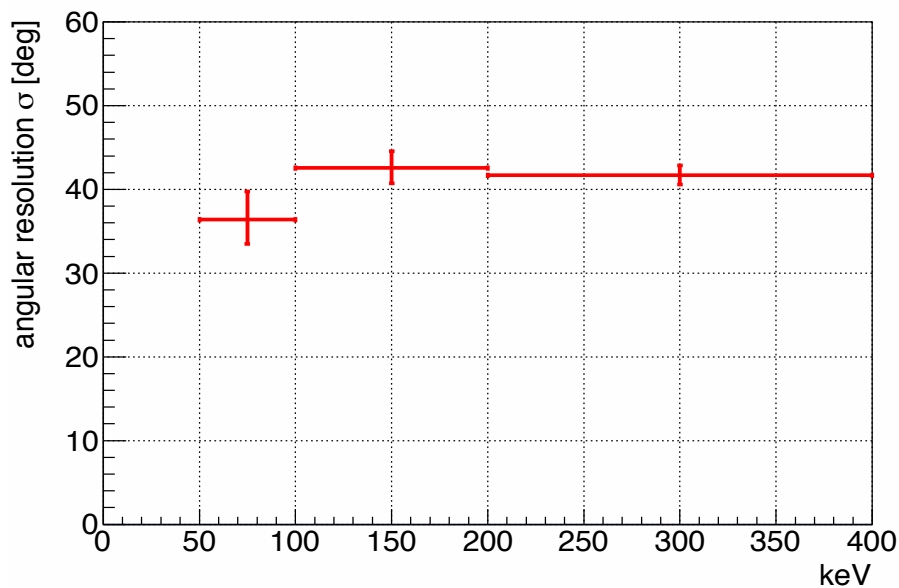The result of measured angular resolutions in each energy ranges is shown in Figure 4.18 [64].

Figure 4.18: Obtained angular resolution for each energy [64].

4.4.6 Direction dependent efficiency

[Direction-dependent efficiency was measured by using the DAQ-mode5. The detector was irradiated with neutrons from a ^{252}Cf source placed at $(25.5, 0, 0)$, $(-25.5, 0, 0)$, $(0, 25.5, 0)$, $(0, -25.5, 0)$, $(0, 0, 47.5)$ and $(0, 0, -47.5)$. We confirmed that we can generate isotropic recoil (standard deviation is 23%) with a weighted sum of these six measurements by Geant4 simulations. Figure 4.19 shows the measured distribution of the elevation angle θ_{ele} and the azimuth angle ϕ_{ele}(see detector coordinate shown in Figure 4.2). We can see that the efficiency is high around $(\theta_{\mathrm{ele}} = 0°, \phi_{\mathrm{azi}} = 0°)$ and $(0°, \pm 90°)$. Since $\phi_{\mathrm{azi}} = 0°$ and $\phi_{\mathrm{azi}} = \pm 90°$ represent the direction of the anode or cathode strips, it is seen that the recoil direction tends to be detected as that along the anode or cathode strips. Also, there are higher points along the diagonal lines from the direction of the anode and the cathode strips. This is because the current tracking algorithm tends to measure the diffused tracks in such directions. Measured direction-dependent efficiency is used for weighting the expected direction distribution of recoil nuclear track for the directional dark matter search analysis.
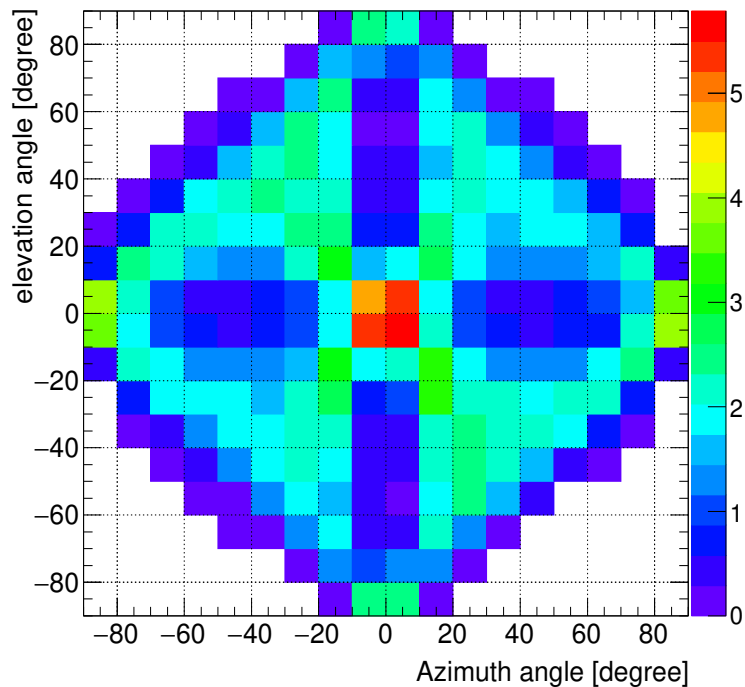
Figure 4.19: Direction-dependent efficiency in the 50 - 400 keV range measured with DAQ-mode5 and the self trigger. The vertical axis is the elevation angle and the horizontal axis is the azimuth angle. Color scale is normalized counts by the mean value.

4.4.7 Head-tail recognition

The head-tail recognition is sense-determination of the measured tracks. After the fundamental studies with prototype detectors [70, 71], head-tail recognition is applied for the NEWAGE dark matter analysis for the first time. NEWAGE-0.3b' detector was used as a 3D-axial detector and will be upgraded to a 3D-vector detector with this work. Figure 4.20 shows the calculated energy deposition of a ^{19}F nucleus of 500 keV in CF$_4$ gas at 0.1 atm as a function of its track trajectory using the SRIM simulation [52]. The point on the left-hand side is the initial point and that on the right-hand side is the final point of the track. The initial position and final position of the nucleus corresponds to 0 mm and around 7 mm, respectively. The energy deposition is the largest at the initial point and decreases as the nucleus passes through the gas. In this analysis, we used the position of the hit (anode and cathode) strip, TOT and FADC-sum waveforms as a measurable of the nuclear tracks.
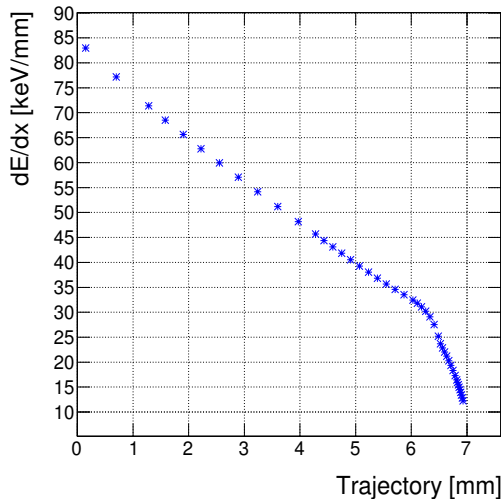
Figure 4.20: Energy deposition (dE/dx) of 500 keV F nucleus in CF4 gas at 0.1 atm as a function of the nucleus position along the track path obtained using SRIM simulation.

We irradiated the detector with the fast neutrons from a ^{252}Cf source placed at $(25.5, 0, 0)$, $(-25.5, 0, 0)$, $(0, 25.5, 0)$, $(0, -25.5, 0)$, $(0, 0, 47.5)$ and $(0, 0, -47.5)$. The histograms shown in Figure 4.21 are the measured TOTs of a nuclear track with a ^{252}Cf source placed at $(-25.5, 0, 0)$. The energy is 200 keV and the track length is 0.96 cm. The direction of the event is clearly detected for this event since the TOT distribution of the anode strips show larger charge detection in the smaller X, or the beginning of the track. The TOT distribution of the cathode strips is more symmetric as expected. Although the original shape of the energy deposition curve is smeared by the electron diffusion during the drift, it is expected that the asymmetries of anode and cathode TOT distributions can be used to determine the head-tail recognition in the plane parallel to the μ-PIC (X−Y plane). We defined the skewness (X) and skewness (Y) as equation (4.5) and (4.6) for the head-tail recognition parameters for the X and Y directions, respectively.
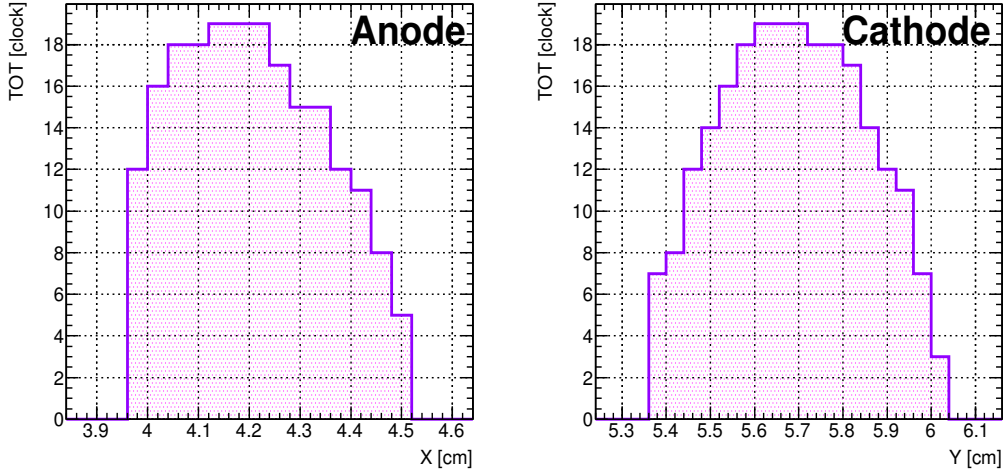
Figure 4.21: Measured TOT per strip of a nuclear track with a ^{252}Cf source placed at ($-$25.5,0,0). Left and right histogram correspond to Anode and Cathode, respectively.

$$\text{skewness (X)} = \frac{S_{X3}}{S_{X2}^{3/2}} \tag{4.5}$$

$$S_{X3} = \frac{\sum_i^{N_X} TOT_{(X_i)} * (X_i - <X>)^3}{N_X},$$

$$S_{X2} = \frac{\sum_i^{N_X} TOT_{(X_i)} * (X_i - <X>)^2}{N_X},$$

$$\text{skewness (Y)} = \frac{S_{Y3}}{S_{Y2}^{3/2}} \tag{4.6}$$

$$S_{Y3} = \frac{\sum_i^{N_Y} TOT_{(Y_i)} * (Y_i - <Y>)^3}{N_Y},$$

$$S_{Y2} = \frac{\sum_i^{N_Y} TOT_{(Y_i)} * (Y_i - <Y>)^2}{N_Y},$$

where $X_i(Y_i)$ is the position of the hit strip, $TOT_{(X_i)}(TOT_{(Y_i)})$ is the value of TOT at $X_i(Y_i)$, and $N_X(N_Y)$ is the number of hit strips. Skewness is an asymmetric parameter in statistics. If a distribution is perfectly symmetric, the skewness parameter is zero. The distortion, represented by the sign and size of the skewness, was calculated for the obtained data. The measured skewness X and Y shown in Figure 4.22 and 4.23.
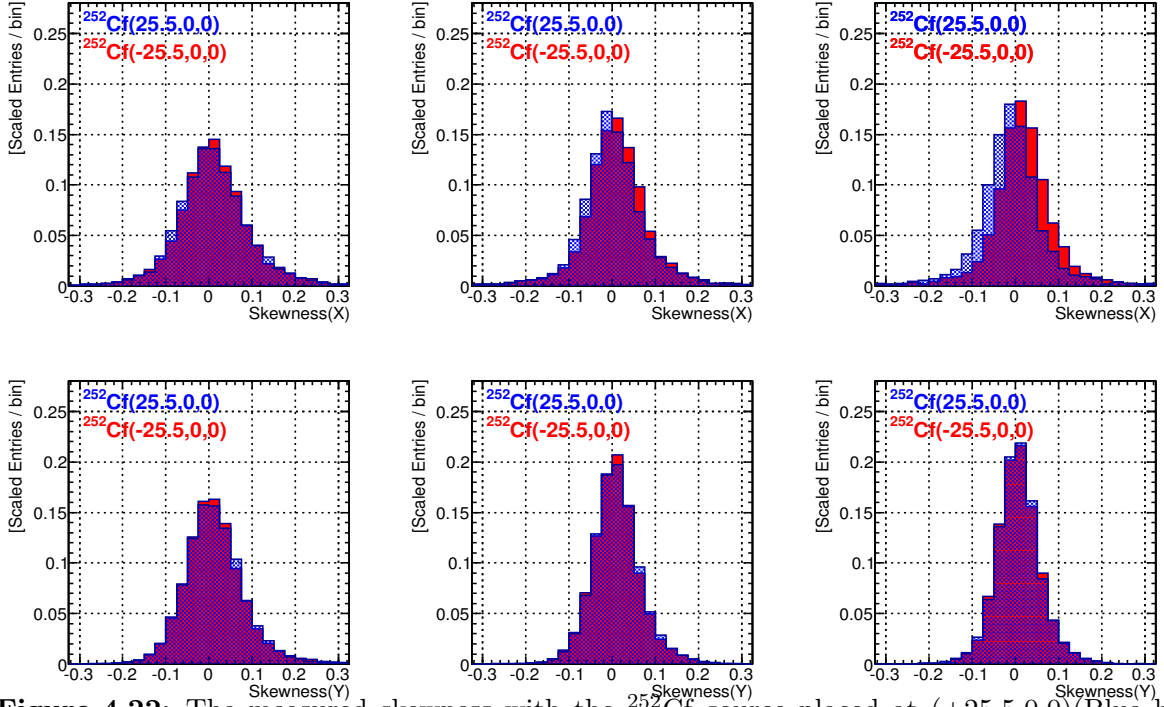
Figure 4.22: The measured skewness with the ^{252}Cf source placed at $(+25.5,0,0)$(Blue histogram) and $(-25.5,0,0)$(Red histogram). Left, middle and right panel correspond to 50-100 keV, 100-200 keV and 200-400 keV, respectively.
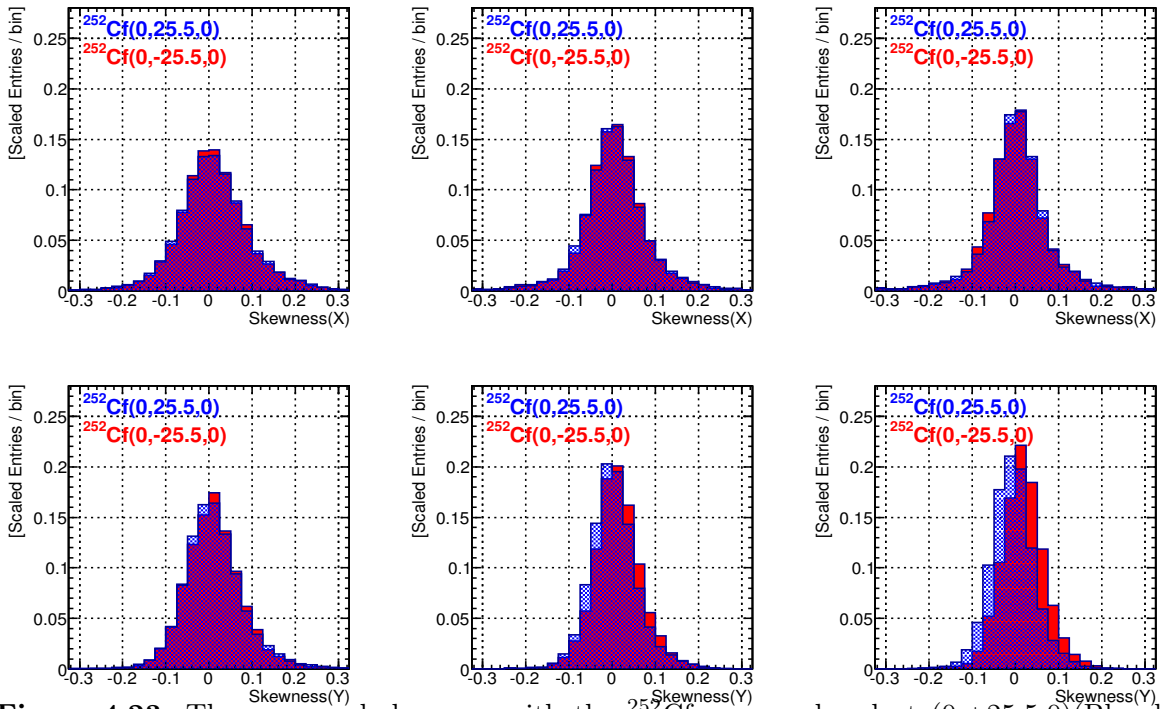
Figure 4.23: The measured skewness with the ^{252}Cf source placed at $(0,+25.5,0)$(Blue histogram) and $(0,-25.5,0)$(Red histogram). Left, middle and right panel correspond to 50-100 keV, 100-200 keV and 200-400 keV, respectively.
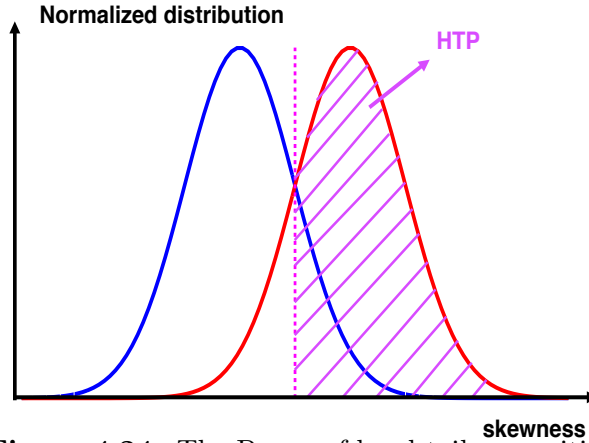
Figure 4.24: The Power of head-tail recognition

As shown in Figure 4.22 and 4.23, the distributions of skewness (X) and (Y) are hardly distinguishable with respect to the source position. The ϕ cut is defined as following,

- ϕ **cut** : $41° \leq$ Azimuth angle $\leq 54°$

In this study, HTP is defined as shown in Figure 4.24 for the energy range of $50-100$ keV, $100-200$ keV and $200-400$ keV. The power is fraction of events with a skewness larger than a set value. In the following discussions, this limits is always set to zero. In the example of the blue histogram or the irradiation from the opposite direction, the fraction below the limit is the HTP. The criteria (red dotted line) is the average of skewness (X)((Y)) for irradiation with the ^{252}Cf source placed at $(0,\pm25.5,0)((\pm25.5,0,0))$ The measured skewness distributions X and Y after the ϕ cut are shown in Figure 4.25 and 4.26.

The measured HTP by using skewness parameter is summarized in Table 4.5. From the results obtained, the HTP value to characterize the detector performance as the 3D-vector detector were determined. Determined HTP value are 50 % for 50-100 keV, 60 % for 100-200 keV and 75 % for 200-400 keV. Since the asymmetry in X and Y are large and some results are equivalent to 50%, it was determined that the head-tail analysis will not be applied for the energy range of 50-100 keV. In other words, the NEWAGE-0.3b' detector was used as a 3D-vector detector for the energy over 100 keV and as a 3D-axial detector for the energy 50-100 keV.

Table 4.5: The HTP for 50-100 keV, 100-200 keV, 200-400 keV.

energy range	+X HTP %	−X HTP %	+Y HTP %	−Y HTP %	average %
50-100 keV	48	64	57	60	57 ± 6
100-200 keV	58	64	67	65	64 ± 4
200-400 keV	66	83	80	74	76 ± 8
histogram	blue(Fig.4.25)	red(Fig.4.25)	blue(Fig.4.26)	red(Fig.4.26)	
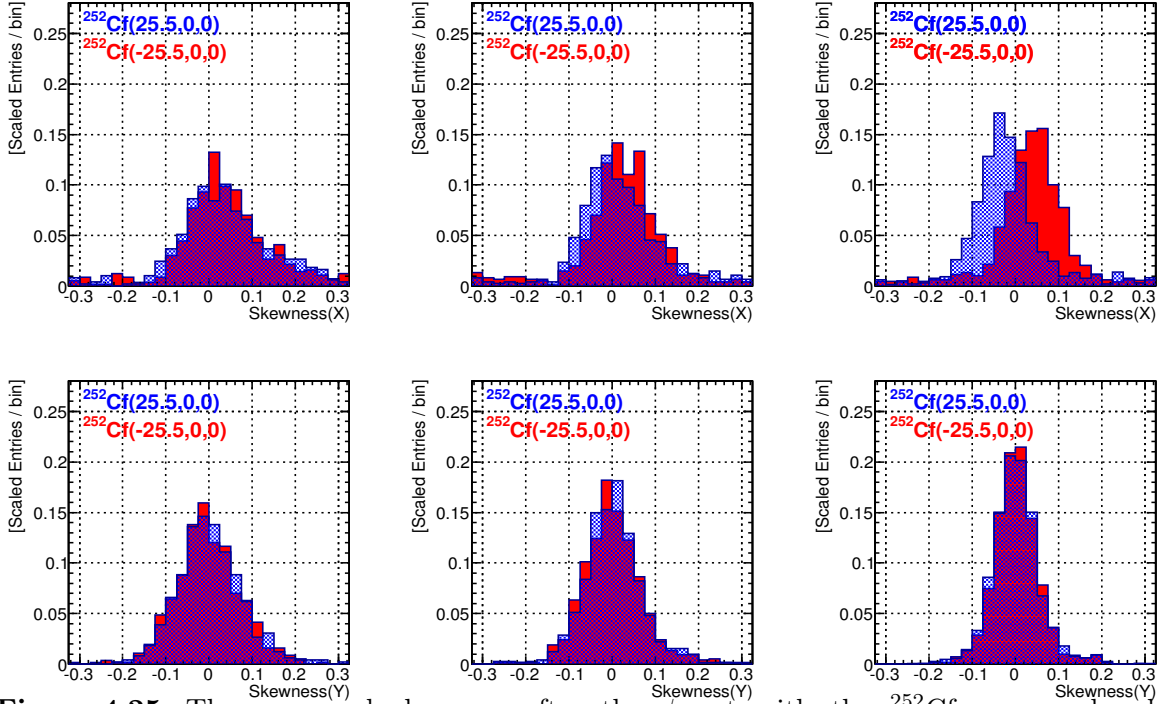
Figure 4.25: The measured skewness after the ϕ cut with the ^{252}Cf source placed at $(+25.5,0,0)$(Blue histogram) and $(-25.5,0,0)$(Red histogram). Left, middle and right panel correspond to 50-100 keV, 100-200 keV and 200-400 keV, respectively.
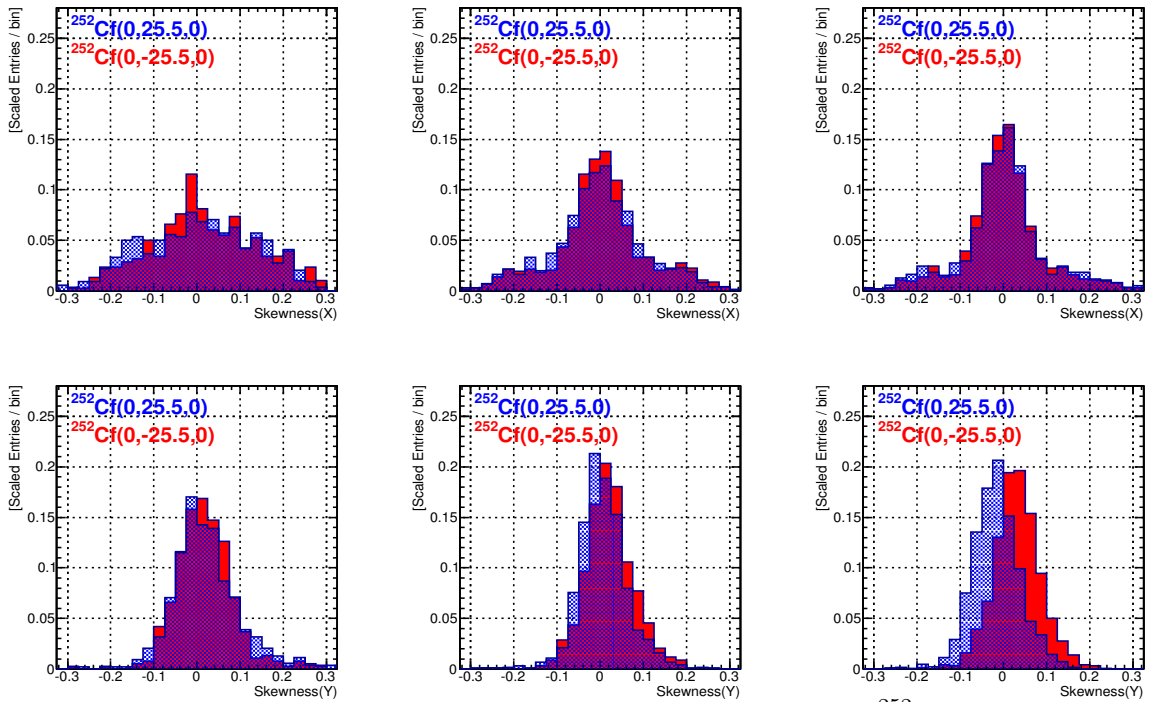
Figure 4.26: The measured skewness after the ϕ cut with the ^{252}Cf source placed at $(0,+25.5,0)$(Blue histogram) and $(0,-25.5,0)$(Red histogram). Left, middle and right panel correspond to 50-100 keV, 100-200 keV and 200-400 keV, respectively.

The nuclear efficiency and directional efficiency described in Section 4.4.4 and 4.4.6 respectively needs to be upgraded for a 3D-vector analysis due to the ϕ cut. Figure 4.27 shows the absolute detection efficiency (left) and direction-sensitive efficiency (right) after the ϕ cut. These efficiencies are the efficiency of the NEWAGE-0.3b' as a 3D-vector detector.
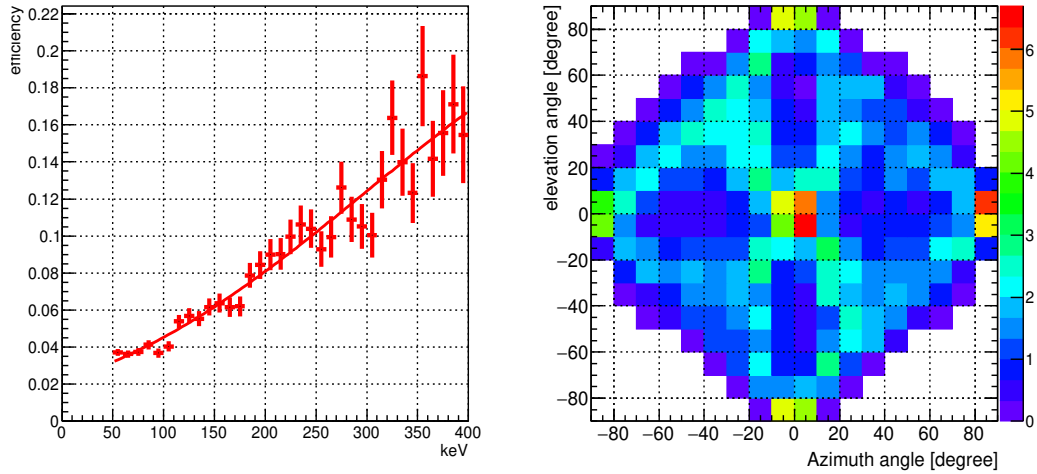
Figure 4.27: The nuclear efficiency (Left) and directional efficiency map (Right) applied ϕ cut.

Chapter 5

Direction-sensitive dark matter search

5.1 Measurement

A dark matter search experiment was performed in Kamioka underground laboratory from Jul. 2013 to Aug. 2017. The data accumulated during these measurements are listed in Table 5.1. The "main" run number is increased when the hardware is modified and the "sub" run number is increased when the chamber gas was changed.

Table 5.1: Measured date and live time for Run14 − Run18

| Run number	Measured date	Live time [days]	direction	flow [ml/min]
Run14-1	2013/7/17 - 2013/9/16	17.10	S30E	500
Run14-2	2013/10/17 - 2013/11/14	14.52	S30E	500
Run14-3	2014/01/29 - 2014/3/12	25.34	S30E	500
Run15-1	2015/3/30 - 2015/8/17	N/A	S30E	700
Run15-2	2015/8/17 - 2015/10/27	N/A	S30E	700
Run15-3	2015/11/6 - 2016/1/14	N/A	S30E	700
Run16-1	2016/1/14 - 2016/3/10	42.28	S30E	1000
Run16-2	2016/3/25 - 2016/6/28	69.94	S30E	1000
Run17-1	2016/6/28 - 2016/8/24	26.16	S30E	500
Run18-1	2016/8/24 - 2016/8/27	N/A	S74E	700
Run18-2	2016/9/1 - 2016/10/19	41.43	S74E	700
Run18-3	2016/10/20 - 2017/1/19	66.86	S74E	700
Run18-4	2017/1/26 - 2017/4/21	49.51	S74E	700
Run18-5	2017/4/27 - 2017/8/8	81.71	S74E	700
Total	2013/7/17 - 2017/8/8	434.85		

Initial results used the data of Run14-1 and Run14-2 with an exposure of 0.327 kg·days was previously reported [61]. Since then, additional data of 403.23 live-days were accumulated until Aug. 2017. In this study, a data set with a total live time of 434.85 days corresponding to an exposure of 4.505 kg·days is used. The statistics is about 14 times of the first results. The Z-coordinate of the Z axis of the detector was aligned to S30E for the first half and to S74E for the second half to cancel the potential systematics. The gas circulation rate was changed time-to-time as listed in the table. The data accumulated during Run15 and Run18-1 was not used for the analysis because the system suffered from electronic noise and DAQ system was out of condition in the corresponding runs, respectively.

5.2 Detector stability and correction

The detector performance would change mainly due to the deterioration of the chamber gas, so the detector performance were monitored and corrected as much as possible. This is new study for this work since a typical data taking period without gas change is longer than previous runs.

5.2.1 Drift velocity transition

The drift velocity was monitored during the dark matter measurement by the way described in Section 4.4.1 and its time-dependence function was determined. Figure 5.1 shows the measured drift velocity for Run14-1, Run17-1 $\sim$ Run18-2. We fitted the measured results with linear lines.
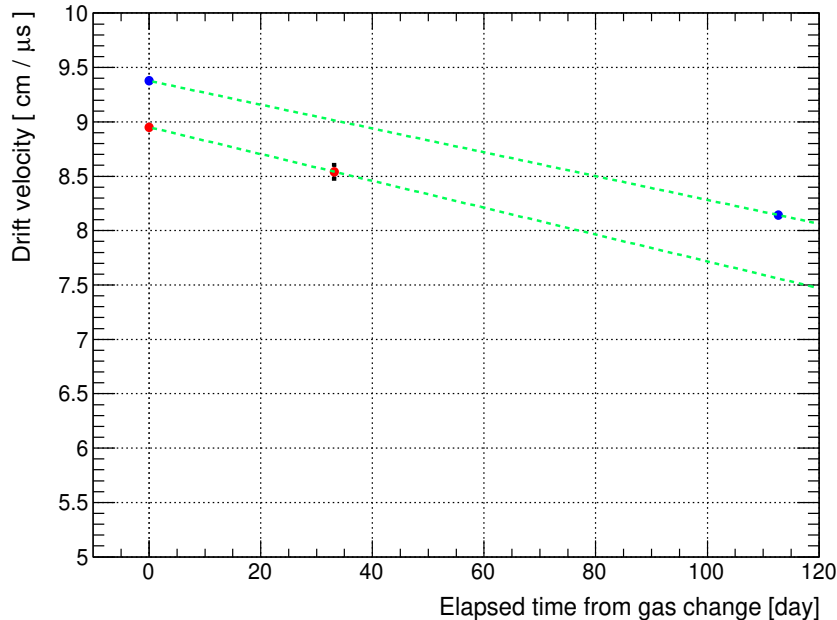
Figure 5.1: Time transition of the drift velocity. Blue and red points is the drift velocity of Run14-1 and Run17-1 $\sim$ run18-2, respectively.

A average value of rate of decrease in the drift velocity for these runs was set as typical ones. The function representing drift velocity $V_d(t)$ as a function of the elapsed day since the gas change t is shown as Equation (5.1)

$$V_d(t) = V_{di} - b_{V_d} \times t, \tag{5.1}$$

where $V_{di} = 9.5$ cm/μs is the initial drift velocity and $b_{V_d} = -0.012$ cm/μs/day is the change of drift velocity per day. Drift velocity calculated by Equation (5.1) is mainly used to convert the time duration into the z range of the tracks in the following analysis.

5.2.2 Gas gain transition

The gas gain was monitored by the energy spectrum of α particles due to the radon progeny. The gas gain is calculated by the measured charge spectrum corresponding to the peak around 6 MeV as described in Section 4.4.2. The charge spectrums, which are measured after about 1 day (red histogram) and 80 days (blue histogram) elapsed from the gas change respectively, are shown in Figure 5.2. As described from section 4.4.2, the gas gains are know from the position of the peaks. The peak position of blue histogram is seen at a position about 25% lower than that of red histogram, which mean a 25% gain decrease is seen in about 80 days. The transition of the monitored gas gain is shown in Figure 5.3. The measured results were fitted with linear lines. The parameters representing the gas gain as a function of the elapsed day since the gas change are shown in Table 5.2. The corrected gas gain was used for the conversion of the measured charge to the energy before any cuts applied so that the event selections should be applied to a corrected energy. Figure 5.4 show the energy peak after the gain correction and it is seen that the gas gain is well-corrected within systematic errors.
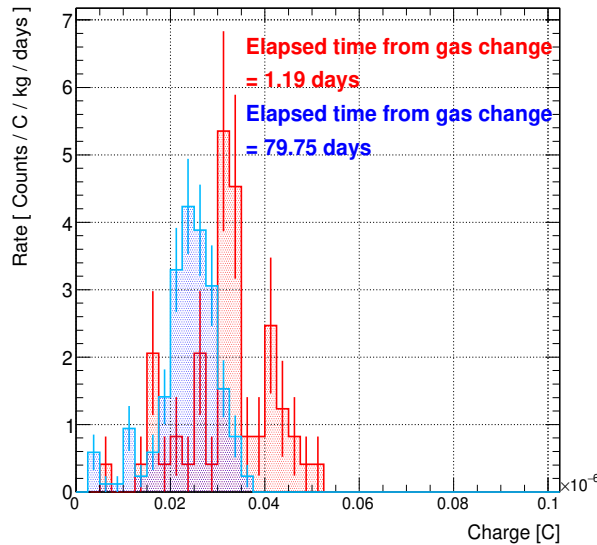
Figure 5.2: The measured charge spectrum corresponds to around 6 MeV peak. Blue and red histograms are the initial part and final part, respectively.
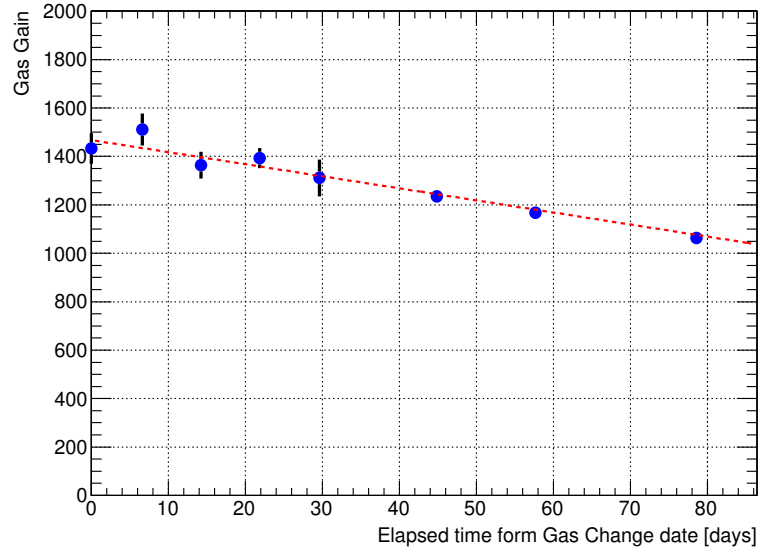
Figure 5.3: Time transition of the gas gain.

Table 5.2: Parameters of gain correction function

Run number	initial gas gain	rate of decrease [1/day]
Run14-1	1501	22.54
Run14-2	1417	10.07
Run14-3	1383	9.03
Run16-1	1569	-1.91
Run16-2	1581	-2.95
Run17-1	1524	-5.51
Run18-2	1524	-5.54
Run18-3	1507	-2.92
Run18-4	1450	-2.51
Run18-5	1494	-5.31
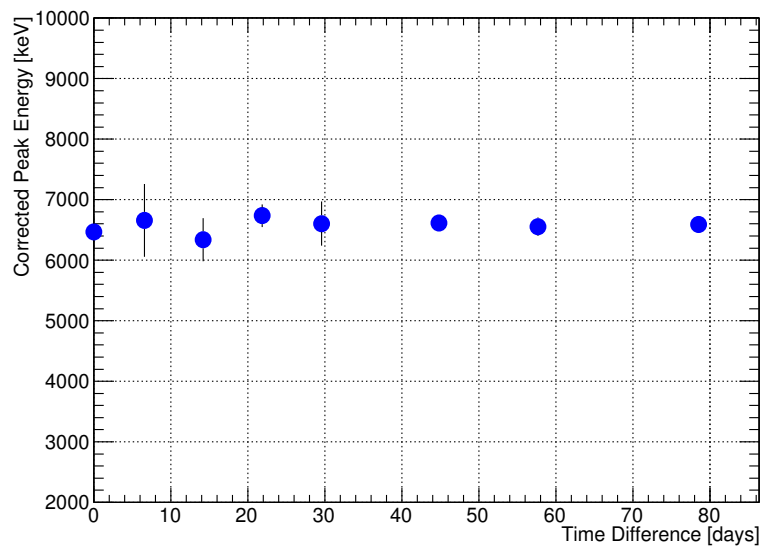
Figure 5.4: Time transition of the corrected peak energy.

5.2.3 TOT-sum transition

TOT-sum is the sum of the TOTs of all strips. The TOT of a strip is the time duration between the blue (rise time) and black (fall time) points along the strip in Figure 5.5. The TOT-sum of a single event is the total number of blue, red, and black points, where the red points lie between the start and end points of the event. As described in Section 4.4.4, TOT-sum is used as one of the important cut parameters. Since the TOT of each strip is expected to decrease as the gas gain decreases, TOT-sum is also expected to show an decrease. In o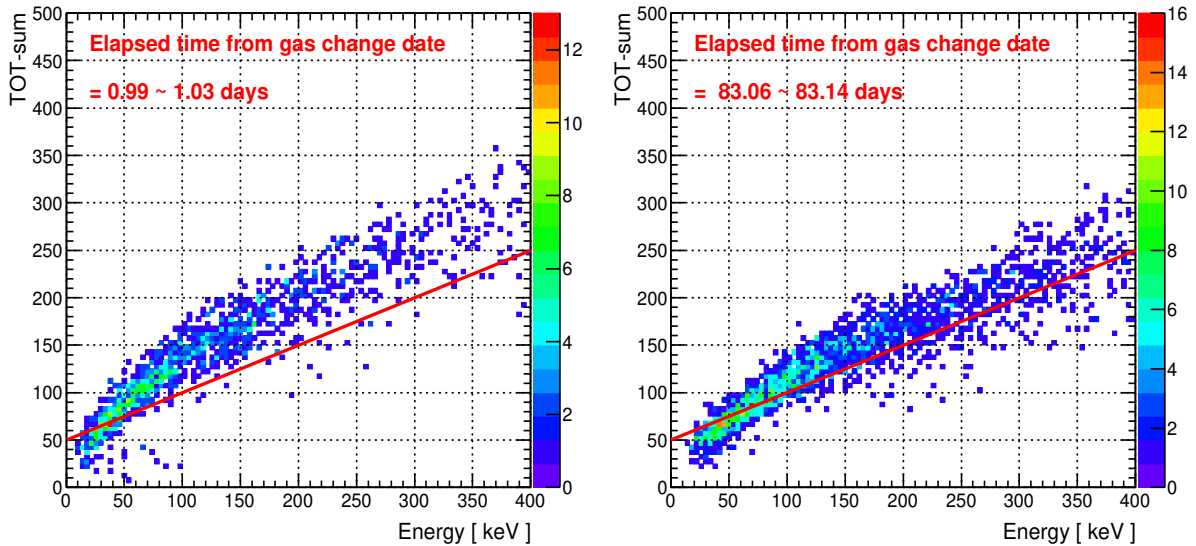rder to recover the inefficiency due to the decrease of the TOT-sum, the time dependence of the TOT-sum was studied and used for the correction.
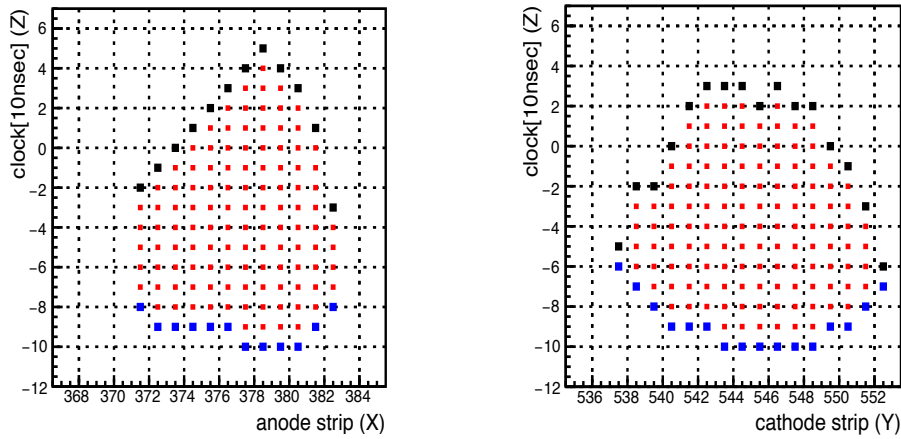
**Figure 5.5:** Track sample measured with a ^{252}Cf run. Left and right panel show the x-z and y-z plane of the track, respectively. Blue and black points show the rise time points and fall time points, respectively.

Figure 5.6: TOT-sum as function of energy. Elapsed time from gas change is $0.99 \sim 1.03$ days (Left) and $83.06 \sim 83.14$ days (Right), respectively. The red line is criteria of the TOT-sum cut.

Figure 5.6 shows TOT-sum as a function of energy. The elapsed time from gas change is 0.99 ∼ 1.03 days for left histogram and 83.06 ∼ 83.14 days for right histogram, respectively. It should be noted that the correction of gas gain described in 5.2.2 is already applied for the energy scale. The red line is criteria of the TOT-sum cut. The TOT-sum distribution becomes smaller and almost half of the distribution falls bellow the line at 50 keV after 80 days from gas change. This means the decrease of the efficiency and the TOT-sum was corrected so that the signal efficiency would be maintained. Figure 5.7 shows time transition of the TOT-sum as an example. The function obtained by fitting this graph is used as TOT-sum correction function. The parameters of TOT-sum correction function for anode at $100 - 110$ keV bin was used to determine correction factor are shown in Table A.10. Other parameters are shown in Appendix. The nuclear efficiency and gamma rejection power after these correction applied are evaluated in section 5.3.
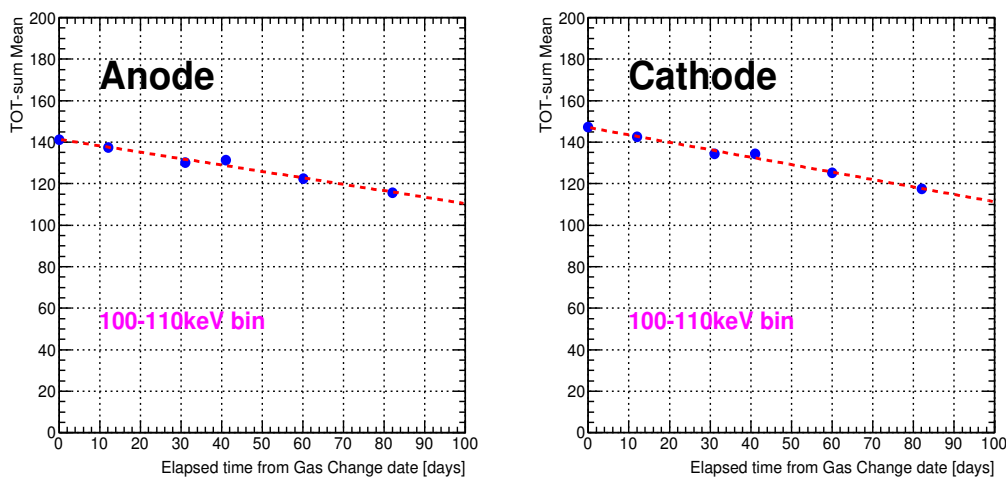
Figure 5.7: The time transition of the TOT-sum at $100 - 110$ keV bin.

Table 5.3: Parameters of TOT-sum correction function for anode at $100 - 110$ keV bin

Run number	initial TOT-sum	rate of decrease [1/day]
Run14-1	144	-0.08
Run14-2	142	0
Run14-3	148	0
Run16-1	145	-0.33
Run16-2	143	-0.17
Run17-1	135	-0.23
Run18-2	116	-0.44
Run18-3	138	-0.15
Run18-4	137	-0.10
Run18-5	141	-0.31

5.3 Event selection and results

The data went through the fiducial-cut first, then three cuts defined in Section 4.4.4 were applied. Figure 5.8-5.11 show the energy dependence of the length, the TOT-sum and the roundness of the event after each cut. Figure 5.11 shows the final sample for the dark matter analysis and its spectrum is shown in Figure 5.13 by the red histogram. Energy spectra at each cut step are also shown in Figure 5.12 and is used for analysis of dark matter limit. The effect of the length-cut and the TOT-sum-cut is remarkable for low energy region, where gamma-rays are mainly rejected. The roundness-cut affects the whole energy range, particularly in $100 - 400$ keV range. It suggests the existence of background from $-z$ (μ-PIC or GEM) and roundness-cut is effective to cut such events.
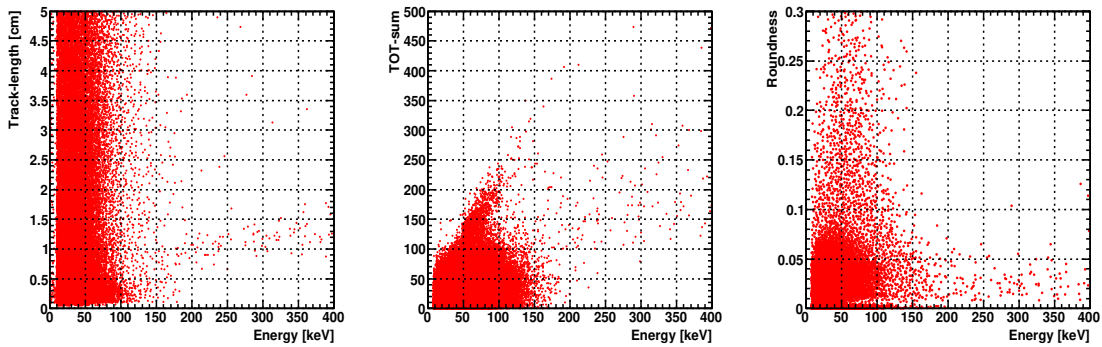
Figure 5.8: Energy dependence of the length (left), the TOT-sum (center), and the roundness (right). The events are cut by only fiducial-cut.
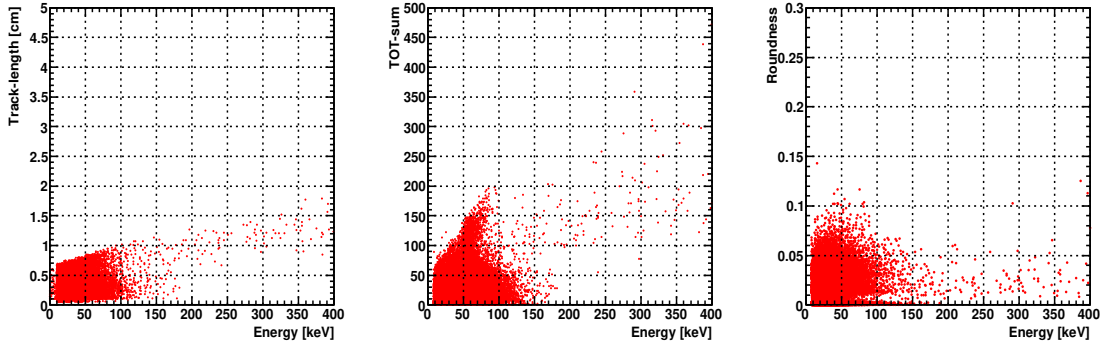
Figure 5.9: Energy dependence of the length (left), the TOT-sum (center), and the roundness (right). The events are cut by fiducial-cut and length-cut.
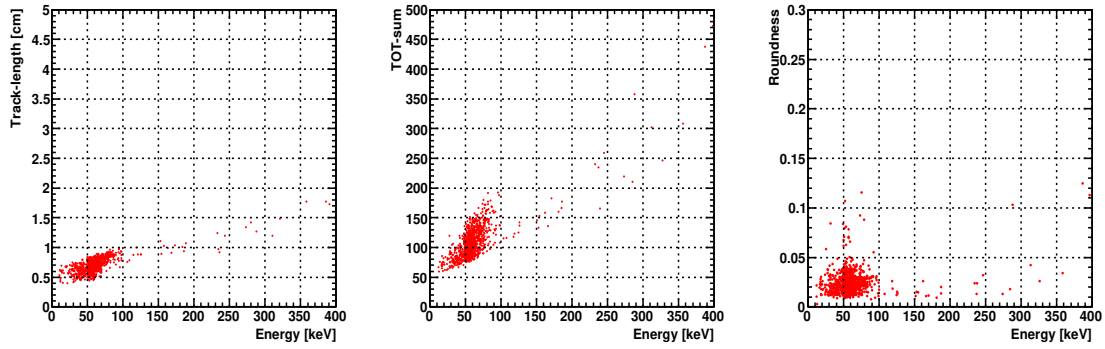
Figure 5.10: Energy dependence of the length (left), the TOT-sum (center), and the round-
ness (right). The events are cut by fiducial-cut, length-cut and TOT-sum-cut.
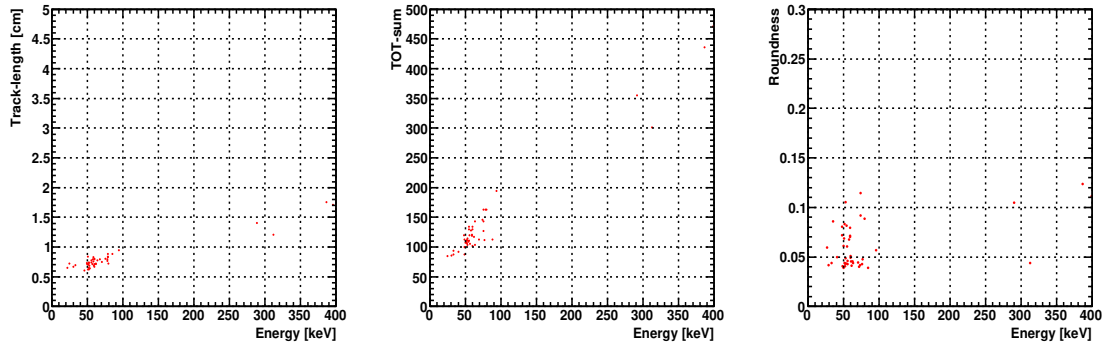
Figure 5.11: Energy dependence of the length (left), the TOT-sum (center), and the round-
ness (right). The events are final sample with the fiducial-cut, length-cut, TOT-
sum-cut and roundness-cut.
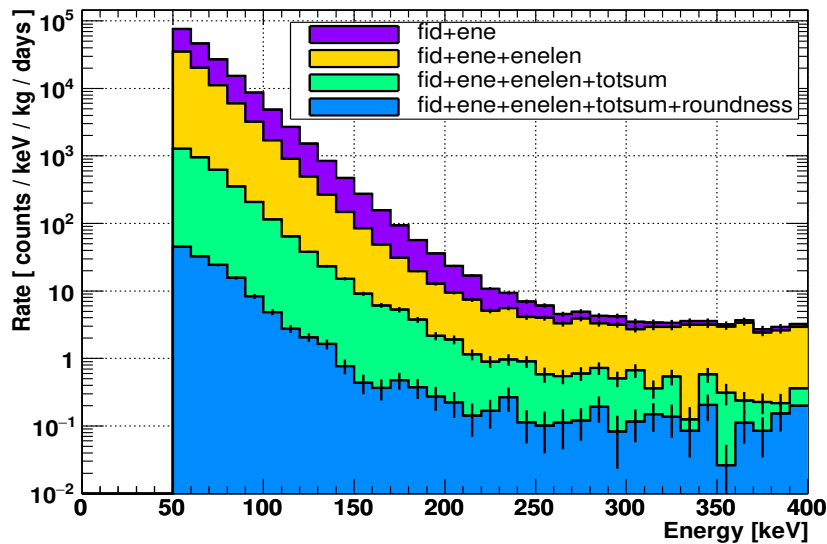
Figure 5.12: Obtained energy spectra in Kamioka Run. As show in the legend, magenta, yel-
low, green and blue histograms are the energy spectra at each cut-step described
in Section 4.4.4, and correspond to the events shown in Figure 5.8-5.11

77

Figure 5.13 shows the measured energy spectrum after all but ϕ cuts applied obtained in this measurement. The blue and red histograms correspond to NEWAGE2015 and this work respectively. Figure 5.14 and 5.16 shows skymap and $\cos\theta_{cyg}$ spectrum after all cuts including ϕ cut applied obtained in this measurement, respectively.
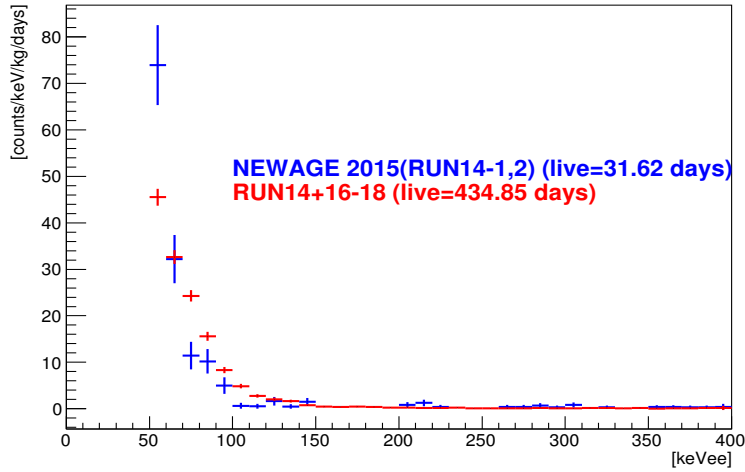
Figure 5.13: Measured energy spectrum. the red histogram is Run14 - Run18. the blue one is the previous work (NEWAGE2015, Run14-1 and Run14-2 only)
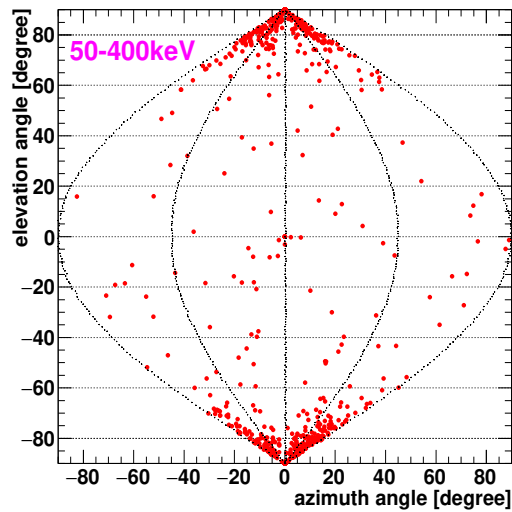
Figure 5.14: Measured direction of the nuclear tracks of Run14 - Run18 in the energy range of $50 - 400$ keV.
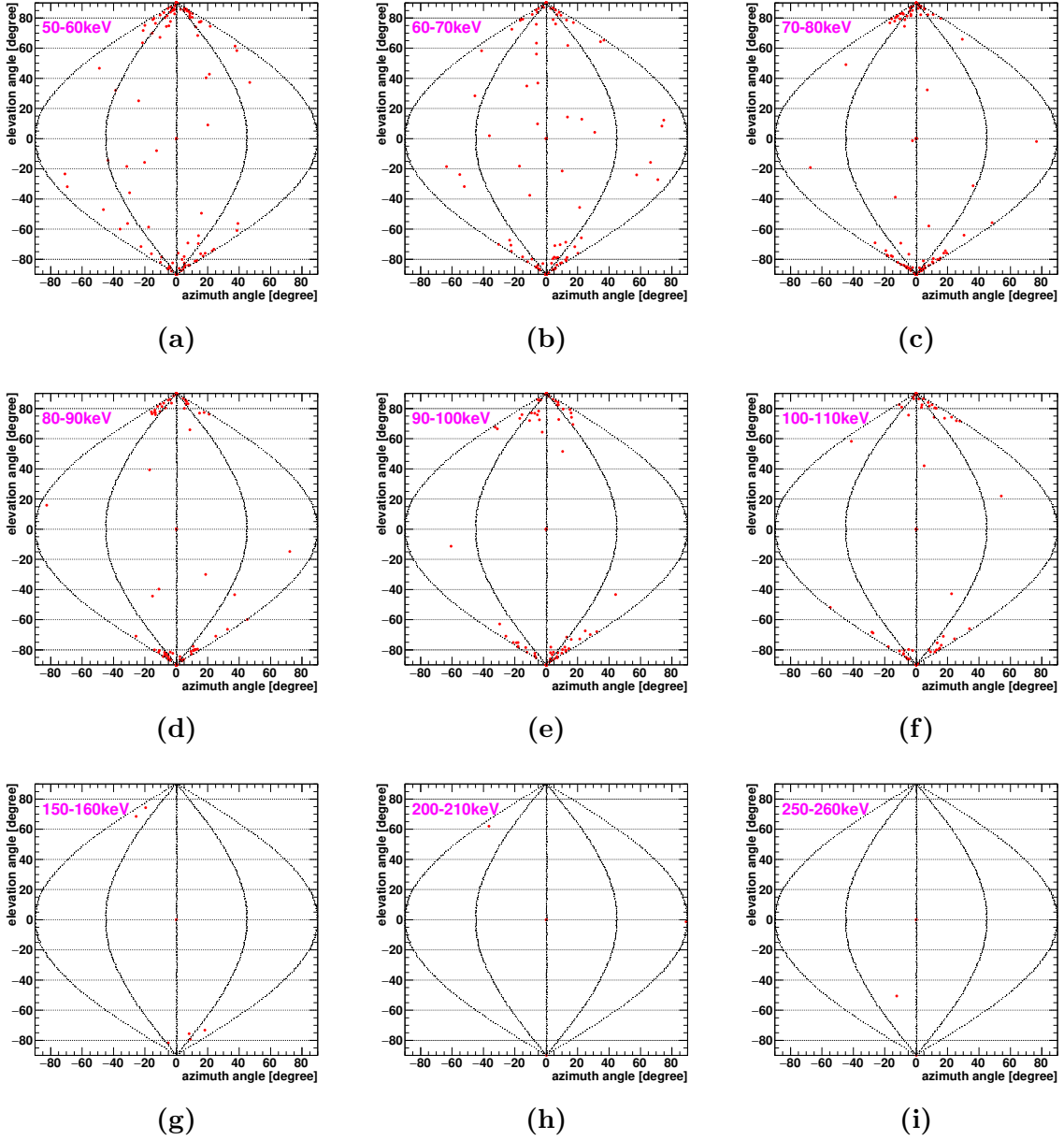
Figure 5.15: Measured $\cos\theta_{cyg}$ spectrum in the energy range of (a) $50 - 60$ keV, (b) 60-70 keV, (c) 70-80 keV, (d) 80-90 keV, (d) 90-100 keV, (e) 100-110 keV, (f) 150-160 keV, (g) 200-210 keV and (i) 250-260 keV, respectively

Obtained nuclear direction plots and corresponding $\cos\theta_{\mathrm{cygnus}}$ distribution for the $50 - 400$ keV energy range are shown in Figure 5.16. The angle θ_{cyg} is the angle between the WIMP-wind direction and the measured direction of a recoil nucleus. If we are observing the dark matter, the strong signal from the Cygnus direction around $\cos\theta_{\mathrm{cyg}} \sim 1$ is expected.
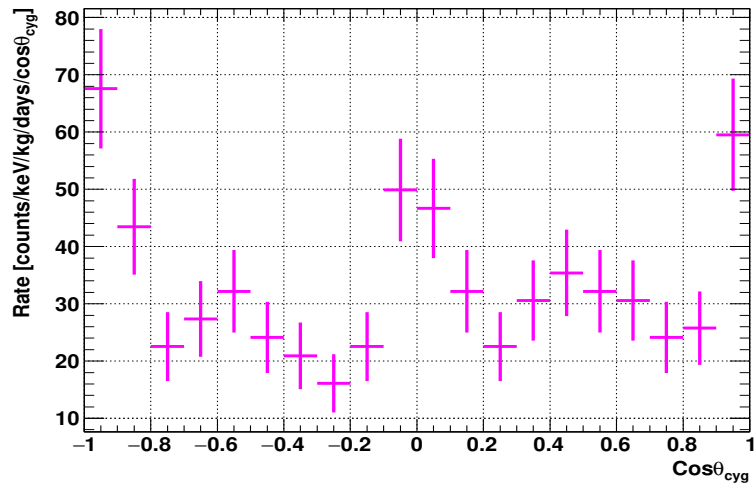
Figure 5.16: Measured $\cos\theta_{cyg}$ spectrum. the magenta histogram is Run14 - Run18 in the energy range of $50 - 400$ keV

5.4 Dark matter limits

We derived the limits of the SD cross-section $\sigma_{\chi-p}^{SD}$ by a direction-sensitive method by comparing the measured $\cos\theta_{cyg}$ distribution with a calculated one. In the calculation, we used the astrophysical parameters, nuclear parameters, and detector responses listed in Table 5.4. The calculation includes nuclear quenching factor shown in Figure 3.8 and detector responses: energy resolution, angular resolution and direction-dependent efficiency described in Section 4.4. Because of the small statistics, measured and calculated $\cos\theta_{cyg}$ shown in Figure 5.17(Left) distributions were rebined into 4-bin as shown in Figure 5.17(Right). We obtained the direction-sensitive exclusion limits by the following procedure.

(1) STEP 1

Prepare the measured $\cos\theta_{cyg}^{mes}$ distributions of the energy bin of interest (bin width is 10 keV, at least one event in the bin).

(2) STEP 2

Renormalize the measured $\cos\theta_{cyg}^{mes}$ distribution. The unit changes from [counts/keV/kg/days] to [count] by using the live time,energy bin width, fiducial mass, and the detection efficiency.

(3) STEP 3

Calculate the expected $\cos\theta_{cyg}^{sim}$ distribution by WIMPs by taking the subset of calculated angle-energy distribution (Figure 2.14). Here, the WIMP mass is assumed and the quenching factor, the energy resolution and the astrophysical and nuclear parameters listed in Table 5.4 are taken account of. Head-tail power is considered and the events are flipped with a determined probability. Then the distribution is smeared with the angular resolution of 40 ° and direction-dependent efficiency by Monte Carlo method assuming random ϕ_{cyg}^{sim}, the azimuth angle when the cygnus direction is a zenith direction.

(4) STEP 4

Renormalize the expected $\cos\theta_{cyg}^{sim}$ distribution. The unit changes from [counts/keV/kg/days] to [count] by using the live time and the fiducial mass.

(5) STEP 5

Compare the measured and expected $\cos\theta_{cyg}^{mes,sim}$ distribution by scanning the cross section $\sigma_{\chi-p}^{SD}$. To evaluate the value with the Poisson error, we used count-base distribution obtained in STEP 2 and STEP 4. If the minimum χ^2/d.o.f. is larger than χ^2/d.o.f. of 90%C.L. exclusion level (i.e. 2.7 for d.o.f. = 1), the cross-section is taken as a direction-sensitive dark matter limit. If the minimum χ^2/d.o.f. is less than χ^2/d.o.f. of 90%C.L. exclusion level, we evaluated the 90%C.L. upper limit by increasing the cross-section when the χ^2 value becomes more than χ^2/d.o.f. of 90%C.L. exclusion level.

(6) STEP 6

Repeat STEP 3-5 by changing WIMP mass.

(7) STEP 7

Repeat STEP 1-6 by changing the energy bin, and take the minimum cross-sections for each WIMP mass.

Figure 5.17 show the example of measured and calculated $\cos\theta_\text{cyg}$ distributions, again normalized into [counts/keV/kg/days/$\cos\theta_\text{cyg}$] unit. The right figure is the case of low of statistics, thus the upper limit of cross section was evaluated by increasing the cross section when the χ^2/d.o.f. value becomes more than that of 90%C.L. exclusion level(green line, the blue is best-fit).

Table 5.4: Astrophysical parameters, nuclear parameters, and detector responses

WIMP velocity distribution	Maxwellian
Maxwellian velocity dispersion	$v_0 = 220$ km/sec
Escape velocity	$v_{esc} = 650$ km/sec
Local halo density	$\rho_\text{DM} = 0.3$ GeV/c^2/cm^3
Spin factor of 19F	$\lambda^2 J(J+1) = 0.647$
Energy resolution at 50 keV	7 keV
Angular resolution at $50 - 100$ keV	40°
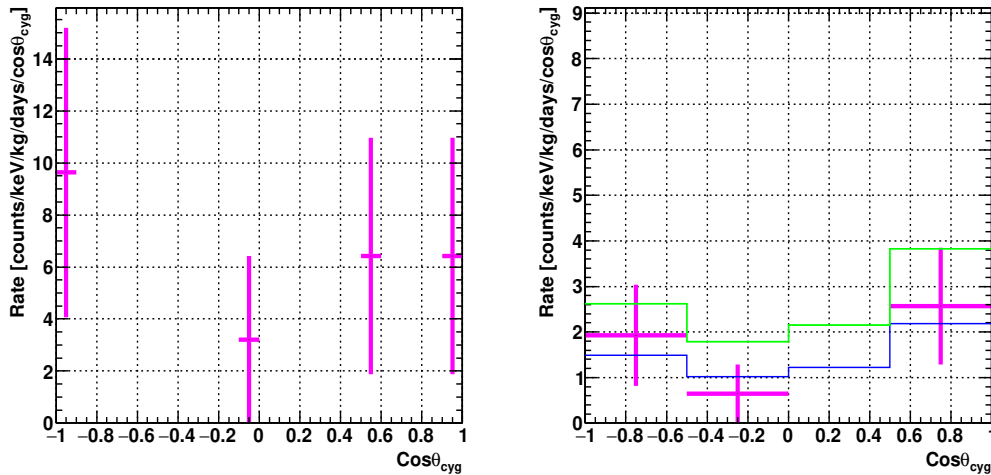
Figure 5.17: Measured $\cos\theta_\text{cyg}$ spectrum in the energy range of $100 - 110$ keV(Left). Rebined measured (magenta) and calculated (green:90%C.L. exclusion level, blue:best-fit) $\cos\theta_\text{cyg}$ distribution.

Figure 5.18 shows the limits of SD cross section as a function of mass of WIMP mass. The regions above the curves are excluded. Red thick solid line is the result with the

new (three-dimensional tracks with head-tail recognition ($E_{th} = 100$ keV)) and red thin line is the result with three-dimensional tracking without head-tail recognition ($E_{th} = 50$ keV) method in this work, respectively.
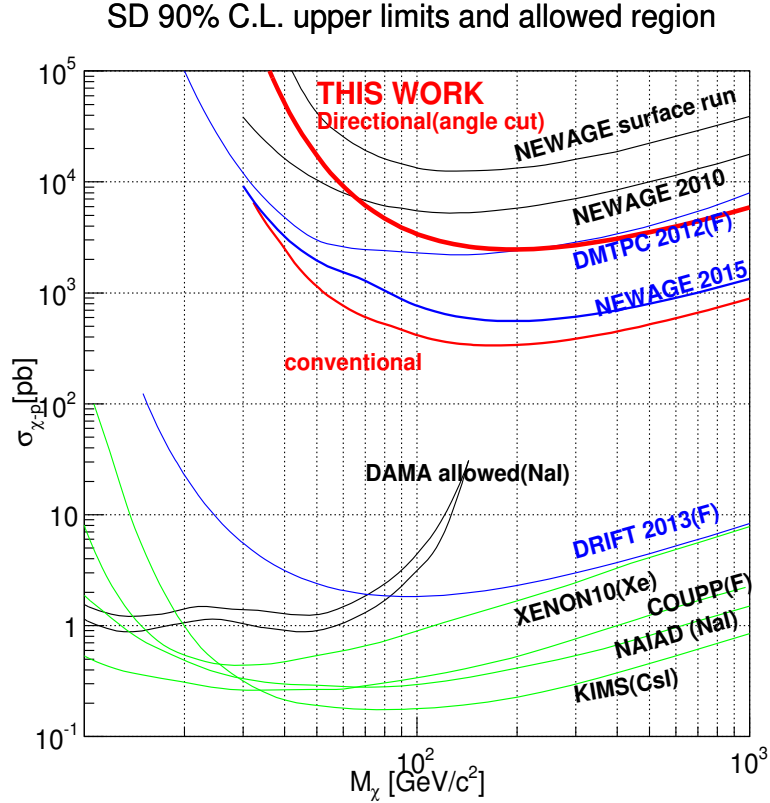
Figure 5.18: Limits of SD cross section as a function of mass of WIMP mass. Red thick solid line is the result with the new (three-dimensional tracks with head-tail recognition ($E_{th} = 100$ keV)) and red thin line is the result with three-dimensional tracking without head-tail recognition ($E_{th} = 50$ keV) method in this work, respectively. Black thin lines labeled "NEWAGE surface run", "NEWAGE 2010 (RUN5)" are previous results measured at surface and Kamioka, respectively. Blue thin line labeled "NEWAGE2015"(Run14-1, Run14-2) previous results measured at Kamioka. Allowed region (DAMA) and upper limits of other experiments are shown for comparison. Green lines are limits set by liquid or solid detectors, blue lines are the limits set by gas detectors with conventional analysis.

Chapter 6

Discussion

This work has demonstrated the dark matter search with a three-dimensional tracking detector with head-tail recognition (3D-vector detector) for the fist time. In this chapter, one of the possibilities of using these "ideal" detector to investigate the nature of the dark matter and the background discussion and a future prospects will be discussed.

6.1   Head-tail discrimination and related physics cases

Although a first experimental search was demonstrated with a 3D-vector methods, the limits are worse than the limits with 3D-axial methods. The main reason is that the head-tail analysis was only possible with tracks more than 100 keV. The head-tail parameter used in this thesis is a very primitive one and a more sophisticated method should make the energy threshold lower. Some of the possibilities for the improvements are discussed below. In this study we adopted "skewness" for the head-tail recognition parameter. Skewness is a very simple parameter and this parameterization can be improved. only X and Y TOT distributions were used in this study but Z parameter as FADC waveform are available. The Z parameter can be analyzed with X and Y parameter and one head-tail parameter out of these parameters can be obtained. One redundant parameter is obtained the track direction and head-tail are obtained from the measured data and this redundancy can be used to increase the head-tail recognition power. With these improvements, the energy threshold for the head-tail recognition would be close to the directional threshold and the limits with 3D tracks+head-tail would be close to the one with 3D tracks results.

An "ideal" 3D-vector detector is expected to provide us with a clear discovery signal of the dark matter and it is even more useful after the discovery in the view point of particle physics and astrophysics. As one of the possibilities of the physics cases, a study on the halo-model discrimination is discussed here [72]. The "standard" halo model we usually consider for the dark matter search experiments, discussed in Section 2.1 for instance, assume a Maxwell-Boltzmann velocity distribution with isotropic directions. Although this is a very natural assumption, these are some numerical simulations suggesting that the dark matter directions might not be isotropic [73, 74, 75, 76, 77, 78]. Figure 6.1 illustrates experimental expectations with these anisotropic halo model. Here an anisotropy parameter r is introduced, where r = 0 is the standard halo model and r = 1 is the fully anisotropic , or co-rotating halo model. The numerical simulation indicates

$r \sim 0.25$. The $E_r - \cos\theta$ distributions with a large statistics for various r values are shown in figures. Here E_r is the recoil energy and θ is the recoil angle with respect to the Cygnus direction. The target nucleus is fluorine and an dark matter mass of 3 times of the target nucleus is assumed. The forward-scattering distribution is expected as a broad peak around $\cos\theta = 1$ with a standard halo model (r=0), and this is the primarily signal for directional dark matter searches. The peak position shifts to smaller $\cos\theta$ with an increase of anisotropy and this change of the distribution would be the key to study the halo model. Experimental data with small statistics are compared with these template distributions as demonstrated in Figure 6.2 and halo models can be tested statistically. One of the results is shown in Figure 6.3. This is the χ^2 values between the normalized template (10^8 events) and pseudo-experimental (10^4 events) events. The pseudo experiments assumes r = 0.3 and the χ^2 values are plotted as a function of the r value assumed for the template. The case with the χ^2 above the dashed-red lines are rejected at a confidence level of 90 %. This case ($r = 0.3$ as an input) indicates that the completely isotropic case $r = 0$ can be excluded at the 90% CL with $O(10^4)$ events. The E_r-$\cos\theta$ distributions is thus such a powerful plot and a large detector which supplies these plots would be a "standard" dark matter study tool in the near future.
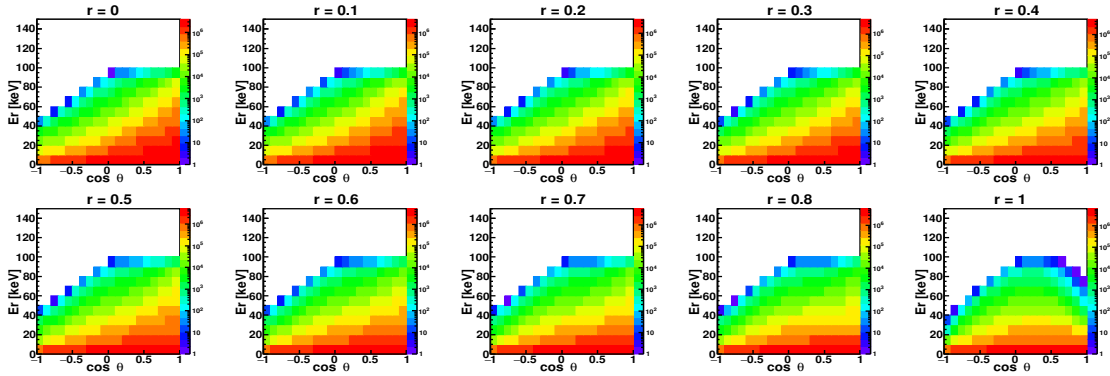
Figure 6.1: E_r-$\cos\theta$ distribution. The target nucleus is F and a dark matter mass of $3 \times$ target nucleus is assumed.
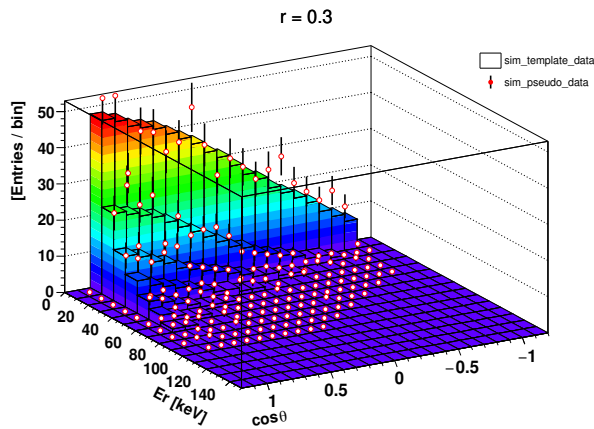
Figure 6.2: Red point is pseudo-experiment data. histogram is template data.
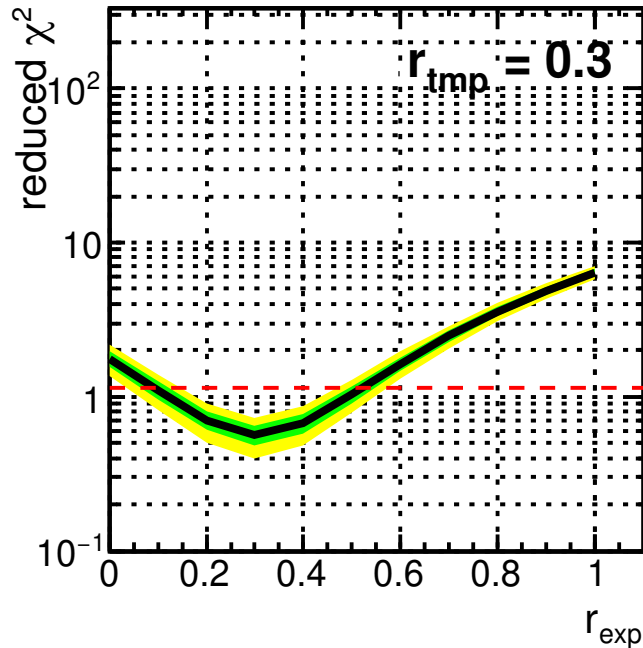
Figure 6.3: Reduced χ^2 as a function of r_{exp}

6.2 Background and future prospects

The limits with 3D-axial method were slightly improved by an improvement of the event selection and statistical increase. The detector components were kept unchanged since the last measurement (RUN14) and essentially the same discussion holds for the background sources [61]. Radioactive contaminations within the detector components are well-known background sources in rare event measurements. The radioactive contaminations emit $\gamma-$rays, $\beta-$rays and $\alpha-$rays. In our case, $\gamma-$rays and $\beta-$rays were rejected with a rejection power of $\sim 10^{-5}$, but $\alpha-$rays cannot be discriminated from nuclear recoils.

Preceding study revealed that the background sources in the energy range relevant to the dark matter search was μ-PIC. C' in Figure 6.4 illustrate the dominant background. The insulator in the μ-PIC was found to contain 0.4×10^{-6}g/g of ^{238}U and 1.8×10^{-6}g/g of ^{232}Th [79, 80]. While this work focused on the long-term data taking and new analytical approach for the head-tail recognition, two works for the background reduction are on-going. First is a direct approach to reduce the α-ray' emission from the μ-PIC by reducing the amount of ^{238}U and ^{232}Th contamination in the μ-PIC. A "cleaner" μ-PIC, or a low-α μ-PIC, with more than two orders of magnitude less contamination of ^{238}U and ^{232}Th was developed [79]. It's performance was tested and the low-α μ-PIC was installed to the NEWAGE-0.3b' detector replacing the standard μ-PIC used for this work in November 2018. The data taking has been started and a result will come very soon. Second is a approach to make the measurement of absolute Z positions of the tracks with so-called minority carriers. In a self-triggering TPCs like NEWAGE in self trigger mode, absolute Z positions of the tracks are not known. A new technique makes the absolute-Z measurement possible was invented in 2015by the DRIFT group [81]. This technique makes use of the difference of the drift velocities of more than one species of negative-charged ions. These minority carriers make it possible to distinguish the tracks

from the μ-PIC plane as well as the drift plane which is potential background source. Intensive studies are being performed to implement this negative-ion TPC technology to the NEWAGE detector with an goal of background reduction of two orders of magnitude [82].

After these improvements were completed, it is expected that the γ-ray background and ambient neutron background will become serious background sources. Improvements on the γ-ray rejection and installation of a neutron shieldings would help to go below these backgrounds. Then the sensitivity will reach the DAMA region and the investigation in the DAMA region will be performed.
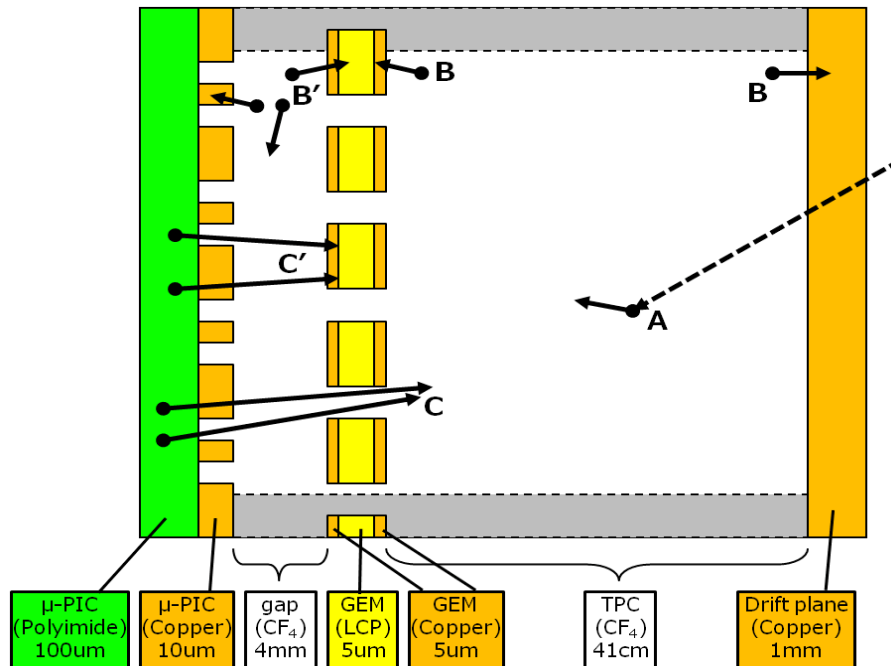
Figure 6.4: Candidates of low-energy background events (50-400 keV)[64].

Chapter 7

Conclusion

A direction-sensitive dark matter search with the NEWAGE-0.3b' three-dimensional gaseous tracking detector was performed from Jul. 17, 2013 to Aug. 8, 2017. The total live time obtained by this measurement is 434.85 days corresponding to an exposure of 4.505 kg·days, which is about 14 times larger than that of the previous work (NEWAGE2015). In this analysis, two new analysis methods were introduced to the NEWAGE analysis. First is the detector performance correction for a long term measurement. Second is the head-tail recognition of the nuclear tracks. Although the head-tail recognition power is limited, this method upgraded the NEWAGE-0.3b' detector from a "3D-axial" detector to a "3D-vector" detector. With this newly upgraded a 3D-vector detector, a first dark matter search was performed. The first experimental dark matter limits with a 3D-vector detector were set. The 90% spin-dependent WIMP-nucleon cross section limit of 2465 pb for 200 GeV/c^2 WIMP was obtained. The limit with 3D-axial method was also improved to 417 pb for 200 GeV/c^2 WIMPs.

Acknowledgment

Bibliography

[1] K. G. Begeman, A. H. Broeils, and R. H. Sanders MNRAS (1991) 523.

[2] M. Loewenstein and R. F. Mushotzky, Astrophys. J. (1996) 83.

[3] D. Clowe. et al. Astrophys. J. (2006) L109.

[4] R. A. Knop et al. Astrophys. J. 598 (2003) 102.

[5] Planck Collaboration XIII, 2016, A&A 594, A11

[6] D. J. Eisenstein et al. Astrophys. J. 633 (2005) 560.

[7] D. Kirkman et al. Astrophys. J. Suppl. Ser. 149 (2003) 1.

[8] G. Jungman et al. Phys. Rep. 267 (1996) 195.

[9] G. Servant et al. New J. Phys. 4 (2002) 99.

[10] N. Arkani-Hamed et al. J. High Energy Phys. 07 (2002) 034.

[11] R. D. Peccei and Helen R. Quinn et al. Phys. Rev. Lett. 38 (1977) 1440.

[12] L. D. Luffy and K. Bibber et al. New Journal of Physics 11 (2009) 105008.

[13] P. Sikivie et al. Phys. Rev. Lett. 51 (1983) 1415.

[14] C. Patrignani et al. (Particle Data Group), Chin. Phys. C, 40, 100001 (2016).

[15] A. Boyarsk et al. Ann. Rev. Nuc. Part. Sci. 59 (2009) 191.

[16] G. M. Fuller et al. Phys. Rev. D 68 (2003) 103002.

[17] R. Adhikari et al. JCAP 01 (2017) 025

[18] Matthias Danninger 2017 J. Phys.: Conf. Ser. 888 012039

[19] E. Aprile et al. PRL 119, 181301 (2017)

[20] Xiangyi Cui et al. PRL 119, 181302 (2017)

[21] C. Amole et al. PRL 118, 251301 (2017)

[22] Hardy M. Hodges Phys. Rev. D 47 (1993) 456.

[23] Kalliopi Petraki, Raymond R. Volkas Int. J. Mod. Phys. A 28 (2013) 1330028.

[24] John Ellis, V. E. Mayes and D. V. Nanopoulos Phys. Rev. D 74 (2006) 115003.

[25] J. D. Lewin and P. F. Smith Astropart. Phys. 6 (1996) 87.

[26] J. Ellis et al. Phys. Lett. B 481 (2000) 304.

[27] A. Ferstl and K. A. Olive Phys. Rev. D 59 (1999) 055009.

[28] D. Spergel Phys. Rev. D 37 (1988) 1353.

[29] R. Bernabei et al. Phys. Lett. B 480 (2000) 23.

[30] K. Fushimi et al. J. Phys. Conf. Ser. 469 (2013) 012011.

[31] J. Cherwinka et al. Astropart. Phys. 35 (2012) 749.

[32] G. J. Alner et al. Phys. Lett. B 616 (2005) 17.

[33] Y. Shimizu et al. Phys. Lett. B 633 (2006) 195.

[34] H. S. Lee, et al. (KIMS Collaboration) Phys. Rev. Lett. 99 (2007) 091301.

[35] R. B. et al. New J. Phys. 2 (2000) 15.1.

[36] XMASS Collaboration, Physics Letters B 759 (2016) 272-276

[37] DEAP-3600 Collaboration, arXiv:1707.08042v2 (2017)

[38] D. S. Akerib et al. (LUX Collaboration) Phys. Rev. Lett. 118, 021303

[39] E. Aprile et al. (XENON Collaboration) Phys. Rev. Lett. 109 (2012) 181301.

[40] R. Agnese et al. (superCDMS Collaboration) arXiv:1707.01632v2

[41] C. E. Aalseth et al. Phys. Rev. D 88 (2013) 012002.

[42] L. Hehn et al. Eur. Phys. J. C (2016) 76:548

[43] G. Angloher et al. Eur. Phys. J. C (2016) 76:25

[44] J. Barreto et al. Phys. Lett. B 711 (2012) 264.

[45] E. Behnke et al. Phys. Rev. D 86 (2012) 052001.

[46] M. Felizardo et al. 1106.3014v3 (2011).

[47] S. Archambault et al. Phys. Lett. B 711 (2012) 153.

[48] D. R. Nygren J. Phys. Conf. Ser. 460 (2013) 012006.

[49] S. F. Biagi Nucl. Instr. Meth. Phys. Res. A 283 (1989) 716.

[50] G. F. Reinking et al. Journal of Applied Physics 60, 499 (1986);

[51] Archana Sharma Properties of some gas mixtures used in tracking detectors. SLAC-JOURNAL-ICFA-16-3, July 1998.

[52] J.F. Ziegler, J.P. Biersack SRIM The Stopping and Range of Ions in Matter, Code (1985).

[53] A. H. et al. Rad. Phys. and Chem. 77 (2008) 1311.

[54] J.B.R. Battat et al. Astroparticle Physics 91 (2017) 65-74

[55] S. Ahlen et al. Phys. Lett. B 695 (2011) 124.

[56] D. Santos et. al. J. Phys. Conf. Ser. 309 (2011) 012014.

[57] S. E. Vahsen EAS publication series, Proceedings of CYGNUS 2011, Third International Conference on Directional Detection of Dark Matter 53 (2012) 43.

[58] J. P. Cussonneau Nucl. Instr. and Meth. in Phys. Res. A 419 (1998) 452.

[59] F. Sauli and A. Sharma Annu. Rev. Nucl. Part. Sci 49 (1999) 341.

[60] G. Aad JINST 3 (2008) P07007.

[61] K. Nakamura et al : Prog. Theor. Exp. Phys. **14** (2015) 043F01.

[62] Tadaaki Tani, Tatsuhiro Naka , Radiation Measurements 95 (2016) 31-36

[63] K. Miuchi Oral presentation at CYGNUS2011, 7-10 June 2011, AUSSOIS (France) (2011).

[64] K. Nakamura Doctor Thesis Kyoto University (January 2014).

[65] A. Takada et. al. Nucl. Instrm. Methods Phys. Res. Sect. A 573 (2007) 195.

[66] F. Sauli and A. Sharma Annu. Rev. Nucl. Part. Sci 49 (1999) 341.

[67] H. K. et al. IEEE Nucl. Sci. Symp. Conf. Rec. 1 (2005) 371.

[68] S. Agostinelli et al. Nucl. Instr. Meth. Phys. Res. A 506 (2003) 250.

[69] K. Nakamura et. al. JINST. 7 (2011) C02023.

[70] K. Miuchi et al. arXiv:1109.3099v2

[71] R. Yakabe et al. JPS Conf. Proc. 11, 040002 (2016)

[72] K. Nagao et al., Discrimination of anisotropy in dark matter velocity distribution with directional detectors, submitted for Physics of the Dark Universe, December 2017.

[73] J. I. Read, G. Lake, O. Agertz and V. P. Debattista, Mon. Not. Roy. Astron. Soc. 389, 1041 (2008)

[74] J. I. Read, L. Mayer, A. M. Brooks, F. Governato and G. Lake, Mon. Not. Roy. Astron. Soc. 397, 44 (2009)

[75] F. S. Ling, E. Nezri, E. Athanassoula and R. Teyssier, JCAP 1002, 012 (2010).

[76] M. Maciejewski, M. Vogelsberger, S. D. M. White and V. Springel, Mon. Not. Roy. Astron. Soc. 415, 2475 (2011)

[77] M. Lisanti and D. N. Spergel, Phys. Dark Univ. 1, 155 (2012)

[78] M. Kuhlen, M. Lisanti and D. N. Spergel, Phys. Rev. D 86, 063505 (2012)

[79] T. Hashimoto et al. arXiv:1707.09744v1

[80] T.Hashimoto Master Thesis Kobe University (February 2016)

[81] J.B.R. Battat et al. / Physics of the Dark Universe 9-10 (2015) 1-7

[82] T.Ikeda et al. arXiv:1709.06219v1

[83] Final model independent result of DAMA/LIBRA - phase1 : Eur.Phys.J.C. **73** (2013) 2648.

[84] Toru Tanimori, Kentaro Miuchi et al : Phys. Rev. B **578** (2004), 241

Appendix A

Append

Table A.1: Parameters of TOT-sum correction function for run14-1

Energy min [keV]	Energy max [keV]	initial TOT-sum (anode)	rate of decrease [1/day](anode)	initial TOT-sum (cathode)	rate of decrease [1/day](cathode)
50	60	104	0	94	0
60	70	115	0	107	0
70	80	126	-0.02	118	-0.02
80	90	134	0	127	0
90	100	144	-0.08	137	-0.05
100	110	151	-0.01	145	0
110	120	159	-0.01	153	0
120	130	166	0	162	0
130	140	174	0	170	0
140	150	182	-0.09	178	-0.02
150	160	188	0	185	0
160	170	193	0	192	0
170	180	201	-0.03	199	-0.01
180	190	204	0	202	0
190	200	215	0	213	-0
200	210	219	0	218	0

Table A.2: Parameters of TOT-sum correction function for run14-2

Energy min [keV]	Energy max [keV]	initial TOT-sum (anode)	rate of decrease [1/day](anode)	initial TOT-sum (cathode)	rate of decrease [1/day](cathode)
50	60	99	0	89	0
60	70	109	-0.01	100	-0.01
70	80	118	0	110	0
80	90	127	-0.02	120	-0
90	100	135	0	128	0
100	110	142	0	137	-0.01
110	120	150	0	145	0
120	130	157	-0.02	153	-0.04
130	140	164	0	160	0
140	150	171	-0.01	167	0
150	160	177	0	174	0
160	170	183	0	181	-0.05
170	180	190	-0.09	187	-0.05
180	190	193	0	192	0
190	200	200	-0.02	199	-0.01
200	210	204	0	204	0

Table A.3: Parameters of TOT-sum correction function for run14-3

Energy min [keV]	Energy max [keV]	initial TOT-sum (anode)	rate of decrease [1/day](anode)	initial TOT-sum (cathode)	rate of decrease [1/day](cathode)
50	60	102	0	93	0
60	70	113	0	105	0
70	80	122	0	116	0
80	90	131	0	125	0
90	100	139	0	133	0
100	110	148	0	143	0
110	120	153	0	151	0
120	130	163	0	159	0
130	140	169	0	166	0
140	150	175	0	174	0
150	160	184	0	182	0
160	170	189	0	189	0
170	180	194	0	194	0
180	190	197	0	199	0
190	200	204	0	206	0
200	210	211	0	213	0

Table A.4: Parameters of TOT-sum correction function for run16-1

Energy min [keV]	Energy max [keV]	initial TOT-sum (anode)	rate of decrease [1/day](anode)	initial TOT-sum (cathode)	rate of decrease [1/day](cathode)
50	60	98	-0.3	95	-0.07
60	70	108	-0.28	107	-0.05
70	80	119	-0.29	118	-0.06
80	90	128	-0.28	128	-0.05
90	100	138	-0.33	139	-0.08
100	110	145	-0.33	147	-0.12
110	120	154	-0.36	157	-0.12
120	130	159	-0.35	162	-0.09
130	140	167	-0.33	171	-0.08
140	150	174	-0.36	177	-0.08
150	160	184	-0.44	188	-0.17
160	170	188	-0.34	193	-0.09
170	180	195	-0.42	201	-0.17
180	190	198	-0.39	204	-0.09
190	200	207	-0.48	211	-0.15
200	210	211	-0.43	217	-0.14

Table A.5: Parameters of TOT-sum correction function for run16-2

Energy min [keV]	Energy max [keV]	initial TOT-sum (anode)	rate of decrease [1/day](anode)	initial TOT-sum (cathode)	rate of decrease [1/day](cathode)
50	60	94	-0.13	98	-0.1
60	70	105	-0.16	111	-0.14
70	80	116	-0.18	123	-0.15
80	90	126	-0.19	133	-0.16
90	100	135	-0.19	143	-0.15
100	110	143	-0.17	151	-0.13
110	120	151	-0.17	161	-0.17
120	130	157	-0.19	168	-0.17
130	140	163	-0.14	174	-0.11
140	150	173	-0.25	184	-0.22
150	160	178	-0.22	190	-0.15
160	170	183	-0.19	194	-0.14
170	180	192	-0.22	204	-0.19
180	190	197	-0.22	212	-0.23
190	200	202	-0.27	216	-0.26
200	210	211	-0.36	224	-0.32

Table A.6: Parameters of TOT-sum correction function for run17-1

Energy min [keV]	Energy max [keV]	initial TOT-sum (anode)	rate of decrease [1/day](anode)	initial TOT-sum (cathode)	rate of decrease [1/day](cathode)
50	60	89	-0.18	95	-0.38
60	70	99	-0.19	106	-0.41
70	80	109	-0.21	117	-0.41
80	90	118	-0.19	127	-0.36
90	100	128	-0.26	137	-0.44
100	110	135	-0.23	144	-0.38
110	120	142	-0.22	153	-0.42
120	130	150	-0.33	161	-0.53
130	140	155	-0.14	167	-0.38
140	150	163	-0.35	175	-0.48
150	160	169	-0.33	182	-0.49
160	170	177	-0.4	190	-0.55
170	180	181	-0.26	195	-0.46
180	190	190	-0.56	203	-0.68
190	200	193	-0.5	208	-0.67
200	210	200	-0.59	215	-0.78

Table A.7: Parameters of TOT-sum correction function for run18-2

Energy min [keV]	Energy max [keV]	initial TOT-sum (anode)	rate of decrease [1/day](anode)	initial TOT-sum (cathode)	rate of decrease [1/day](cathode)
50	60	75	-0.26	77	-0.32
60	70	83	-0.33	86	-0.35
70	80	92	-0.39	96	-0.44
80	90	100	-0.35	104	-0.41
90	100	110	-0.48	116	-0.56
100	110	116	-0.45	123	-0.51
110	120	123	-0.41	129	-0.42
120	130	129	-0.43	136	-0.46
130	140	137	-0.47	145	-0.57
140	150	144	-0.56	153	-0.64
150	160	146	-0.43	154	-0.47
160	170	153	-0.51	163	-0.6
170	180	159	-0.55	167	-0.51
180	190	163	-0.48	173	-0.56
190	200	170	-0.43	178	-0.43
200	210	167	-0.25	180	-0.45

Table A.8: Parameters of TOT-sum correction function for run18-3

Energy min [keV]	Energy max [keV]	initial TOT-sum (anode)	rate of decrease [1/day](anode)	initial TOT-sum (cathode)	rate of decrease [1/day](cathode)
50	60	91	-0.11	92	-0.13
60	70	102	-0.11	104	-0.13
70	80	113	-0.14	117	-0.17
80	90	121	-0.12	125	-0.14
90	100	130	-0.14	135	-0.18
100	110	138	-0.16	144	-0.16
110	120	148	-0.18	154	-0.2
120	130	154	-0.16	160	-0.16
130	140	161	-0.14	169	-0.17
140	150	167	-0.18	174	-0.17
150	160	174	-0.17	182	-0.17
160	170	178	-0.15	187	-0.17
170	180	188	-0.2	197	-0.22
180	190	193	-0.21	203	-0.23
190	200	194	-0.15	207	-0.23
200	210	201	-0.15	212	-0.18

Table A.9: Parameters of TOT-sum correction function for run18-4

Energy min [keV]	Energy max [keV]	initial TOT-sum (anode)	rate of decrease [1/day](anode)	initial TOT-sum (cathode)	rate of decrease [1/day](cathode)
50	60	91	-0.13	94	-0.15
60	70	102	-0.12	105	-0.13
70	80	112	-0.11	116	-0.14
80	90	122	-0.14	126	-0.16
90	100	131	-0.16	136	-0.16
100	110	137	-0.1	143	-0.12
110	120	146	-0.14	152	-0.16
120	130	154	-0.16	160	-0.18
130	140	161	-0.15	168	-0.15
140	150	167	-0.13	174	-0.14
150	160	177	-0.2	185	-0.2
160	170	180	-0.18	188	-0.19
170	180	187	-0.18	195	-0.15
180	190	194	-0.2	204	-0.19
190	200	199	-0.16	210	-0.2
200	210	201	-0.1	212	-0.13

Table A.10: Parameters of TOT-sum correction function for run18-5

Energy min [keV]	Energy max [keV]	initial TOT-sum (anode)	rate of decrease [1/day](anode)	initial TOT-sum (cathode)	rate of decrease [1/day](cathode)
50	60	94	-0.22	94	-0.25
60	70	105	-0.27	108	-0.3
70	80	116	-0.28	119	-0.33
80	90	126	-0.31	129	-0.34
90	100	133	-0.29	139	-0.35
100	110	141	-0.31	147	-0.36
110	120	150	-0.34	156	-0.38
120	130	156	-0.32	163	-0.37
130	140	163	-0.34	171	-0.38
140	150	170	-0.34	177	-0.38
150	160	176	-0.34	185	-0.4
160	170	183	-0.37	192	-0.42
170	180	187	-0.35	197	-0.41
180	190	193	-0.38	204	-0.42
190	200	199	-0.37	209	-0.43
200	210	206	-0.43	217	-0.48